CONTENTS

Janusz Gołdasz, Bogdan Sapiński
Application of CFD to Modeling of Squeeze Mode Magnetorheological Dampers 129

Artur Ganczarski, Damian Szubartowski
On the Stress Free Deformation of linear FGM interface under Constant Temperature 135

Vasyl' Shvabjuk, Georgij Sulym, Olena Mikulich
Stress State of Plates with Incisions under the Action of Oscillating Concentrated Forces 140

Zbigniew Budniak
Modelling and Numerical Analysis Of Assembly System 145

Monika Prucnal-Wiesztort
Accuracy of Positioning and Orientation of Effector of Planar Parallel Manipulator 3RRR 151

Krzysztof Kęcik
Application of Shape Memory Alloy in Harvesto-Absorber System 155

Aneta Bohojło-Wiśniewska
Numerical Modelling of Humid Air Flow around a Porous Body 161

Dominik Sawicki, Eugeniusz Zieniuk
Parametric Integral Equations Systems Method in Solving Unsteady Heat Transfer Problems for Laser Heated Materials 167

Piotr Czarnocki, Kamila Czajkowska
Delamination Resistance of Laminate Made with VBO MTM46/HTS Prepreg 173

Heorhiy Sulym, Lyubov Piskozub, Yosyf Piskozub, Yaroslav Pasternak
Antiplane Deformation of a Bimaterial Containing an Interfacial Crack with the Account of Friction.
2. Repeating and Cyclic Loading 178

Abstracts 185

ABSTRACTS

Janusz Gołdasz, Bogdan Sapiński
Application of CFD to Modeling of Squeeze Mode Magnetorheological Dampers

The so-called squeeze flow involves a magnetorheological (MR) fluid sandwiched between two planar surfaces setting up a flow channel. The height of the channel varies according to a prescribed displacement or force profile. When exposed to a magnetic field of sufficient strength MR fluids develop a yield stress. In squeeze-mode devices the yield stress varies with both the magnetic field magnitude and the channel height. In this paper an unsteady flow model of an MR fluid in squeeze mode is proposed. The model is developed in Ansys Fluent R16. The MR material flow model is based on the apparent viscosity approach. In order to investigate the material's behaviour the authors prepared a model of an idealized squeeze-mode damper in which the fluid flow is enforced by varying the height of the channel. Using mesh animation, the model plate is excited, and as the mesh moves, the fluid is squeezed out of the gap. In the simulations the model is subjected to a range of displacement inputs of frequencies from 10 to 20 Hz, and local yield stress levels up to 30 kPa. The results are presented in the form of time histories of the normal force on the squeezing plate and loops of force vs. displacement (velocity).

Artur Ganczarski, Damian Szubartowski
On the Stress Free Deformation of linear FGM interface under Constant Temperature

This paper demonstrates the stress free thermo-elastic problem of the FGM thick plate. Existence of such a purely thermal deformation is proved in two ways. First proof is based on application of the Iljushin thermo-elastic potential to displacement type sys-tem of equations. This reduces 3D problem to the plane stress state problem. Next it is shown that the unique solution fulfils conditions of simultaneous constant temperature and linear gradation of thermal expansion coefficient. Second proof is based directly on stress type system of equations which straightforwardly reduces to compatibility equations for purely thermal deformation. This occurs if only stress field is homogeneous in domain and at boundary. Finally an example of application to an engineering problem is presented.

Vasyl' Shvabjuk, Georgij Sulym, Olena Mikulich
Stress State of Plates with Incisions under the Action of Oscillating Concentrated Forces

This paper proposes the novel technique for analysis of dynamic stress state of multi-connected infinite plates under the action of oscillating forces. Calculation of dynamic stresses at the incisions of plates is held using the boundary-integral equation method and the theory of complex variable functions. The numerical implementation of the developed algorithmis based on the method of mechanical quadratures and collocation technique. The algorithm is effective in the analysis of the stress state caused by steady-state vibrations of plates.

Zbigniew Budniak
Modelling and Numerical Analysis Of Assembly System

The present articles covers a concept of the creation and testing of assembly systems with the use of modern CAD and CAE systems on the example of an assembly system designed for joining parts with circular surfaces that are fitted with positive clearance. The numerical investigations were based on the constructed spatial skeleton pattern of the system. The purpose of the simulation tests was to determine the impact of the measurement and angular inaccuracies of all the elements of the assembly system as well as the inaccuracy of the positioning of the robot's drives on the positioning accuracy of the parts joined taking into consideration the conditions of assembly in automatic assembly.

Monika Prucnal-Wiesztort
Accuracy of Positioning and Orientation of Effector of Planar Parallel Manipulator 3RRR

Parallel manipulator belongs to group of mechanisms with closed kinematic chains. This feature involves both advantages and disadvantages. The study examined the issue of accuracy of a planar system with three degrees of freedom, with revolute pairs, showing the effect of errors of the drives settings on effector positioning deviation. Enclosed is a numerical example for which analyzed the deviation in motion manipulator when going through the singular configuration. Based on the analysis was determined the area around the singular positions for which to obtain the orientation of the assumed accuracy is impossible.

Krzysztof Kęcik
Application of Shape Memory Alloy in Harvesto-Absorber System

This paper presents a conception of the harvester-absorber system consisting of two parts. The first is the pendulum attached to the main system (oscillator), which is suspended on the linear damper and the nonlinear spring made of shape memory alloy. The spring is modelled as a polynomial function based on Landau–Ginzburg theory of phase transitions (similar as ferroelectric and ferromagnets). The obtained results show, that SMA element can increase harvesting energy level, while the absorber effect can be impaired (but not loss). Additionally, introducing SMA element causes changes in dynamics, introduces a new unstable solutions and bifurcations. The analysis was done by classical integration and continuation solution methods.

Aneta Bohojło-Wiśniewska
Numerical Modelling of Humid Air Flow around a Porous Body

This paper presents an example of humid air flow around a single head of Chinese cabbage under conditions of complex heat transfer. This kind of numerical simulation allows us to create a heat and humidity transfer model between the Chinese cabbage and the flowing humid air. The calculations utilize the heat transfer model in porous medium, which includes the temperature difference between the solid (vegetable tissue) and fluid (air) phases of the porous medium. Modelling and calculations were performed in ANSYS Fluent 14.5 software.

Dominik Sawicki, Eugeniusz Zieniuk
Parametric Integral Equations Systems Method in Solving Unsteady Heat Transfer Problems for Laser Heated Materials

One of the most popular applications of high power lasers is heating of the surface layer of a material, in order to change its properties. Numerical methods allow an easy and fast way to simulate the heating process inside of the material. The most popular numerical methods FEM and BEM, used to simulate this kind of processes have one fundamental defect, which is the necessity of discretization of the boundary or the domain. An alternative to avoid the mentioned problem are parametric integral equations systems (PIES), which do not require classical discretization of the boundary and the domain while being numerically solved. PIES method was previously used with success to solve steady-state problems, as well as transient heat transfer problems. The purpose of this paper is to test the efficacy of the PIES method with time discretization in solving problem of laser heating of a material, with different pulse shape approximation functions.

Piotr Czarnocki, Kamila Czajkowska
Delamination Resistance of Laminate Made with VBO MTM46/HTS Prepreg

A laminate made with the Vacuum Bag Only (VBO) prepregs can be cured out of autoclave. Because of low curing pressure such a process can result in deterioration of laminate mechanical properties. They can be significantly lower than those displayed by the autoclave cured ones. The resistance against delamination can be among the most affected. Since this property is a week point of all the laminates it was of particular interest. Delamination resistance of unidirectional laminate made from VBO MTM46/HTS(12K) prepreg was in the scope of the presented research and the critical values of the Strain Energy Release Rates and the Paris-type equations corresponding to Mode I, Mode II and Mixed-Mode I/II static and cyclic loadings, respectively, were determined.

Heorhiy Sulym, Lyubov Piskozub, Yosyf Piskozub, Yaroslav Pasternak
Antiplane Deformation of a Bimaterial Containing an Interfacial Crack with the Account of Friction. 2. Repeating and Cyclic Loading

The paper presents the exact solution of the antiplane problem for an inhomogeneous bimaterial with the interface crack exposed to the normal load and cyclic loading by a concentrated force in the longitudinal direction. Using discontinuity function method the problem is reduced to the solution of singular integral equations for the displacement and stress discontinuities at the domains with sliding friction. The paper provides the analysis of the effect of friction and loading parameters on the size of these zones. Hysteretic behaviour of the stress and displacement discontinuities in these domains is observed.

APPLICATION OF CFD TO MODELING OF SQUEEZE MODE MAGNETORHEOLOGICAL DAMPERS

Janusz GOŁDASZ[*,], Bogdan SAPIŃSKI[***]**

[*]BWI Group, Technical Center Kraków, ul. Podgórki Tynieckie 2, 30-399 Cracow, Poland
[**]Department of Automation and Information Technology, Cracow University of Technology, ul. Warszawska 24, 31-155 Cracow, Poland
[***]Department of Process Control, AGH University of Science and Technology, al. Mickiewicza 30-059 Cracow, olnd

jgoldasz@pk.edu.pl, deep@agh.edu.pl

received 12 May 2015, revised 30 July 2015, accepted 7 Sempember 2015

Abstract: The so-called squeeze flow involves a magnetorheological (MR) fluid sandwiched between two planar surfaces setting up a flow channel. The height of the channel varies according to a prescribed displacement or force profile. When exposed to a magnetic field of sufficient strength MR fluids develop a yield stress. In squeeze-mode devices the yield stress varies with both the magnetic field magnitude and the channel height. In this paper an unsteady flow model of an MR fluid in squeeze mode is proposed. The model is developed in Ansys Fluent R16. The MR material flow model is based on the apparent viscosity approach. In order to investigate the material's behaviour the authors prepared a model of an idealized squeeze-mode damper in which the fluid flow is enforced by varying the height of the channel. Using mesh animation, the model plate is excited, and as the mesh moves, the fluid is squeezed out of the gap. In the simulations the model is subjected to a range of displacement inputs of frequencies from 10 to 20 Hz, and local yield stress levels up to 30 kPa. The results are presented in the form of time histories of the normal force on the squeezing plate and loops of force vs. displacement (velocity).

Key words: Magnetorheological Fluid, Damper, Squeeze-Mode, Computational Fluid Dynamics, Mesh Animation

1. INTRODUCTION

The MR effect is manifested by changes in the material's apparent viscosity when exposed to magnetic field. This feature has made it more than welcome in semi-active control systems and automotive applications in particular. The MR material has been basis for developing hardware and applications also in the real world and not only the academia. By examining the manner in which the material operates it is now well understood the material may operate in any of the operation modes: flow-mode, shear-mode, squeeze-mode (Jolly et al., 1996; Jolly and Carlson, 1996). Real-world examples of flow-mode hardware include automotive dampers and powertrain mounts. Rotary devices are controllable brakes and clutches. The squeeze-mode utilizes an MR fluid that is trapped in a flow channel whose height varies according to a prescribed displacement profile on either surface of the channel. The fluid is squeezed out of the gap simple by the plate motion. This particular operation mode may provide optimum performance when implemented in small-stroke dampers or vibration mounts. At the same time a successful application of squeeze-mode requires a mathematical model of the phenomena for fast sizing of prototypes at a design stage of the development process. Analytical models based on the classic Bingham approach (Gołdasz and Sapiński, 2015) are rather limited in scope, and the solutions have been made available in few idealized cases, e.g. simple geometry. CFD (Computational Fluid Dynamics) tools offer a modeling potential that can be realized within a reasonable time constraint, although full scale unsteady flow problems are a challenge, too.

CFD or finite-element studies on devices utilizing MR fluids are rare, e.g. (Case et al., 2013, Chen et al., 2007; Zheng et al., 2014), and on squeeze-mode devices even so (Gstottenbauer et al., 2008; Sapiński and Szczęch, 2013). Therefore, there is a need to address the problem of developing a model procedure for use with more complex case studies. In this study the authors apply an apparent viscosity model to a simple 2D axi-symmetric model of an idealized squeeze-mode damper geometry. The unsteady behavior of the incompressible fluid in squeeze flow is then studied using mesh animation techniques. The calculations are performed for a material in which the magnetic field-induced yield stress is allowed to vary in terms of the flow channel height

2. MODELING

In this section the authors was presented Navier-Stokes equation and the apparent viscosity model. Additionaly, the geometry of the damper, yield stress vs. gap height characteristics were highlighted.

2.1. Theory

The behaviour of MR fluids in flow can be studied using well-known Navier-Stokes (N-S) equations. Their tensor form is (Tannehi et al., 1996)

$$\rho\frac{\partial u_i}{\partial t}+\rho u_j\frac{\partial u_i}{\partial x_j}=-\frac{\partial p}{\partial x_i}+\frac{\partial \tau_{i,j}}{\partial x_j}, \tag{1}$$

where: τ – shear stress, ρ – density, u – velocity, p – pressure, and x_i is the independent variable (i=1,2,3). In N-S equations flow problems concerning specific materials are handled by the sheear stress term. In the case of MR fluids, using the Bingham model and defining the apparent viscosity as the ratio of the fluid's yield stress over the local shear rate the following expression is

DOI 10.1515/ama-2015-0021

$$\mu_{app} = \mu + \frac{\tau_0}{\left|\frac{\partial u_i}{\partial x_j}\right|} \tag{2}$$

and the yield stress term

$$\tau_{i,j} = \mu_{app} \frac{\partial u_i}{\partial x_j}, \tag{3}$$

where: τ_0 – yield stress, μ_{app} – apparent viscosity, μ – base viscosity. The yield stress is allowed to vary in terms of space and magnitude. The model in Equation (2) has a discontinuity when the shear rate is zero which makes flow problems impossible to solve in these conditions. Solutions (Chen et al., 2007) suggest imposing an upper bound on the apparent viscosity term (2) when shear rate approaches zero. In the present model the upper bound is chosen to be 1000 times the base viscosity of the fluid. In Ansys Fluent this approach can be programmed into an user-defined function.

2.2. Analytical solution

Sproston et al. (1994) and Zhang et al. (2011) obtained an analytical solution for ER/MR fluids in squeeze-flow. In this paper the expression obtained by Zhang is further utilized in subsequent calculations. It is an extension of Stefan model (de Vincente et al., 2011; Esmonde et al., 2009; Farjoud et al., 2011) incl. the effects of viscosity, plasticity, and inertia (acceleration)

$$F_{MR} = F_v + F_\tau - F_i \tag{4}$$

and

$$F_v = 3\frac{\mu\pi R_p^4}{2(h_0+z)^3} v_z, \tag{5}$$

$$F_\tau = 3\frac{\pi R_p^3 \tau_0}{4(h_0+z)} \mathrm{sgn}(v_z), \tag{6}$$

$$F_i = 3\frac{\pi R_p^4 \rho a_z}{8(h_0+z)}, \tag{7}$$

Where: R_p – plate radius, h_0 – initial gap, a_z – acceleration, F_{MR} – normal force, F_v – viscous force, F_i – inertial force, F_τ – force due to yield stress. In this study results obtained using the analytical expression given by Equation (4) are compared against CFD.

2.3. Input data

Consider the 2D axi-symmetric geometry in Fig. 1. The outer rectange denotes the fluid domain, and the inner wall boundary refers to a circular flat plate that is constrained to move vertically according to the prescribed displacement profile $h(t)$. The fluid region directly underneath the plate is characterized by a volume of non-zero yield stress, whereas zero yield stress in imposed in the other portion of the fluid. The outer diameter D_p of the plate is 64 mm, and the initial gap height h_0 = 3.38 mm. The CFD model is setup with wall boundary conditions on the outer and the inner boundary. Mesh is animated on the inner boundary in order to simulate flow conditions of a fluid subjected to external kinetic (as well as magnetic) excitation inputs.

In the simulated study the authors assumed fluid properties similar to the BASF's 4035 MR material with 26% Fe vol (Kieburg, 2010). The density of the fluid is 2.6 g/cc, and the base viscosity μ = 50 cP.

The region of the fluid underneath the plate is assumed to be characterized by a magnetic field supplied from a virtual core assembly with a coil of N =150 wire turns. With the current range from 0 to 3 A, the fluid's yield stress vs. height characteristics can be estimated in Fig. 2. The arrows in the figure indicate the operating range of this virtual device; the minimum gap height was 1.94 mm, and the maximum height was 4.82 mm.

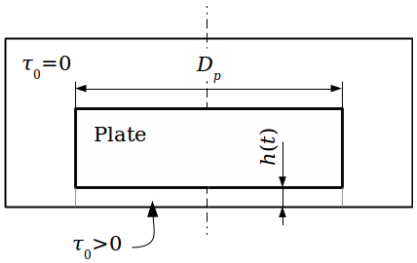

Fig. 1. CFD model schematic layout

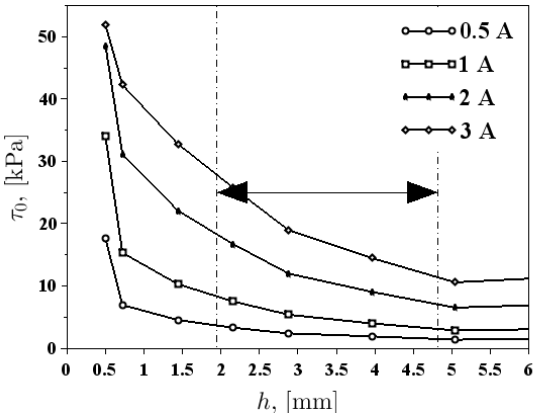

Fig. 2. Calculated yield stress vs. channel height, $\tau_0(h)$

To summarize, the series of simulated experiments incorporated two stages. The first one assumed constant yield stress of the fluid (regardless of the channel height), whereas as the second part utilized the variable yield stress model according to Fig. 2. The external excitation was in the form of sinusoidal displacement input applied to the inner boundary (plate). Given the initial gap size the gap height varied according to $h(t) = h_0 + z(t) = h_0 + cos(2\pi ft + \pi/2)$, where z – plate displacement, z_m – displacement amplitude, f – frequency. The maximum aplitude of the displacement input was 1.44 mm, and the frequency range was from 10 Hz to 20 Hz, thus translating into peak velocities of the plate to be appr. 200 mm/s. In the CFD model the force is assumed to be positive in compression (downward motion).

2.4. Results

The section contains simulation results by means of Ansys Fluent R16. Unsteady flow equations were handled at the constant time step of 0.04 ms. The data are presented in the form of plots of force vs. displacement (velocity) in Figs. 3-11.

To provide force estimate, pressure distribution was integrated across the entire surface area below the plate.

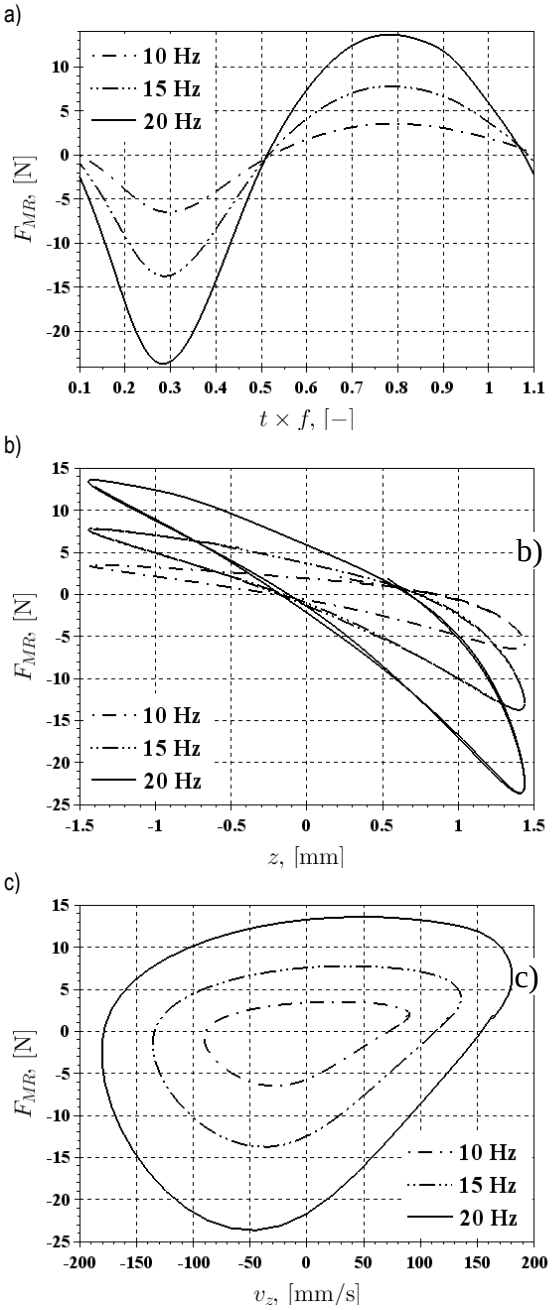

Fig. 3. Non-energized condition: τ_0 = 0 kPa, f = {10, 15, 20 Hz}, a) F_{MR} vs. t, b) F_{MR} vs. z, c) F_{MR} vs. v_z

Specifically, constant yield stress scenarios are revealed in Figs. 3-6. The effect of frequency can be studied by considering the results in Figs. 7-9. Next, a comparison of CFD results against the analytical squeeze-flow model as in Equation (4) is given in Fig. 10. Finally, variable yield stress cases are illustrated in Fig. 11. With the exception of Fig. 3. all illustrations show only the positive force output. Tensile forces were beyond the scope of this study. In Fig. 3a the simulation time t is scaled by the input frequency f to enable a direct comparison of the obtained results regardless of the kinetic excitation conditions. Fig. 3 reveals small yet noticeable effects of inertia manifested by a rotation of the force vs. displacement ellipse in Fig. 3b and the increase in the force vs. velocity hysteresis as in Fig. 3c.

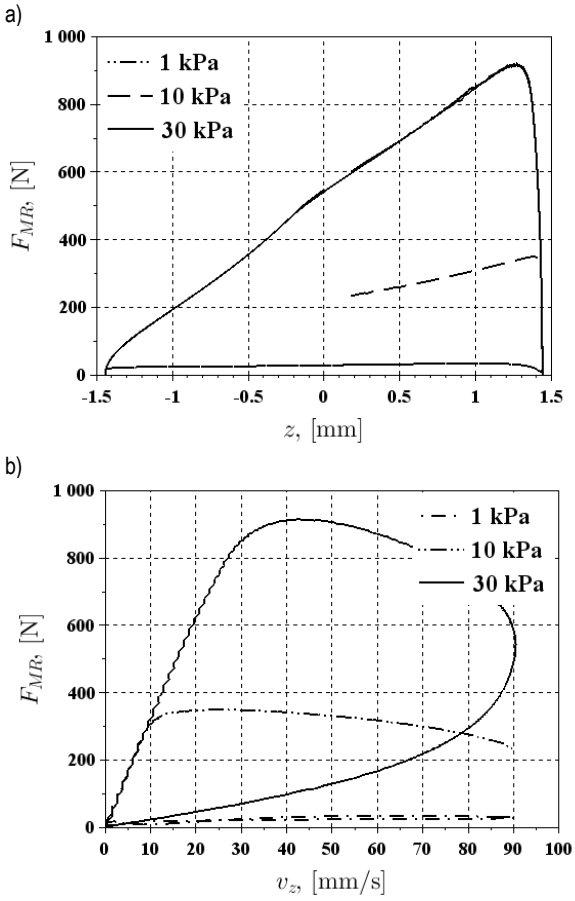

Fig. 4. Constant yield stress: f = 10 Hz, a) F_{MR} vs. z, b) F_{MR} vs. v_z

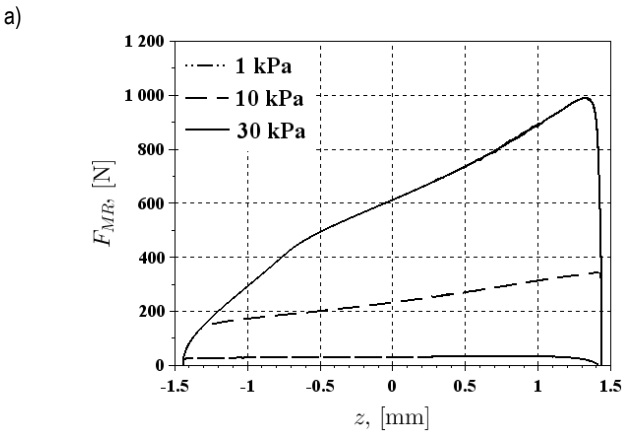

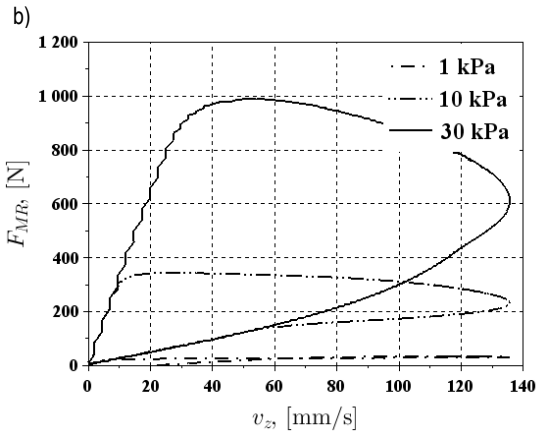

Fig. 5. Constant yield stress: f = 15 Hz, a) F_{MR} vs. z, b) F_{MR} vs. v_z

DOI 10.1515/ama-2015-0021

Constant non-zero yield stress results in Figs. 4, 5 and 6 were performed for three frequencies (10, 15, 20) Hz and three distinct levels of the yield stress (1, 10, 30) kPa, respectively. Specifically, 20 Hz data in Fig. 6 reveal an appr. 100 N increase in the force due to higher shear rates. The 30 kPa curve in Fig. 6 also shows a dual rate behavior that is almost absent in the corresponding data set in Fig. 4. The dual-rate feature is representative of the bi-viscous implementation of the apparent viscosity model in Fluent. Effectively, the model response in low frequency and high yield stress scenarios may be underestimated The effect is yet to be studied in detail, however, the initial observation is consistent with other data obtained using the same apparent viscosity model (Farjoud et al., 2011). In all cases the force shows a strong dependence on piston position. That is evident when observing a large hysteresis in force vs. velocity loops in Figs. 4-6. For comparison in Figs. 7-9 the influence of frequency (and velocity) can be observed and analyzed. Specifically, Fig. 7 reveals the model output at the constant yield stress of 1 kPa and the three frequencies, respectively. Fig. 8 illustrates the 10 kPa case, and Fig. 9 illustrates the behavior of the fluid whose yield stress was 30 kPa.

a) b)

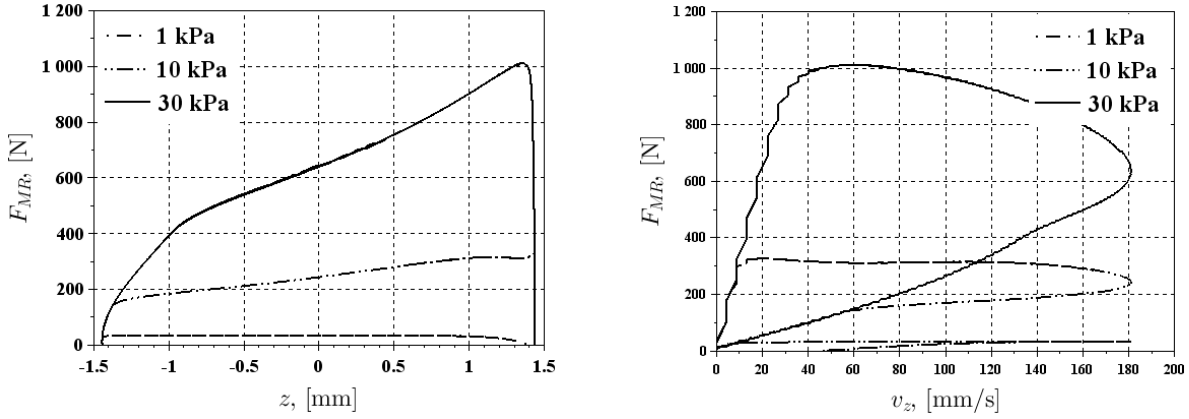

Fig. 6. Constant yield stress: f = 20 Hz, a) F_{MR} vs. z, b) F_{MR} vs. v_z

a) b)

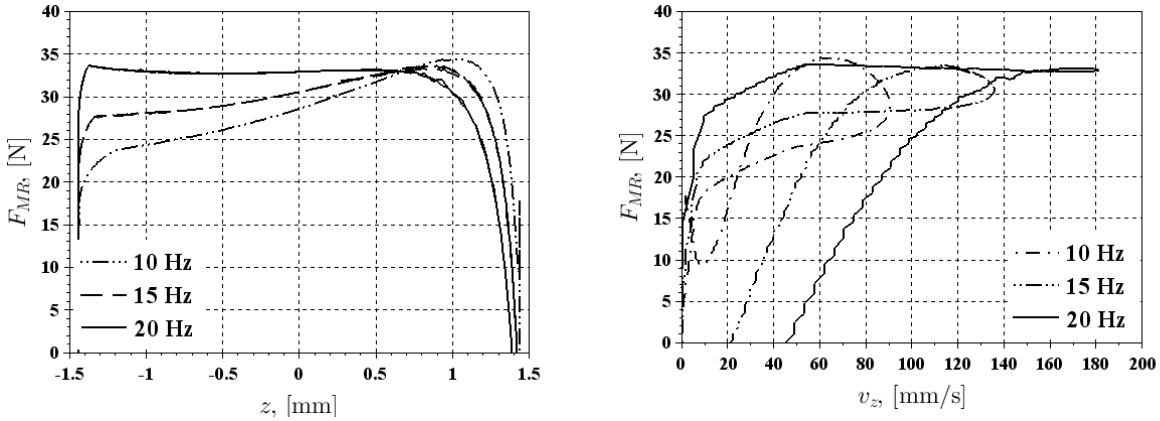

Fig. 7. Effect of frequency: τ_0 = 1 kPa, a) F_{MR} vs. z, b) F_{MR} vs. v_z

a) b)

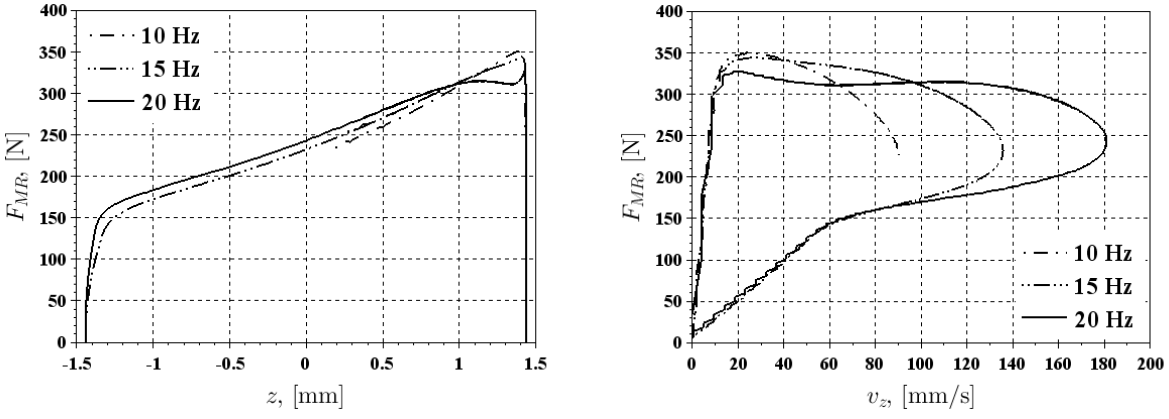

Fig. 8. Effect of frequency: τ_0 = 10 kPa, a) F_{MR} vs. z, b) F_{MR} vs. v_z

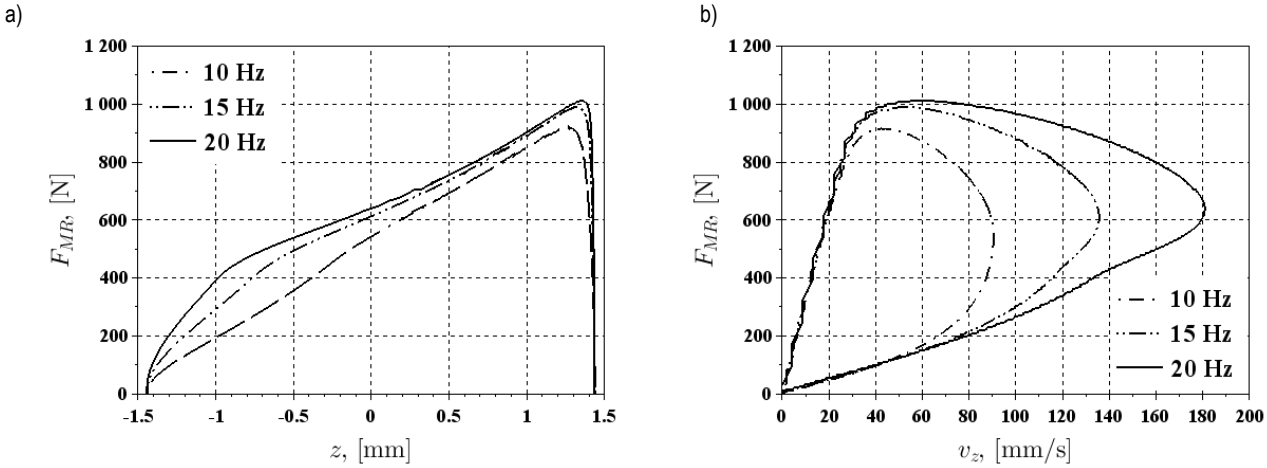

Fig. 9. Effect of frequency: τ_0 = 30 kPa, a) F_{MR} vs. z, b) F_{MR} vs. v_z

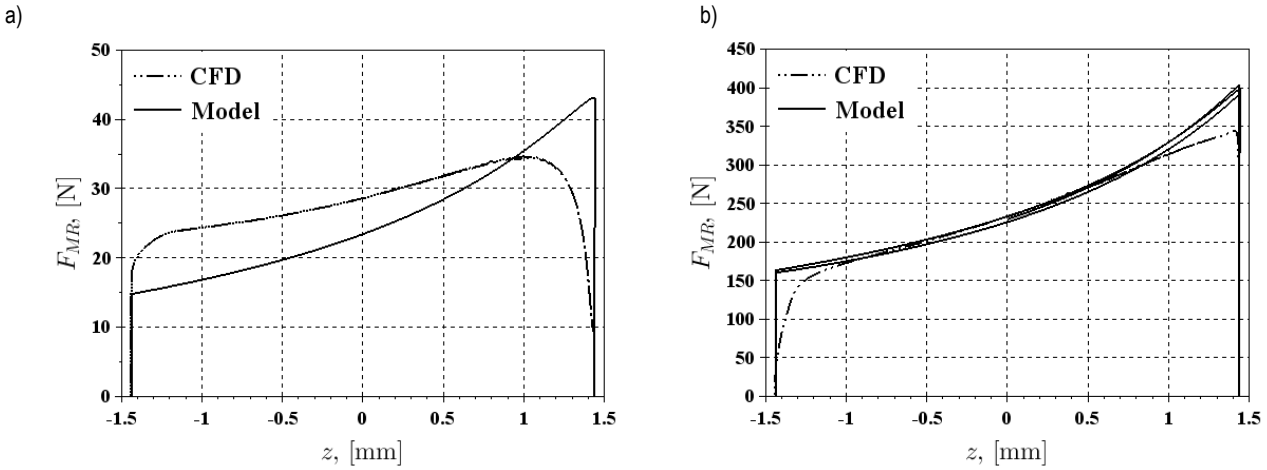

Fig. 10. Comparison: analytical model vs. CFD results, a) f = 10 Hz, τ_0 = 1 kPa, b) f = 15 Hz, τ_0 = 10 kPa

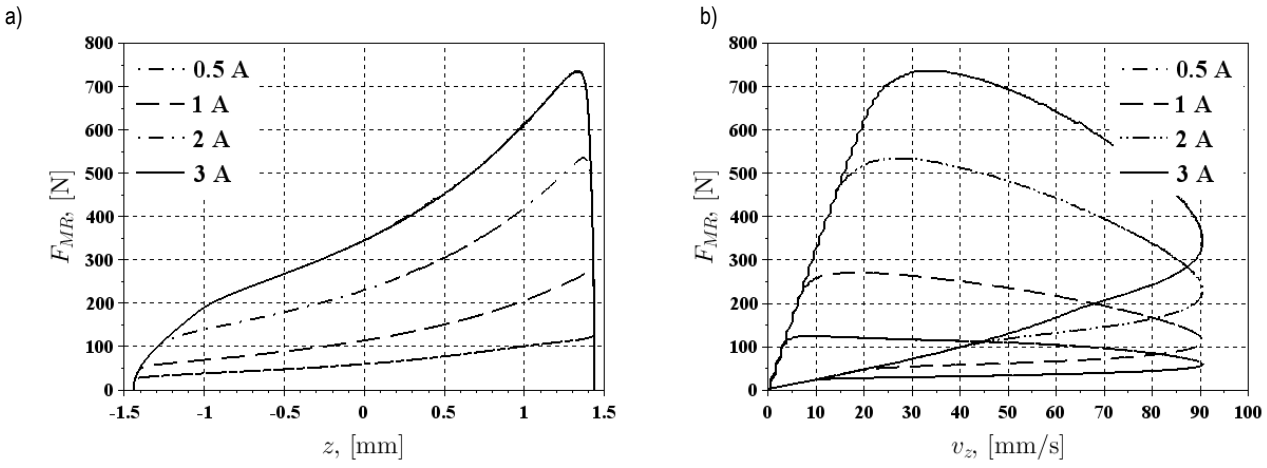

Fig. 11. Variable yield stress, τ_0 = var, f = 10 Hz, a) F_{MR} vs. z, b) F_{MR} vs. v_z

To validate the CFD model the obtained results were compared against the analytical expression given by Equation (4). The results are revealed in Fig. 10. In general, the illustrations show good agreement of the CFD output against the analytical theory. Discrepancies are at the extreme positions of the displacement range. The behavior is due to the bi-viscous character of the CFD solution, and is yet to be confirmed when analyzing the model performance against real data in near future. Finally, variable yield stress scenarios were considered in which the yield stress τ0 was allows to vary in terms of the control gap height and current supplied by a virtual coil. The current range was from 0.5 A to 3 A. The output is presented in Fig. 11. The effect of yield stress increase can be clearly seen in the revealed data. In the data the increase in the F_τ component with plate-to-base distance is accompanied by the effect of augmenting the yield stress due to position at current level.

DOI 10.1515/ama-2015-0021

3. CONCLUSIONS

This study concerned a CFD experiment involving an MR fluid subjected to compressive loads. In general, the model confirms the well-known fact that as the gap height decreases, compressive loads increase. Specifically, the authors developed a CFD model based on the apparent viscosity approach and tested its performance under constant yield stress conditions and variable yield stress conditions, respectively. A comparison of the CFD data against theory was made, too, in order to draw conclusions on the model limitations and operation range. It is clear from the data that the Fluent model underestimates the analytical solution at near-zero velocity points, however, good agreement is obtained in all presented cases. The results provide a reasonable base for future work with real devices and fluids.

REFERENCES

1. **Case D., Taheri, B., Richer, E.** (2013), Multiphysics modeling of magnetorheological dampers, *The International Journal of Multiphysics*, Vol. 7, No. 1, 61-76.
2. **Chen S. M., Bullough W. A., Ellam D. J.** (2007), Examination of through flow in a radial ESF clutch, *Journal of Intelligent Material Systems and Structures*, Vol. 12, 1175–1179.
3. **de Vicente, Juan, et al.** (2011), Squeeze flow magnetorheology, *Journal of Rheology* (*1978-present*), Vol. 55, No. 4, 753-779.
4. **Esmonde, H., H. See, and M. V. Swain** (2009), Modelling of ER squeeze films at low amplitude oscillations, *Journal of Non-Newtonian Fluid Mechanics*, Vol. 161, No. 1, 101-108.
5. **Farjoud, A., Ahmadian, M., Mahmoodi, N., Zhang, X., & Craft, M.** (2011), Nonlinear modeling and testing of magneto-rheological fluids in low shear rate squeezing flows, *Smart Materials and Structures*, Vol. 20, No. 8, 085013.
6. **Gołdasz J., Sapiński B.** (2015), *Insight into magnetorheological shock absorbers*, Springer Publishing, Heidelberg.
7. **Gstottenbauer, N., Kainz, A., Manhartsgruber, B., Scheidl, R.** (2008), Experimental and numerical studies of squeeze-mode behaviour of magnetic fluid, *Proceedings of the Institution of Mechanical Engineers, Part C: Journal of Mechanical Engineering Science*, Vol. 22, No. 12, 2395-2407.
8. **Jolly M., Bender J. W., Carlson J. D.** (1996), Properties and applications of magnetorheological fluids, *Proceedings of the SPIE Conference of the International Society of Optical Engineers*, Vol. 3327, 262–275.
9. **Jolly M., Carlson J. D.** (1996), Controllable squeeze-film damping using magnetorheological fluids, *Proceedings of the 5th International Conference on New Actuators, Bremen, 333–336.*
10. **Kieburg Ch.** (2010), MR Fluid Basonetic 4035, *BASF Technical Information.*
11. **Sapiński, B., Szczęch, M.** (2013), CFD model of a magnetorheological fluid in squeeze mode, *acta mechanica et automatica*, Vol. 7, No. 3, 180-183.
12. **Sproston J. L., Rigby S. G., Wiliams E. W., Stanway R.** (1994), A numerical simulation of electrorheological fluids in oscillatory compressive squeeze-flow, *Journal of Physics D: Applied Physics*, Vol. 2, No. 27, 338–340.
13. **Tannehill J. C., Anderson D. A., Pletcher R. H.** *(*1996*), Computational fluid mechanics and heat transfer.* Taylor and Francis, New York.
14. **Zhang X. J., Farjoud A., Ahmadian M, Guo K. H., Craft M.** (2011), Dynamic testing and modeling of an MR squeeze mount, *Journal of Intelligent Material Systems and Structures*, Vol. 22, No. 15, 1717–1728.
15. **Zheng, J., Li, Z., Koo, J., Wang, J.** (2014), Magnetic circuit design and multiphysics analysis of a novel MR damper for applications under high velocity. *Advances in Mechanical Engineering*, Vol. 2014, 402501.

The work has been accomplished within the scope of the research project No. PBS 1/A6/3/2012 sponsored by the National Center for Research and Development (Poland).

DOI 10.1515/ama-2015-0022 acta mechanica et automatica, vol.9 no.3 (2015)

ON THE STRESS FREE DEFORMATION OF LINEAR FGM INTERFACE UNDER CONSTANT TEMPERATURE

Artur GANCZARSKI*, Damian SZUBARTOWSKI*

*Institute of Applied Mechanics, Department of Mechanical Engineering, Cracow University of Technology, 31-864 Kraków, al. Jana Pawła II 37, Poland

artur.ganczarski@pk.edu.pl, tszubartowski@o2.pl

received 24 February 2015, revised 9 October 2015, accepted 14 October 2015

Abstract: This paper demonstrates the stress free thermo-elastic problem of the FGM thick plate. Existence of such a purely thermal deformation is proved in two ways. First proof is based on application of the Iljushin thermo-elastic potential to displacement type system of equations. This reduces 3D problem to the plane stress state problem. Next it is shown that the unique solution fulfils conditions of simultaneous constant temperature and linear gradation of thermal expansion coefficient. Second proof is based directly on stress type system of equations which straightforwardly reduces to compatibility equations for purely thermal deformation. This occurs if only stress field is homogeneous in domain and at boundary. Finally an example of application to an engineering problem is presented.

Key words: Linear FGM Interface, Stress Free Deformation

1. INTRODUCTION

Functionally graded materials (FGMs) provide thermal insulation and mechanical toughness at high temperature by varying the composition of thermal conductivity coefficient, thermal expansion coefficient and Young's modulus from high temperature side to low temperature side continuously and simultaneously by removing the discontinuity of layered plate. These advantages cause that FGMs are applicable in many fields such as high performance engines for aerospace vehicles, turbine blades and heat-resisting tools. A general overview of thermal stresses in FGMs comprises work by Noda (1999).

Numerous analytical solutions of thermo-elastic plane or three-dimensional problems of FGMs take advantage of specific power or exponential function approximation methods of multilayered composite plate, limiting simultaneously their generality and suggesting question how to reduce the problem. One way to attain this may be proving theorem on the stress free deformation accompanying linear gradation of thermo-mechanical properties of the material staying in constant temperature condition. Such a proof can be done following two ways taking advantage of either displacement or stress formulation of thermo-elastic equations. In the first case lemma consists in generalization of theorem on the plane stress state in an isotropic thermo-elastic thick plate, originally proved by Sneddon and Lockett (1960). The authors presented convinced proof for a problem of semi-infinite thermo-elastic medium bounded by two parallel planes and loaded by an arbitrary temperature field on one surface. The method of solution employed was the double Fourier transform. The results confirmed solution of analogous problems, being inspiration to their work, received earlier by Sternberg and McDowell (1957), based on Green's function, and by Muki (1957), who used method combining the theory of Fourier series and the Hankel transforms of integral order. Also there exists other more elegant way, based on application of Iljushin's potential (Iljushin et al., 1979), which is demonstrated in the present work. Final step of the proof of theorem relays on pointing out that unique solution of the plane stress equations, that satisfy homogeneous boundary conditions, guarantees stress free deformation if only temperature field is constant and gradation of thermal expansion coefficient is linear function.

In the other case, when stress formulation of thermo-elastic equations is used, the proof of theorem is almost elementary and turns out to be straightforward analogy to these which were done by Fung (1965) and Nowacki (1970) for homogeneous material.

2. FGM'S – CONCEPT, FABRICATION, PROPERTIES AND NUMERICAL MODELING

In many applications, especially in the space industry as well as electronic industry, structures or part of structures are exposed to high temperature, usually up to 2000K or even 3500K in some parts of rocket engines, see Schulz et al. (2003), high temperature gradients, and/or cyclic temperature changes. Conventional metallic materials, such as carbon steels or stainless steels: ASTM 321, ASTM 310, nickel- or aluminium-based alloys cannot resist such high temperatures, see Odqvist (1966). The first method to improve the resistance of metallic structures against extreme temperature conditions consists in covering the structure with a ceramic layer since ceramics are known for their high thermal resistance. For instance, in a metal-ceramic composite: Al-SiC the thermal conductivities ratio is approximately equal: $\lambda_{\mathrm{m}}/\lambda_{\mathrm{c}} = 3.6$, the thermal expansion coefficients ratio: $\alpha_{\mathrm{m}}/\alpha_{\mathrm{c}} = 5$, whereas the elastic moduli ratio: $E_m/E_{\mathrm{c}} = 0.16$, see Potarescu and Sugano (1993). Indices m and c refer to matrix and ceramic mate-

DOI 10.1515/ama-2015-0022

rials respectively. Hence, at the metal-ceramic interface, severe discontinuity of thermo-mechanical properties occurs, which results in high strain and stress mismatch at the interface. As a consequence, delamination or failure of the coating is rapidly observed. As a remedy to these disadvantages the concept of Functionally Graded Materials - FGM, was developed in Japan in the 1980s, see Yamanouchi et al. (1990), giving structural components a spatial gradient in thermo-mechanical properties. The spatial gradient is achieved by use of two-component composites. The volume fraction of the composite constituents varies spatially such that the effective thermo-mechanical properties change smoothly from one material (ceramic) to the other (metal). In this way, in the case of a Thermal Barrier Coating deposited on a metallic substrate, the heat-resistant ceramic layer and the solid metal are separated by functionally graded FG layer, the composition of which varies from pure ceramic to pure metal. The processing technologies for TBCs and FGMs may lead to residual stresses, which are built-in during cool-down from the elevated fabrication temperature. These residual stresses may be significant relative to thermo-mechanical stresses applied subsequently. As regards FG layer processing, Plasma Spray Thermal Barrier Coating leads to lamellar microstructures, whereas columnar-lamellar microstructures are produced when using Electron Beam Physical Vapour Deposition, see Lee et al. (1996), Schulz et al. (2003).

A general review article on the application of the several ceramic materials to TBCs is given by Lee et al. (1996). Selected thermo-mechanical properties as elastic modulus E and both thermal expansion α and conductivity λ coefficients are summarized in Table 1 for two alumina-based composites, see Chen and Tong (2004), Cho and Shin (2004) for Ni-Al_2O_3 and Wang et al. (2000) for Ti-Al_2O_3.

Tab. 1. Comparison of properties of constituents of two alumina-based composites Ni-Al_2O_3 (Hen and Tong, 2004; Cho and Shin, 2004) and Ti-Al_2O_3 (Wang et al., 2000)

Composite	E [GPa]	λ [W/mK]	$\alpha \cdot 10^{-6}$ [1/K]
Ni	199.5	90.7	13.3
Al_2O_3	393.0	30.7	8.8
Al	73	154	23
Al_2O_3	380	46	8.5

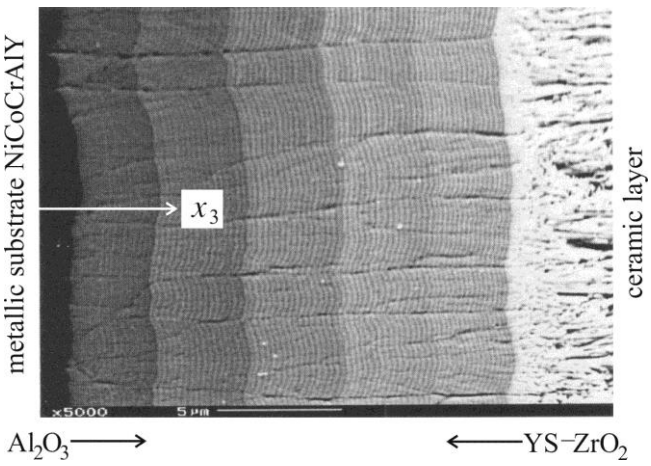

Fig. 1. Microstructure of chemically graded Electron Beam Physical Vapour Deposition thermal barrier coating, after Schulz et al. (2003)

When the classical FEM based on homogeneous elements is used for FGMs, the material properties stay the same for all integration points belonging to one finite element. This means that material properties may vary in a piecewise continuous manner, from one element to the other and a unique possibility to model FGM structure is approximation by use of appropriately fine mesh. On the other hand, a too coarse mesh may lead to unrealistic stresses at the interface between the subsequent layers. To overcome this difficulty a special graded element has been introduced by Kim and Paulino (2002) to discretize FGM properties. The material properties at Gauss quadrature points are interpolated there from the nodal material properties by the use of isoparametric interpolation functions. Contrary to the classical FEM formulation, the stiffness matrix of an element is expressed by the integral in which constitutive matrix is a function of the coordinates. In the original formulation the same shape functions are used for approximation of the displacement field and material inhomogeneity. However, from the numerical point of view nothing stands in the way of implementation of shape functions referring directly to the individual character of inhomogeneity, for instance power functions, see Akai et al. (2005) or exponential functions, see Bagri et al. (2005).

3. THE GENERAL FORMULATION OF FGM THERMO-ELASTIC PROBLEM

A thermo-elastic body under consideration (Fig.1) is bounded by two parallel planes normal to axis x_3, and its thermo-mechanical properties such as thermal conductivity coefficient, thermal expansion coefficient and Young's (Kirchhoff's) modulus are optional functions of x_3

$$\lambda = \lambda(x_3) \quad \alpha = \alpha(x_3) \quad E = E(x_3) \qquad G = G(x_3). \tag{1}$$

Since $E(x_3)$ and $G(x_3)$ are controlled by the same function of x_3 the Poisson ratio is considered as independent of x_3 and satisfying classical relation

$$\nu = \frac{E}{2G} - 1. \tag{2}$$

This guarantees isotropy (two independent material constants) on one hand and simultaneously prevents from some peculiar effects occurring on the other hand, see Ganczarski and Barwacz (2004).

The body is established a temperature field $T + \theta(x_i)$, where T stands for the temperature of the solid corresponding to zero stress and strain. Also it is assumed that there are no body forces within the solid and that its surfaces are free from tractions.

The system of equations of uncoupled thermo-elasticity expressed in displacements takes the form

$$\begin{aligned}
&\nabla^2 u_i + \frac{1}{1-2\nu}\frac{\partial \Theta}{\partial x_i} + \underline{\frac{1}{G}\frac{\partial G}{\partial x_3}\left(\frac{\partial u_i}{\partial x_3} + \frac{\partial u_3}{\partial x_i}\right)} = 2\frac{1+\nu}{1-2\nu}\frac{\partial(\propto\theta)}{\partial x_i},\\
&\nabla^2 u_3 + \frac{1}{1-2\nu}\frac{\partial \Theta}{\partial x_3} + \underline{\frac{2}{G}\frac{\partial G}{\partial x_3}\left(\frac{\partial u_3}{\partial x_3} + \frac{\nu\theta}{1-2\nu}\right)} = 2\frac{1+\nu}{1-2\nu} \qquad (3)\\
&\times\left[\frac{\partial(\propto\theta)}{\partial x_3} + \underline{\frac{1}{E}\frac{\partial E}{\partial x_3}\alpha\theta}\right],\\
&\nabla^2\theta + \underline{\frac{1}{\lambda}\frac{\partial \lambda}{\partial x_3}\frac{\partial \theta}{\partial x_3}} = 0,
\end{aligned}$$

where u_i denotes the displacement vector, and $\Theta = \mathrm{grad}(u_i)$

is the dilatation. The underlined terms in Eqs (3) yield of FGM application and they are additional in comparison with classical formulation of homogeneous material. The relation between the stress tensor σ_{ij} and the displacement vector u_i is given by the Duhamel-Neumann equation

$$\sigma_{ij} = G\left[\frac{\partial u_i}{\partial x_j} + \frac{\partial u_j}{\partial x_i} + 2\left(\frac{\nu(\Theta-3\alpha\theta)}{1-2\nu} - \alpha\theta\right)\delta_{ij}\right]. \tag{4}$$

The variation of temperature θ throughout the solid is determined by steady Fourier equation Eq. (3_3) in case of absence of inner heat sources.

System of equations expressed in stresses (extension of Beltrami-Michell formulation) equivalent to (3) is as follows

$$\begin{aligned}
&\nabla^2\sigma_{ii} + \frac{1}{1+\nu}\left[\frac{\partial^2 s}{\partial x_i^2} - \nabla^2 s\right] - 2E\frac{\partial}{\partial x_3}\left(\frac{1}{E}\right)\left[\frac{\partial \sigma_{jj}}{\partial x_3} - \frac{\nu}{1+\nu}\frac{\partial s}{\partial x_3}\right]\\
&\quad -E\frac{\partial^2}{\partial x_3^2}\left(\frac{1}{E}\right)\left[\sigma_{jj} - \frac{\nu}{1+\nu}s\right]\\
&\quad +\frac{E}{1+\nu}\left[\frac{\partial^2(\alpha\theta)}{\partial x_i^2} - \nabla^2(\alpha\theta)\right] = 0 \qquad i,j = 1,2,\\
&\nabla^2\sigma_{33} + \frac{1}{1+\nu}\left[\frac{\partial^2 s}{\partial x_3^2} - \nabla^2 s\right] + \frac{E}{1+\nu}\left[\frac{\partial^2(\alpha\theta)}{\partial x_3^2} - \nabla^2(\alpha\theta)\right] = 0,\\
&\nabla^2\tau_{ij} + \frac{1}{1+\nu}\frac{\partial^2 s}{\partial x_i x_j} + \frac{\partial}{\partial x_3}\left(\frac{1}{E}\right)\left[\frac{\partial \sigma_{kk}}{\partial x_i} - \frac{1}{1+\nu}\frac{\partial s}{\partial x_i} - \frac{\partial \tau_{ki}}{\partial x_k}\right]\\
&\quad +\frac{E}{1+\nu}\frac{\partial^2(\alpha\theta)}{\partial x_i x_j} = 0 \qquad i,j,k = 1,2,3 \quad i \neq j \neq k,\\
&\nabla^2\theta + \frac{1}{\lambda}\frac{\partial\lambda}{\partial x_3}\frac{\partial\theta}{\partial x_3} = 0,
\end{aligned} \tag{5}$$

where $s = \mathrm{tr}(\sigma) = \sigma_{11} + \sigma_{22} + \sigma_{33}$. It worth to notice that equations ($5_{1\text{-}3}$) can be obtained either in classical way or directly from equations ($3_{1\text{-}2}$) according to concept by Ignaczak (1959).

4. CONDITIONS OF EXISTENCE OF STRESS FREE DEFORMATION

4.1. Proof based on displacement formulation

To solve Eqs (3) the following potential, originally proposed by Iljushin et al. [8], is introduced

$$\begin{aligned}
&u_i = \frac{\partial\phi}{\partial x_i}, \quad u_3 = -\frac{\partial\phi}{\partial x_3} + f(x_3)\\
&f(x_3) = Ax_3^2 + Bx_3 + C\\
&\alpha\Theta = 2\frac{1-\nu}{1+\nu}Ax_3 - \frac{1}{1+\nu}\frac{\partial^2\phi}{\partial x_3^2},
\end{aligned} \tag{6}$$

where function of displacement potential ϕ is of harmonic type

$$\nabla^2\phi = 0 \tag{7}$$

and A, B, and C are constants.

Simple introducing of definitions (6) to Eqs (3) shows that only equations of mechanical state are satisfied as identity, contrary to the case of homogeneous material, when also the equation of thermal state is satisfied as identity

$$\begin{aligned}
&\frac{\partial}{\partial x_i}\underbrace{(\nabla^2\phi)}_{=0} + \frac{1}{1-2\nu}\frac{\partial}{\partial x_i}\left(\underbrace{\nabla^2\phi}_{=0} - 2\frac{\partial^2\phi}{\partial x_3^2} + 2Ax_3 + B\right)\\
&\quad +\frac{1}{G}\frac{\partial G}{\partial x_3}\underbrace{\left(\frac{\partial^2\phi}{\partial x_3\partial x_i} - \frac{\partial^2\phi}{\partial x_i\partial x_3}\right)}_{=0}\\
&\quad = 2\frac{1+\nu}{1-2\nu}\left(-\frac{1}{1+\nu}\frac{\partial^3\phi}{\partial x_i\partial x_3^2}\right) - \frac{\partial}{\partial x_3}\underbrace{(\nabla^2\phi)}_{=0} + 2A\\
&\quad +\frac{1}{1-2\nu}\frac{\partial}{\partial x_3}\left(\underbrace{\nabla^2\phi}_{=0} - 2\frac{\partial^2\phi}{\partial x_3^2} + 2Ax_3 + B\right)\\
&\quad +\frac{2}{G}\frac{\partial G}{\partial x_3}\left[-\frac{\partial^2\phi}{\partial x_3^2} + 2Ax_3 + B + \frac{\nu}{1-2\nu}\left(\underbrace{\nabla^2\phi}_{=0} - 2\frac{\partial^2\phi}{\partial x_3^2}\right.\right.\\
&\left.\left.+2Ax_3 + B)\right] = 2\frac{1+\nu}{1-2\nu}\left[2\frac{1-\nu}{1+\nu}A - \frac{1}{1+\nu}\frac{\partial^3\phi}{\partial x_3^3}\right.\right.\\
&\left.\left.+\frac{1}{E}\frac{\partial E}{\partial x_3}\left(2\frac{1-\nu}{1+\nu}Ax_3 - \frac{1}{1+\nu}\frac{\partial^2\phi}{\partial x_3^2}\right)\right].
\end{aligned} \tag{8}$$

The stress components referring to the plane stress state with respect to axis x_3

$$\begin{aligned}
&\tau_{13} = G\left(\frac{\partial u_1}{\partial x_3} + \frac{\partial u_3}{\partial x_1}\right) = G\underbrace{\left(\frac{\partial^2\phi}{\partial x_1\partial x_3} - \frac{\partial^2\phi}{\partial x_3\partial x_1}\right)}_{=0} = 0,\\
&\tau_{23} = G\left(\frac{\partial u_2}{\partial x_3} + \frac{\partial u_3}{\partial x_2}\right) = G\underbrace{\left(\frac{\partial^2\phi}{\partial x_2\partial x_3} - \frac{\partial^2\phi}{\partial x_3\partial x_2}\right)}_{=0} = 0,\\
&\sigma_{33} = 2G\left[\frac{\partial u_3}{\partial x_3} - \alpha\theta + \frac{\nu}{1-2\nu}(\Theta - 3\alpha\theta)\right]\\
&\quad = 2G\left\{-\frac{\partial^2\phi}{\partial x_3^2} + 2Ax_3 + B - 2\frac{1-\nu}{1+\nu}Ax_3 + \frac{1}{1+\nu}\frac{\partial^2\phi}{\partial x_3^2}\right.\\
&\quad +\frac{\nu}{1-2\nu}\left[\underbrace{\nabla^2\phi}_{=0} - 2\frac{\partial^2\phi}{\partial x_3^2} + 2Ax_3 + B\right.\\
&\left.\left.\quad -3\left(2\frac{1-\nu}{1+\nu}Ax_3 - \frac{1}{1+\nu}\frac{\partial^2\phi}{\partial x_3^2}\right)\right]\right\} = 2G\frac{1-\nu}{1-2\nu}B,
\end{aligned} \tag{9}$$

are also identically equal to zero when $B = 0$ for any point x_i. This proves that Eqs (6) transform original mechanical problem Eq. (3) into plane stress problem

$$\nabla^2\phi + 2(1-\nu)Ax_3 - (1+\nu)\alpha\theta = 0. \tag{10}$$

The general solution (10) can be written in a form which is more suitable to plate problem, namely in which the thermoelastic solid is bounded by two parallel planes $x_3 = z$ and exhibits axial symmetry

$$\frac{\partial^2\phi}{\partial r^2} + \frac{1}{r}\frac{\partial\phi}{\partial r} + 2(1-\nu)Az - (1+\nu)\alpha\theta = 0. \tag{11}$$

Differentiation of Eq. (11) with respect to r and next substitution $u = \partial\phi/\partial r$ according to Eqs (61), lead to the classical Euler-type differential equation describing thermo-mechanical membrane state

$$\frac{\partial^2 u}{\partial r^2} + \frac{1}{r}\frac{\partial u}{\partial r} - \frac{u}{r^2} = (1+\nu)\frac{\partial(\alpha\theta)}{\partial r}. \tag{12}$$

Unique solution of equation (12) that satisfies homogeneous boundary conditions

$$u(0) = 0, \quad \sigma_r(R) = 0 \tag{13}$$

takes well known form

$$u = \frac{(1-\nu)}{R^2}r\int_0^R \alpha\theta r\mathrm{d}r + \frac{(1+\nu)}{r}\int_0^r \alpha\theta\rho\mathrm{d}\rho,$$

DOI 10.1515/ama-2015-0022

$$\sigma_r = \frac{E}{R^2}\int_0^R \alpha\theta r\mathrm{d}r - \frac{E}{r^2}\int_0^r \alpha\theta\rho\mathrm{d}\rho, \qquad (14)$$
$$\sigma_\varphi = \frac{E}{R^2}\int_0^R \alpha\theta r\mathrm{d}r + \frac{E}{r^2}\int_0^r \alpha\theta\rho\mathrm{d}\rho - E\alpha\theta,$$

which in case of constant temperature $\theta = \mathrm{const}$ and linear gradation of coefficient of thermal expansion $\alpha(z) = a_0 + a_1 z$ leads to purely linear (stress-less) deformation

$$u(r,z) = \alpha\theta(z)r, \quad \sigma_r = \sigma_\varphi \equiv 0, \qquad (15)$$

what closes the proof.

4.2. Proof based on stress formulation

The proof of theorem presented in point 4.1, in case of the stress formulation Eq. ($5_{1\text{-}3}$), is straightforward analogy to those done by Fung (1965) and Nowacki (1970) for homogenous material. This turns out to be almost elementary when one assumes that $\sigma_{ij} \equiv 0$ in both Eq. ($5_{1\text{-}3}$) and appropriate boundary conditions. Namely, system of equations is satisfied as identity if

$$\frac{\partial^2(\alpha\theta)}{\partial x_i^2} - \nabla^2(\alpha\theta) = 0 \qquad i = 1,2,3,$$
$$\frac{\partial^2(\alpha\theta)}{\partial x_i x_j} = 0 \qquad i,j = 1,2,3, \qquad (16)$$
$$\nabla^2\theta + \frac{1}{\lambda}\frac{\partial\lambda}{\partial x_3}\frac{\partial\theta}{\partial x_3} = 0.$$

For constant temperature $\theta = \mathrm{const}$ satisfying Fourier's law (16_3) the unique solution of ($16_{1,2}$) corresponds again to the linear gradation of coefficient of thermal expansion $\alpha(x_3) = a_0 + a_1 x_3$.

5. EXAMPLE

It has been proved in points 4.1 and 4.2 that material of linear gradation of thermal expansion coefficient, subjected to constant temperature exclusively, is not stressed. This means that it exhibits unconstrained and purely thermal deformation. In case of axial symmetry such deformation can be expressed by following equations

$$\varepsilon_r = \frac{\partial u}{\partial r} = \alpha\theta, \quad \varepsilon_\varphi = \frac{u}{r} = \alpha\theta, \quad \varepsilon_z = \frac{\partial w}{\partial z} = \alpha\theta. \qquad (17)$$

Let us assume that the structure is composed of homogeneous metallic substrate (Al) and ceramic layer (Al_2O_3), joined by FGM interface as shown in Fig.3, and thermo-elastic properties presented in Tab.1.

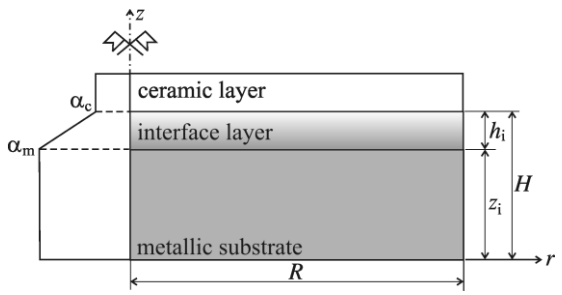

Fig. 3. Metallic substrate and ceramic layer joined by FGM interface of linear thermal expansion coefficient structure

Hence linearly graded coefficient of thermal expansion exhibits polygonal function

$$\alpha(z) = \begin{cases} \alpha_\mathrm{m} & 0 \le z < z_\mathrm{i} \\ \alpha_\mathrm{m} - (\alpha_\mathrm{m} - \alpha_\mathrm{c})\frac{z - z_\mathrm{i}}{h_\mathrm{i}} & z_\mathrm{i} \le z < z_\mathrm{i} + h_\mathrm{i} \\ \alpha_\mathrm{c} & z_\mathrm{i} + h_\mathrm{i} \le z \le H \end{cases} \qquad (18)$$

and we easily arrive at following of solution Eqs (18) for u

$$u(r,z) = \int_0^r \alpha(z)\theta\mathrm{d}\rho = \begin{cases} \alpha_\mathrm{m}\theta r & 0 \le z < z_\mathrm{i} \\ \alpha_\mathrm{m}\theta r - (\alpha_\mathrm{m} - \alpha_\mathrm{c})\frac{z - z_\mathrm{i}}{h_\mathrm{i}}\theta r & z_\mathrm{i} \le z < z_\mathrm{i} + h_\mathrm{i} \\ \alpha_\mathrm{c}\theta r & z_\mathrm{i} + h_\mathrm{i} \le z \le H \end{cases} \qquad (19)$$

and for w respectively

$$w(r,z) = \int_0^z \alpha(z)\theta\mathrm{d}\zeta = \begin{cases} \alpha_\mathrm{m}\theta z & 0 \le z < z_\mathrm{i} \\ \alpha_\mathrm{m}\theta z - (\alpha_\mathrm{m} - \alpha_\mathrm{c})\frac{(z - z_\mathrm{i})^2}{2h_\mathrm{i}}\theta & z_\mathrm{i} \le z < z_\mathrm{i} + h_\mathrm{i} \\ \alpha_\mathrm{c}\theta(z_\mathrm{i} + h_\mathrm{i}) - (\alpha_\mathrm{m} - \alpha_\mathrm{c})\frac{h_\mathrm{i}}{2}\theta + \alpha_\mathrm{c}\theta(z - z_\mathrm{i} + h_\mathrm{i}) & z_\mathrm{i} + h_\mathrm{i} \le z \le H \end{cases}. \qquad (20)$$

The displacement field corresponding to stress free deformation defined by Eqs (19-20) is spanned over the mesh of 81×41 square elements and shown in Fig. 4. It is well visible that both substrate and ceramic layers exhibit homogeneous deformation, whereas deformation of interface links them satisfying simultaneously stress less state.

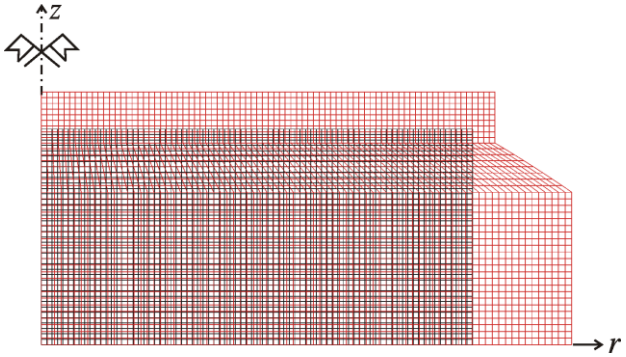

Fig. 4. Unconstrained (stress less) and purely thermal deformation Eqs (19-20) of three layer structure: initial mesh – black colour, deformed mesh – red colour (displacement magnified ×100)

6. CONCLUSIONS

Homogeneous temperature field does not result stress in thermo-elastic material of linear gradation, if only force type boundary conditions are homogeneous and there are not body forces. However, the case of stress less deformation has only theoretical sense since neither manufacturing nor classical FEM do not allow for modeling of continuously varying FGM. Namely, from technological point of view the Al_2O_3 outer layer deposed on top of a NiCoCAlY bond coat, shown in Fig. 1 after Schulz et al. (2003), exhibits hardly noticeable stress state resulting from mismatch between metal and ceramic Young's modules and coefficients of thermal expansion. On the other hand, if the classical FEM is used for solving FGM problems, the material properties can only vary in a piecewise continuous manner since all integra-

tion points within an element have a common property value. To overcome this difficulty a special graded element concept, based on additional interpolation for nodal material properties, is necessary to apply.

REFERENCES

1. **Akai T., Ootao Y., Tanigawa Y.** (2005), Piezothermoelastic analysis of functionally graded piezoelectric cylindrical panel due to nonuniform heat supply in the circumefernetial direction, *Proc. Thermal Stresses'05*, 709-712.
2. **Bagri A., Eslami M. R., Samsam-Shariat B. A.** (2005), Coupled thermoelasticity of functionally graded layer, *Proc. Thermal Stresses'05*, 721-724.
3. **Chen W. F., Tong L.** (2004), Sensitivity analysis of heat conduction for functionally graded materials, *Mater. Design*, 25, 633-672.
4. **Cho J. R., Shin S. W.** (2004), Material composition optimization for heat-resisting FGMs by artificial neural network, *Composites*, A35, 585-595.
5. **Fung Y. C.** (1965), *Foundations of solid mechanics*, Prentice-Hall, New Jersey.
6. **Ganczarski A., Barwacz L.** (2004), Notes on damage effect tensors of two-scalar variables, *Int. J. Damage Mech.*, 13, 3, 287-295.
7. **Ignaczak J.** (1959), Direct determination of stresses from the stress equations of motion in elasticity, *Arch. Mech. Stos.*, 11(5), 671−678.
8. **Iljushin A. A., Lomakin W. A., Shmakov A. P.** (1979), *Mechanics of Continuous Media*, Moscow.
9. **Kim J. H., Paulino G. H.** (2002), Isoparametric graded finite elements for non-homogeneous isotropic and orthotropic materials, *ASME J. Appl. Mech.*, 69, 502−514.
10. **Lee W. Y., Stinton D. P., Berndt C. C, Erdogan F., Lee Y.-D., Mutasin Z.** (1996), Concept of functionally graded materials for advanced thermal barrier coating applications, *J. Am. Ceram. Soc.* 79, 3003-3012.
11. **Muki R.** (1957), Thermal stresses in a semi-infinite solid and a thick plate under steady distribution of temperature, *Proc. Fac. Eng. Keio. Univ.*, 9, 42.
12. **Noda N.** (1999), Thermal stresses in functionally graded materials, *J. Thermal Stresses*, Vol. 22(4/5), 477−512.
13. **Nowacki W.** (1970), *Theory of elasticity*, PWN, Warsaw.
14. **Odqvist F. K. G.** (1966), *Mathematical theory of creep and creep rupture*, Oxford, Clarendon Press.
15. **Potarescu F., Sugano Y.** (1993), An improved solution to thermoelastic material design in fuctionally graded materials: Scheme to reduce thermal stresses, *Comput. Mech. Appl. Mech.Eng.*, 109, 377-389.
16. **Schulz U., Bach F. W., Tegeder G.** (2003), Graded coating for thermal, wear and corrosion barriers, *Mater. Sci. Eng.*, A 362(1-2), 61−80.
17. **Sneddon I. N., Lockett F. J.** (1960), On the steady-state thermo-elastic problem for the half-space and the thick plate, *Quart. Appl. Math.*, Vol. 18(2), 145−153.
18. **Sternberg E., McDowell E. L.** (1957), On the steady-state thermoelastic problem for the half-space, *Quart. Appl. Math.*, 14, 381.
19. **Wang B.-L., Han J. C., Du S. Y.** (2000), Crack problems for functionally graded materials under transient thermal loading, *J. Thermal Stresses*, 23, 143-168.
20. **Yamanouchi M., Hirai T., Shiota I.** (1990), Overall view of the P/M fabrication of fuctionally gradient materials, *Proc. First Int. Symp. Functionally Gradient Materials*, eds Yamanouchi et al., Sendai, Japan, 59-64.

This work was supported by National Science Centre Poland grant Nr UMO-2011/03/B/ST8/05132.

DOI 10.1515/ama-2015-0023

STRESS STATE OF PLATE WITH INCISIONS UNDER THE ACTION OF OSCILLATING CONCENTRATED FORCES

Vasyl' SHVABYUK[*], Heorhiy SULYM[**], Olena MIKULICH[*]

*Department of Technical Mechanic, Lutsk National Technical University, 75 Lvivska st., Lutsk, 43018, Ukraine
**Bialystok University of Technology, ul. Wiejska 45C, 15-351 Bialystok, Poland

shvabyk@lutsk-ntu.com.ua, h.sulym@pb.edu.pl, shypra@ukr.net

received 2 March 2015, revised 9 October 2015, accepted 14 October 2015

Abstract: This paper proposes the novel technique for analysis of dynamic stress state of multi-connected infinite plates under the action of oscillating forces. Calculation of dynamic stresses at the incisions of plates is held using the boundary-integral equation method and the theory of complex variable functions. The numerical implementation of the developed algorithmis based on the method of mechanical quadratures and collocation technique. The algorithm is effective in the analysis of the stress state caused by steady-state vibrations of plates.

Key words: Stress State, Plates, Incision, Hole

1. INTRODUCTION

Many structural elements, which are used in modern engineering, can be modelled as plates during the structural analysis. Frequently these elements operate under the dynamic loads. Thus, estimation of their strength is based on the calculation of dynamic stress state near defects, which can be present in the plate. This greatly complicates the stress state due to the reflection of elastic waves from the defects' boundary inside the plate.

In contrast with static loading, the strength of structural elements depends on the frequency of the applied dynamic load.

Methods for analysis of the stress state of structural elements with one or more holes under dynamic loadings were developed in the works: Brebbia et al. (1984), Guz et al. (1978), Savin (1968), Timoshenko (1967), Pao and Mow (1971), Mow and Mente (1963), etc.

The problem of diffraction of elastic waves in an infinite plate with a circular hole or a system circular holes was solved by Guz et al. (1978), Pao et al. (1971) and Mow et al. (1963). In the works by Kubenko (1967) and Guz et al. (1978) the problem of the concentration of dynamic stress near holes of non-canonical form is studied by the method, which is based on the method of series and the boundary shape perturbation technique.

In the works Mushelishvili (1966) and Panasyuk et al. (1984) an algorithm for studying of the stress state of plates of different shape under the static loadings is developed. This algorithm is based on the boundary integral equation method and the theory of a complex variable.

The main advantage of this approach is its universality and high accuracy in the case of multiply connected plates of difficult shape or infinite plates with holes, which are under the action of concentrated forces.

Systems of integral equations for determination of the dynamic stress state of plates are derived in the works: Kupradze (1963), Sherman (1962), Sladek et al. (2000). Numerical analysis of the stress state is held by the boundary element method in the works Benerjee (1994) and Brebbia et al. (1984). The Somigliana type integral formula is used. Thus, integral equations for relative displacements are directly obtained. Stress at the boundary is determined by the numerical differentiation. At high frequencies, numerical differentiation can lead to significant errors, thus, the technique which utilize stress integral formulae for dynamic problems is of high importance.

2. SOLUTION OF THE PROBLEM

2.1. Statement of the problem

Consider an infinite plate with incision that is under the influence of concentrated oscillating forces $Q_1 e^{i\omega\tau}$, $Q_2 e^{i\omega\tau}$, where ω is the frequency of the applied loading, and τ is time (Fig. 1). The problem consists in determination of the dynamic stresses at the boundary incision in the plate.

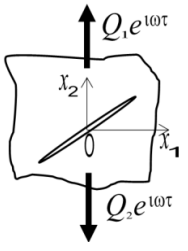

Fig. 1. Model of the plate

The center of gravity of the plate is placed at the origin of a Cartesian coordinate system Ox_1x_2. Symbol D denotes the

domain occupied by the plate, and L is the boundary of the domain D.

2.2. Integral equation of the problem

For the plane stress state the potential solution for image motion is selected as (Bonnet, 1995):

$$u_j = \int_L p_i U_{ij}^* ds + \int_D Q_i U_{ij}^* dD, \quad (1)$$

where $p_1,\ p_2$ are unknown complex potential function.

The representation of the image U_{ij}^* should be choosing with the regard to Zommerfeld conditions, since the plate is infinite. It has the form (Brebbia et al., 1984):

$$U_{ij}^* = \frac{1}{2\pi\rho c_2^2}\left(\psi\delta_{ij} - \chi \cdot r_i r_j\right),$$

where

$$\psi = \frac{i\pi}{2}\left(-H_0^2\left(\frac{\omega r}{c_2}\right) + \frac{c_2}{\omega r}\left(H_1^2\left(\frac{\omega r}{c_2}\right) - \frac{c_2}{c_1}H_1^2\left(\frac{\omega r}{c_1}\right)\right)\right),$$

$$\chi = \frac{i\pi}{2}\left(H_2^2\left(\frac{\omega r}{c_2}\right) - \left(\frac{c_2}{c_1}\right)^2 H_2^2\left(\frac{\omega r}{c_1}\right)\right),$$

$r_i = \frac{\partial r}{\partial x_i}$, $r = \sqrt{(x_1 - x_1^0)^2 + (x_2 - x_2^0)^2}$, c_1, c_2 are the speeds of expansion and shear waves: $c_1^2 = \frac{E}{\rho(1-\nu^2)}, c_2^2 = \frac{E}{2\rho(1+\nu)}$, E is the Young's modulus, ρ is the density of the material; ν is the Poisson ratio; $H_k^2(r) = J_k(r) - Y_k(r)$ are Hankel functions of the second kind; $J_k(r),\ Y_k(r)$ are Bessel functions of the first and second kinds $(i, j = 1, 2)$. The integration over the domain and along the boundary is performed within variable x_1^0, x_2^0. Here the time factor $e^{i\omega\tau}$ is omitted at the displacements and the stresses terms.

Determination of the stresses at an arbitrary point of the plate with normal $\vec{n}$ are performed by the formula (Savin, 1968):

$$2(\sigma_n - i\,\tau_n) = \frac{2E}{1-\nu} Re\left(\frac{\partial}{\partial\bar{z}}(u_1 - iu_2)\right) + e^{2i\alpha}\frac{2E}{1+\nu}\left(\frac{\partial}{\partial z}(u_1 - iu_2)\right), \quad (2)$$

where α is the angle between the normal to the boundary of the plate and the axis Ox_1; $\frac{\partial}{\partial\bar{z}} = \frac{1}{2}\left(\left(\frac{\partial}{\partial x_1} - i\frac{\partial}{\partial x_2}\right)\right)$, $\frac{\partial}{\partial z} = \frac{1}{2}\left(\left(\frac{\partial}{\partial x_1} + i\frac{\partial}{\partial x_2}\right)\right)$.

Since the functions U_{ij}^* along with the displacement u_j are complex, the determination of the stress is performed for the real and imaginary parts of images (1):

$$u_j^R = \int_L \left(p_i^R U_{ij}^{*R} - p_i^I U_{ij}^{*I}\right)ds + \int_D \left(Q_i^R U_{ij}^{*R} - Q_i^I U_{ij}^{*I}\right)dD,$$

$$u_j^I = \int_L \left(p_i^I U_{ij}^{*R} + p_i^R U_{ij}^{*I}\right)ds + \int_D \left(Q_i^I U_{ij}^{*R} + Q_i^R U_{ij}^{*I}\right)dD,$$

where the values with the superscript R are real parts of corresponding functions $F_k^R = Re(F_k)$, and the values with the superscript I are the imaginary parts of corresponding functions $F_k^I = Im(F_k), k = 1,2$.

Substituting the representation for displacement in the formula (2), we obtain formulas for determining stresses at the boundary of the plate:

$$2(\sigma_n^R - i\,\tau_{sn}^R) = \int_L (f_1^R q^R - f_1^I q^I)dt + \int_L (f_2^R \bar{q}^R - f_2^I \bar{q}^I)d\bar{t}$$
$$\int_D (f_1^R Q^R - f_1^I Q^I)dD + \int_L (f_2^R \bar{Q}^R - f_2^I \bar{Q}^I)dD$$

$$2(\sigma_n^I - i\,\tau_{sn}^I) = \int_L (f_1^R q^I + f_1^I q^R)dt + \int_L (f_2^R \bar{q}^I + f_2^I \bar{q}^R)d\bar{t}$$
$$+ \int_D (f_1^R Q^I + f_1^I Q^R)dD + \int_L (f_2^R \bar{Q}^I + f_2^I \bar{Q}^R)dD,$$

where $f_k^R = f_k^R(x_1,\ x_2,\ x_1^0,\ x_2^0), f_k^I = f_k^I(x_1,\ x_2,\ x_1^0,\ x_2^0)$, $k = 1, 2$ are functions of the real argument, which contain Bessel functions of second and first kind respectively and are obtained similarly to those in Mikulich and Maksymovych (2011); $q^R = \frac{ip^R ds}{dt}, q^I = \frac{ip^I ds}{dt}$ are unknown functions to be determined, $t = x_1^0 + ix_2^0$.

Integration of functions $f_k^R, k = 1,2$ for small values of the argument leads to singularity. To establish their characteristics we use the asymptotic expressions for the Bessel functions of the second kind for small values of the argument (Elbert and Laforgia, 1986). Then the formula for determining of the stresses can be written as:

$$2(\sigma_n^R - i\,\tau_{sn}^R) = \frac{1}{2\pi i}\frac{1+\nu}{2}\int_L \left(\left(\frac{dz}{d\bar{z}}\frac{\bar{z}-\bar{t}}{z-t} - 1\right)\frac{1}{z-t}\right)q^R dt$$
$$-\frac{1}{2\pi i}\int_L \left(-\frac{1+\nu}{2}\frac{1}{\bar{z}-\bar{t}} + \frac{dz}{d\bar{z}}\frac{3-\nu}{2}\frac{1}{z-t}\right)\bar{q}^R d\bar{t} +$$
$$\int_L (G_1^R q^R - f_1^I q^I)dt + \int_L (G_2^R \bar{q}^R - f_2^I \bar{q}^I)d\bar{t} +$$
$$\int_D (f_1^R Q^R - f_1^I Q^I)dD + \int_D (f_2^R \bar{Q}^R - f_2^I \bar{Q}^I)dD;$$

$$2(\sigma_n^I - i\,\tau_{sn}^I) = \frac{1}{2\pi i}\frac{1+\nu}{2}\int_L \left(\left(\frac{dz}{d\bar{z}}\frac{\bar{z}-\bar{t}}{z-t} - 1\right)\frac{1}{z-t}\right)q^I dt$$
$$-\frac{1}{2\pi i}\int_L \left(-\frac{1+\nu}{2}\frac{1}{\bar{z}-\bar{t}} + \frac{dz}{d\bar{z}}\frac{3-\nu}{2}\frac{1}{z-t}\right)\bar{q}^I d\bar{t} +$$
$$\int_L (G_1^R q^I + f_1^I q^R)dt + \int_L (G_2^R \bar{q}^I + f_2^I \bar{q}^R)d\bar{t} +$$
$$\int_D (f_1^R Q^I + f_1^I Q^R)dD + \int_D (f_2^R \bar{Q}^I + f_2^I \bar{Q}^R)dD;$$

where $f_k^I,\ G_k^R = G_k^R(x_1,\ x_2,\ x_1^0,\ x_2^0),\ k = 1,2$ are bounded and continuous functions of real argument everywhere in *D*.

Let us perform the limiting transition when $(x_1, x_2) \to L$ in the last formula according to Plemelj-Sokhotski formulas (Savin, 1968). Consequently, integral equations for determination of the unknown functions q^R and q^I for given loading at the boundary are obtain:

$$\bar{q}^R + \frac{1}{2\pi i}\frac{1+\nu}{2}\int_L \left(\left(\frac{dz}{d\bar{z}}\frac{\bar{z}-\bar{t}}{z-t} - 1\right)\frac{1}{z-t}\right)q^R dt$$
$$-\frac{1}{2\pi i}\int_L \left(-\frac{1+\nu}{2}\frac{1}{\bar{z}-\bar{t}} + \frac{dz}{d\bar{z}}\frac{3-\nu}{2}\frac{1}{z-t}\right)\bar{q}^R d\bar{t} + \quad (3)$$
$$\int_L (G_1^R q^R - f_1^I q^I)dt + \int_L (G_2^R \bar{q}^R - f_2^I \bar{q}^I)d\bar{t} = 2S^R;$$

$$\bar{q}^I + \frac{1}{2\pi i}\frac{1+\nu}{2}\int_L \left(\left(\frac{dz}{d\bar{z}}\frac{\bar{z}-\bar{t}}{z-t} - 1\right)\frac{1}{z-t}\right)q^I dt$$
$$-\frac{1}{2\pi i}\int_L \left(-\frac{1+\nu}{2}\frac{1}{\bar{z}-\bar{t}} + \frac{dz}{d\bar{z}}\frac{3-\nu}{2}\frac{1}{z-t}\right)\bar{q}^I d\bar{t} + \quad (4)$$
$$\int_L (G_1^R q^I + f_1^I q^R)dt + \int_L (G_2^R \bar{q}^I + f_2^I \bar{q}^R)d\bar{t} = 2S^I,$$

where the first and second integrals are evaluated for their Cauchy principal value; S^R, S^I are known function:

$$2S^R = \int_D (f_1^I Q^I - f_1^R Q^R)dD + \int_D (f_2^I \bar{Q}^I - f_2^R \bar{Q}^R)dD,$$
$$2S^I = \int_D (f_1^R Q^I + f_1^I Q^R)dD + \int_D (f_2^R \bar{Q}^I + f_2^I \bar{Q}^R)dD.$$

Stresses at the boundary of the incisions of the plate are determined in the absence of the contact of the incision's boundary. This is verified by the formulas:

DOI 10.1515/ama-2015-0023

$$u_1^R - iu_2^R = -\frac{1+\nu}{\pi Ei}\int_L (F_1^R q^R - F_1^I q^I)dt + \int_L (F_2^R \bar{q}^R - F_2^I \bar{q}^I)d\bar{t} + \int_D (F_1^R Q^R - F_1^I Q^I)dD + \int_L (f_2^R \bar{Q}^R - F_2^I \bar{Q}^I)dD, \quad (5)$$

$$u_1^I - iu_2^I = -\frac{1+\nu}{\pi Ei}\int_L (F_1^R q^I + F_1^I q^R)dt + \int_L (F_2^R \bar{q}^I + F_2^I \bar{q}^R)d\bar{t} + \int_D (F_1^R Q^I + F_1^I Q^R)dD + \int_L (f_2^R \bar{Q}^I + F_2^I \bar{Q}^R)dD, \quad (6)$$

where $F_k^R = F_k^R(x_1,\ x_2,\ x_1^0,\ x_2^0), F_k^I = F_k^I(x_1,\ x_2,\ x_1^0,\ x_2^0)$, $k = 1, 2$ are functions of the real argument, which contain Bessel functions of second and first kind respectively and are obtained similar to those by Mikulich (2012).

2.3. Numeric solution of the algortim

To study the stress state of the infinite plate with one incision denote its boundary contour as Ω. The incision in the plates is modeled as an elliptic hole with axis ratio of 10. Its equation in parametric form is as follows: $x_1 = \varphi(\theta),\ x_2 = \psi(\theta),\ 0 < \theta < 2\pi$. Parameter θ is chooses with respect to the condition that traversing the path boundary region remains at the left. To reduce the number of nodal points the numerical integration is performed using Sidi sigmoidal non-linear transformation (Sidi, 2006):

$$\theta = G(\xi) = \xi - \frac{\sin(2\pi\xi)}{2\pi}, 0 < \xi < 2\pi.$$

Then, at the boundary it holds that $t = \varphi(\theta) + i \cdot \psi(\theta) = g(\theta)$.

Solution of integral equations (3) - (4) is performed using the method of mechanical quadratures. For integrals with Cauchy-type kernels quadrature formulas of the form (Kolm and Rokhlin, 2001; Eshkuvatov et al., 2009) are used:

$$\int_\Omega \frac{q}{t-z_\nu}dt = h\sum_{n=1}^K q_n \frac{g'_n}{t_n - z_\nu},$$
$$t_n = g(\theta_n),\ g'_n = g'(\theta_n),\ \theta_n = n \cdot h,\ z_\nu = z(\tilde{\theta}_\nu),$$
$$\tilde{\theta}_\nu = \theta_\nu + \frac{h}{2},\ \nu = \overline{1,K},\ q_n = q(t_n),\ h = \frac{2\pi}{K}.$$

And for other of the integrals the quadrature formulas of the form (Mikulich, 2012) are applied:

$$\int_\Omega q \cdot f(t,\ z_\nu)dt = h\sum_{n=1}^K q_n \cdot f_{\nu n} \cdot g'_n,$$

where $f_{\nu n} = f(t_n, z_\nu)$.

Replacing the integrals with the specified quadrature formulas, the system of linear algebraic equations for determination of the nodal values of unknown boundary functions q^R and q^I is obtained:

$$\bar{q}_\nu^R + h\sum_{n=1}^K f_{1\nu n}^R q_n^R g'_n + h\sum_{n=1}^K f_{2\nu n}^R \bar{q}_n^R \bar{g}'_n - h\sum_{n=1}^K f_{1\nu n}^I q_n^I g'_n - h\sum_{n=1}^K f_{2\nu n}^I \bar{q}_n^I \bar{g}'_n = 2S_\nu^R,$$

$$\bar{q}_\nu^I + h\sum_{n=1}^K f_{1\nu n}^R q_n^I g'_n + h\sum_{n=1}^K f_{2\nu n}^R \bar{q}_n^I \bar{g}'_n + h\sum_{n=1}^K f_{1\nu n}^I q_n^R g'_n + h\sum_{n=1}^K f_{2\nu n}^I \bar{q}_n^R \bar{g}'_n = 2S_\nu^I,$$

where $\bar{q}_\nu^R = \bar{q}^R(z_\nu),\ q_n^R = q^R(t_n),\ \bar{q}_\nu^I = \bar{q}^I(z_\nu)$, are real and imaginary parts of the unknown functions at the boundary, $f_{i\nu n}^R = f_i^R(t_n,\ z_\nu),\ f_{i\nu n}^I = f_i^I(t_n,\ z_\nu),\ i = 1, 2,\ S_\nu^R = S^R(z_\nu),$ $S_\nu^I = S^I(z_\nu)$ are known function.

Calculations were performed in the absence of contact of boundary of incisions that was tested on the basis of Esq. (5)-(6).

After determination of the unknown functions, stress state of the plate is calculated by dependencies, which are obtained in accordance with representation (1) by providing singular components in the kernels of equations and consequently using Plemelj-Sokhotski formulas:

$$2(\sigma_{\theta_\nu} - i\tau_{s\theta_\nu}) = 2(\sigma_{\theta_\nu}^R - i\tau_{s\theta_\nu}^R) + 2i(\sigma_{\theta_\nu}^I - i\tau_{s\theta_\nu}^I),$$

$$2(\sigma_{\theta_\nu}^R - i\tau_{s\theta_\nu}^R) = \frac{1+\nu}{2}q_\nu^R + \frac{1-\nu}{2}\bar{q}_\nu^R + h\sum_{n=1}^K \tilde{f}_{1\nu n}^R q_n^R g'_n + h\sum_{n=1}^K \tilde{f}_{2\nu n}^R \bar{q}_n^R \bar{g}'_n - h\sum_{n=1}^K \tilde{f}_{1\nu n}^I q_n^I g'_n - h\sum_{n=1}^K \tilde{f}_{2\nu n}^I \bar{q}_n^I \bar{g}'_n + \tilde{\Phi}_\nu^R,$$

$$2(\sigma_{\theta_\nu}^I - i\tau_{s\theta_\nu}^I) = \frac{1+\nu}{2}q_\nu^I + \frac{1-\nu}{2}\bar{q}_\nu^I + h\sum_{n=1}^K \tilde{f}_{1\nu n}^R q_n^I g'_n + h\sum_{n=1}^K \tilde{f}_{2\nu n}^R \bar{q}_n^I \bar{g}'_n + h\sum_{n=1}^K \tilde{f}_{1\nu n}^I q_n^R g'_n + h\sum_{n=1}^K \tilde{f}_{2\nu n}^I \bar{q}_n^R \bar{g}'_n + \tilde{\Phi}_\nu^I,$$

where $\tilde{f}_{i\nu n}^R = \tilde{f}_i^R(t_n,\ z_\nu),\ \tilde{f}_{i\nu n}^I = \tilde{f}_i^I(t_n,\ z_\nu);\ \ i = 1, 2;\ \ \tilde{\Phi}_\nu^R,$ $\tilde{\Phi}_\nu^I$ are the values of known functions in selected points of collocation, which are obtained similar to Mikulich and Maksymovych (2011).

2.4. Numeric calculation stresses in the plate

Based on the developed technique the distribution of maximal stresses in the plate with an incision under the actions of oscillating forces $Q_1 e^{i\omega\tau},\ Q_2 e^{i\omega\tau}$ is studied. The forces are applied at the points $(0;\ \pm b)$.

The results of calculations of dynamic stresses are attributed to the intensity of the stresses oscillating forces.

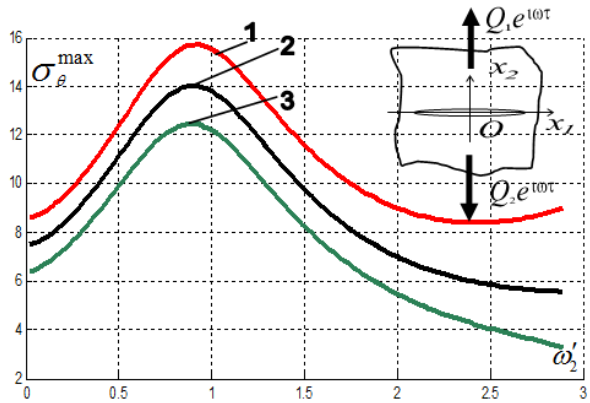

Fig. 2. Maximum dynamic stresses in the plate with a horizontal incision

Fig. 2 shows the results of numerical calculation of the dependence of the maximum dynamic stresses on the dimensionless frequency $\omega_2' = \frac{\omega \cdot a}{c_2}$ of the applied forces, where c_2 is the speed of shear waves. The incision in the plate is modeled as an elliptic hole with axis ratio of 10. Calculations were performed for different values of the distance between the point of application of

the oscillating forces and the center of the incision. The calculations were performed for 200 nodal points at the boundary of the incision. The Poisson's ratio was equal to 0.3. In Fig. 2 curve 1 corresponds to the case of $b = a$; curve 2 corresponds to the case of $b = 1.5a$ and curve 3 corresponds to the case of $b = 2a$, where a is a major semi axis of the incision.

Fig. 2 shows that the maximum dynamic stresses have the fluctuating nature. At high frequencies, a significant increase in the stresses doesn't occur due to the absence of contact at the boundary of incision.

Analysis of the numerical results shows that the maximum stresses at the boundary of the incision are increasing (for a range of frequencies in (0.01, 0.9)), and then they decrease and become lower comparing to those under static loads.

The maximum dynamic stresses exceed the corresponding static ones in 1.82 times for the case, when the distance to the points of application of forces is equal to the major semi-axis of the incision. With the increase in distance to the point of application of forces the maximum dynamic stresses exceed static in 1.86 times for $b = 1.5a$ and in 1.93 times for $b = 2a$.

Values of dynamic stresses at the boundary of incision at specific values of the frequency for oscillating concentrated forces $Q_1 e^{i\omega\tau}$, $Q_2 e^{i\omega\tau}$, which are applied at the points $(0, a)$ and $(0, -a)$ and Poisson ratio of 0.3 are determined. The results are shown in Fig. 3. Here θ is the angle in radians.

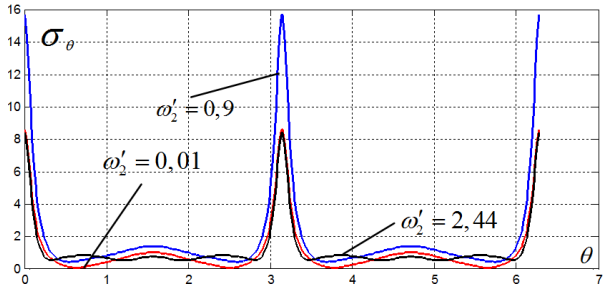

Fig. 3. Distributions of stresses on the boundary of the horizontal incision

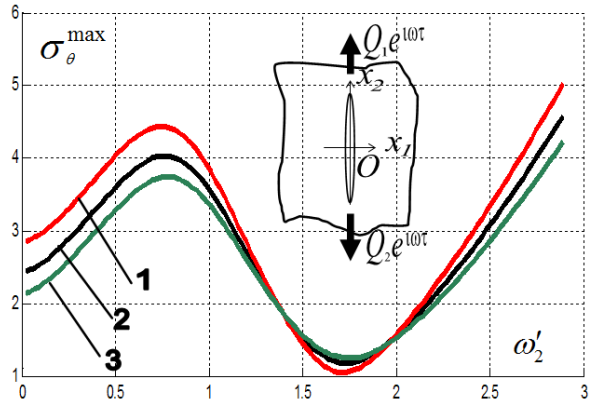

Fig. 4. Maximum dynamic stresses in the plate with a vertical incision

The figure shows that the maximum stresses are occurring at the end of the major semi-axis. There is no significant change in the distribution of stresses along the boundary of incision with increasing in frequency.

The effect of orientation of incision on the distribution of maximum dynamic stresses is also studied. The values of the maximum stresses in the plate with a vertical incision for different values of dimensionless frequency $\omega_2' = \frac{\omega \cdot a}{c_2}$ are calculated. The results are shown in Fig. 4.

Calculations were performed for different values of the distance from the point of application of the oscillating forces to the center of the incision. In numerical calculations 250 nodal points meshed the boundary of the incision, and the Poisson ratio was equal to 0.3. In Fig. 4 curve 1 corresponds to the case of $b = 1.8a$; curve 2 corresponds to the case of $b = 2a$ curve 3 corresponds to the case of $b = 2.2a$, where a is the major semi-axis of the incision.

Fig. 2 shows that the maximum dynamic stresses have the fluctuating nature.

The maximum stresses are observed at the frequency of 0.75, and minimum stresses occur at frequency of 1.72. Increase in the frequency of the applied oscillating force causes a significant increase in stresses, which exceed the static ones.

The maximum dynamic stresses exceed the corresponding static in 1.55 times for the case when the distance to the points of application of forces is $b = 1.8a$. With increase in distance to the point of application of forces the maximum dynamic stresses exceed static in 1.65 times for $b = 2a$ and in 1.75 times for $b = 2.2a$.

Values of dynamic stresses at the boundary of vertical incision at specific values of the frequency for oscillating concentrated forces $Q_1 e^{i\omega\tau}$, $Q_2 e^{i\omega\tau}$, which are applied at the points $(0, 1.8a)$ and $(0, -1.8a)$ and Poisson's ratio of 0.3 are determined. The results are shown in Fig.5. Here θ is the angle in radians.

The figure shows that the maximum stress occurs at the end of the major semi-axis. With increase in frequency the decrease in the oscillating nature of the distribution of stresses along the incision boundary is observed.

With increase in frequency of the applied load stress distribution along the boundary of the incision changes. Therefore, to study the dynamic stress state it is not enough to determine the value of stress just at a few points. This demonstrates the significant accuracy of the proposed algorithm as opposed to the methods of series and boundary shape perturbation. Since these methods define stresses only at specific points, but not along the boundary.

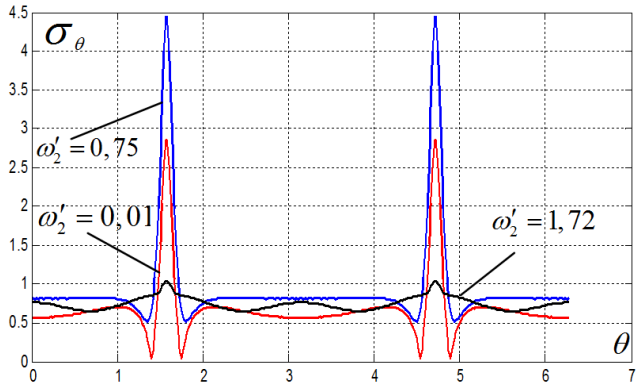

Fig. 5. Distributions of stresses on the boundary of the vertical incision

The dependence of the distribution of maximum dynamic stress from the inclination angle of the incision is investigated. Concentrated forces $Q_1 e^{i\omega\tau}$, $Q_2 e^{i\omega\tau}$ are applied at the points $(0, 2a)$ and $(0, -2a)$. The calculations were performed for 250

DOI 10.1515/ama-2015-0023

nodal points at the boundary of the incision and the Poisson's ratio of 0.3. In fig. 6 curve 1 corresponds to the case of $0°$, curve 2 — $30°$, curve 3 — $45°$, curve 4 — $60°$, curve 5 — $90°$, where is an angle between the major axis of the incision and Ox_1. axis.

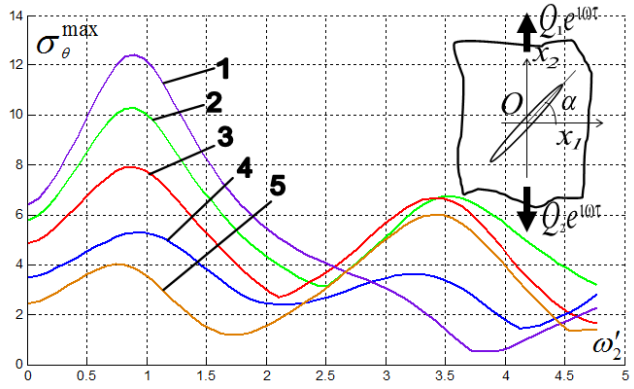

Fig. 6. Maximum dynamic stresses in the plate with an incision

Fig. 6 shows that the maximal dynamic stresses have the fluctuating nature regardless of the inclination of the incision. The maximum dynamic stresses exceed the corresponding static for the case when the frequency ω_2' of the applied load is in the range $(0.9; 1)$. For vertical incision maximum dynamic stresses occur at a frequency $\omega_2' = 3.45$.

3. SUMMARY

The technique developed in this paper allows to study the stresses at the boundary of incisions in plates under the action of concentrated oscillating forces. Effects of orientation of incisions on the stress distribution are studied. Effects of the distance between the incisions on the stress distribution are investigated.

The advantage of the proposed algorithm is the ability of determination of the dynamic stresses along the entire boundary, and not at the only specific point. This makes it possible to investigate in details the dynamic stress state of defective plates.

REFERENCES

1. **Banerjee P.** (1994) *Boundary element method in engineering science,* McGraw Hill, New York, London.
2. **Bonnet M.** (1995), *Integral equations and boundary elements. Mechanical application of solids and fluids (in French)*, CNRS Éditions / Éditions EYROLLES, Paris.
3. **Brebbia C., Telles J., Wrobel L.** (1984), *Boundary element techniques,* Springer, New York.
4. **Elbert Á., Laforgia A.** (1986), Monotonicity properties of the zeros of Bessel functions, *SIAM Journal on Mathematical Analysis,* 17, 1483-1488.
5. **Eshkuvatov Z. K., Nik Long N. M. A., Abdulkawi M.** (2009), Quadrature formula for approximating the singular integral of Cauchy type with unbounded weight function on the edges, *Journal of Computational and Applied Mathematics*, 233, 334–345.
6. **Guz A.M. Kubenko V., Chernenko M.** (1978) *The diffraction of elastic waves,* Naukova Dumka, Kyiv.
7. **Kolm P., Rokhlin V.** (2001), Numerical Quadratures for Singular and Hypersingular Integrals, *Computers and Mathematics with Applications*, 41, 327-352.
8. **Kubenko V.** (1967) Dynamic stress concentration around an elliptical hole, *Reports of the Academy of Sciences USSR*, 3, 60-64.
9. **Kupradze V.** (1963) *Methods of potential in the theory of elasticity,* Fizmatgiz, Moscow.
10. **Mikulich O. A.** (2012), Stress state of plate elements with rigid inclusion of arbitrary shape at a steady-state oscillations, *Naukovi notatky*, 39, 118-123.
11. **Mikulich O. A., Maksymovych V. M.** (2011), Study of interaction holes in infinity plates at a steady-state oscillations, *Naukovi notatky*, 33, 164-169.
12. **Mow C., Mente L.** (1963): Dynamic stresses and displacements around cylindrical discontinuities due to plane harmonic shear waves, *Journal of Applied Mechanics, 30, 598–604.*
13. **Mushelishvili N.**(1966) *Some selected problems of mathematical theory of elasticity,* Moscow.
14. **Panasyuk V., Savruk M., Nazarchuk Z.** (1984) *The method of singular integral equations in two-dimensional diffraction problems,* Naukova Dumka, Kyiv.
15. **Pao Y., Mow C.** (1971) *Diffraction of elastic waves and dynamic stress concentration*, Crane Russak, New York.
16. **Savin G. N.** (1968), *Distribution of the stresses near the holes,* Naukova Dumka, Kyiv.
17. **Sherman D.** (1962) The method of integral equations in the plane and spatial problems of static elasticity theory, *Proceedings of the All-Union Congress on Theoretical and Applied Mechanics, 405-467.*
18. **Sidi A.** (2006), Extension of a class of periodizing variable transformations for numerical integration, *Mathematics of Computation*, 75(253), 327–343.
19. **Sladek J., Sladek V., Atluri S. N.** (2000), Local boundary integral equation method for solving problem of elasticity with nonhomogeneous material properties*, Computational mechanics,* 24, 456-462.
20. **Timoshenko S.** (1967) *Fluctuations in engineering,* Nauka, Moscow.

MODELLING AND NUMERICAL ANALYSIS OF ASSEMBLY SYSTEM

Zbigniew BUDNIAK*

*Faculty of Mechanical Engineering, Koszalin University of Technology, ul. Raclawicka 15-17, 75-612 Koszalin, Poland

zbigniew.budniak@tu.koszalin.pl

received 20 October 2014, revised 7 October 2015, accepted 9 October 2015

Abstract: The present articles covers a concept of the creation and testing of assembly systems with the use of modern CAD and CAE systems on the example of an assembly system designed for joining parts with circular surfaces that are fitted with positive clearance. The numerical investigations were based on the constructed spatial skeleton pattern of the system. The purpose of the simulation tests was to determine the impact of the measurement and angular inaccuracies of all the elements of the assembly system as well as the inaccuracy of the positioning of the robot's drives on the positioning accuracy of the parts joined taking into consideration the conditions of assembly in automatic assembly.

Key words: Modeling, Analysis, Assembly Manipulator, Chain Dimensional, Assembly System, CAD/CAE

1. INTRODUCTION

Issues related to the specificity of modeling and kinematic analyses of technical systems were presented in papers Bil, (2011, 2012, 2013); Chen et al. (2014); Liuet et al. (2012), Kacalak et al. (2015). The present article covers a method to create and test assembly systems that comprise an assembly robot, a holder to fasten the body with a fitted opening, a gripper and the parts to be combined.

The essential part of the work presented included a verification of the correctness of the spatial model developed of the assembly system, development of the parametric models of the parts and the assembly, conducting a kinematic analysis (Budniak, 2012) and its visualization including its animation. SolidWorks software was used for the purpose of parametric solid modelling of the mounting seat. Kinematic calculations and analyses were conducted with the use of SolidWorks Motion software (Chang, 2011).

Special attention needs to be drawn to the possibility of conducting an analysis of the accuracy of the mutual position of the assembly system elements based on spatial dimension chains that are of a key importance in their designing. The task of the identification of dimension chains is strenuous and there is a high risk of making an error, especially in the case of mechanisms with a large number of parts with complex geometries. Owing to the use of spatial dimension chains, which are recorded as models in CAD/CAE, it is possible to conduct a verification of the conceptual spatial design of the assembly system, an analysis of the mutual positions of the elements combined in the technological process of assembly (Żurek et al., 2013; Tabara et al., 2013), an analysis of the dimensional and shape accuracy of the constituent elements of the assembly system as well as an analysis of clearances in movable connections (Storch et al., 2007; Zebrowski et al., 2009; Ahn et al., 2013).

2. CHAPTER TITLE

The process of automatic assembly could not proceed correctly without the required accuracy of the position of the parts combined at each stage (Yun et al., 2010; Zhu et al., 2013; Tabara et al., 2013). This follows particularly from the seizure conditions of the elements combined, which in the majority of cases are the conditions of automatic assembly (Budniak, 2014; Huang, 2005). The mutual position of the parts combined is particularly important in the moment of their positioning (Fig.1a) and centering (Fig.1b).

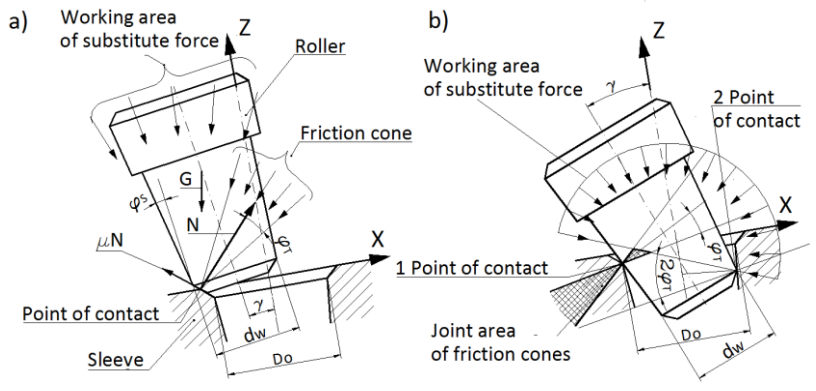

Fig. 1. The position of combined parts, where: a) positioning, b) centering

DOI 10.1515/ama-2015-0024

The first stage of the combination of the parts is characterized by a single-point contact of the elements combined. Their seizure occurs only when the direction of the substitute assembly force passes through the contact point of the parts and it is simultaneously inside the cone of friction $2\varphi T$; cf. Fig.1a. It is evident from the figure that the probability of the parts combined being seized is minute; however, it grows when angle φT is increased. The probability of the parts combined being seized during their displacement: both on the surfaces of phases and on the frontal surface of the sleeve is small.

The second stage of combining parts is substantially different from the first one, as the surfaces that are matched contact one another in two points (Fig.1b). In order to determine the seizure conditions of the parts to be combined, a mechanical engineering law was accepted, according to which: if multiple forces and moments act on an element, they can be reduced to one substitute force, while it can be found that the roller that is inserted is in standstill when the substitute assembly force cuts the common area of friction cones.

Seizure occurs when the substitute force that acts on the roller that is inserted cuts the equilibrium area that is the common area of friction cones (Fig.1b). This area is limited by a polygon, whose vertex coordinates are intersection points of the forming outline friction cones $2\varphi T$, where the value of this angle is calculated from the following formula:

$$\varphi_T = arctg\ \mu, \tag{1}$$

where: μ – friction coefficient value

At the moment of centering, the parts to be combined ought to take such a position so that with any of their dimensions that are within tolerance limits there should not occur any seizure of these. Hence, the conditions of automatic assembly are as follows:

$$\gamma \leq \gamma_{perm},\ \ \omega_\Delta \leq \omega_\Delta, \tag{2}$$

where for cylindrical parts to be combined (conical surface angle $\varphi_S = 0^0$):

$$\gamma_{perm} = \arccos\left(\frac{d_w}{D_o} * cos\varphi_T\right) - \varphi_T,$$

$$\omega_\Delta = (D_o - d_w \cdot cos\gamma_{perm})/2. \tag{3}$$

Owing to the dependences present, it is possible to reveal ways to obtained the required positional accuracy. If Condition (2) is fulfilled, everything depends from what the direction will be of the substitute assembly force. This direction will chiefly depend from the accepted assembly diagram, the constructional details of the assembly mechanisms, the rigidity of the assembly system, the misalignment of the axes of the surfaces matched etc.

3. SPATIAL MEASUREMENT CHAIN OF THE ASSEMBLY SYSTEM

In the present study, a numerical analysis was conducted of the assembly system for combining parts of the roller-sleeve type as presented in Fig. 2. This system constitutes the basis of a robotic mounting seat, which consists of an assembly robot and peripheral instrumentation. The $RRRPRR$ assembly robot possesses six degrees of freedom: five rotational couples and one sliding couple.

In order to guarantee the mutual position of the axes of the elements to be combined, points Q_s and P_h with a specific accuracy, one needs to determine above all the mutual position of the elements of the assembly system. Value r_Δ, which determines the error of the mutual position of nodal points Q_s and P_h, depends from the accuracy of the relative position of the arms of the assembly robot (r_1, r_2 and r_3), servo-motor s, gripper e with the gripping part c, the base of the robot p, the elements to be combined and the accuracy of their workmanship. The determination of the closing link r_Δ was based on the solution of the spatial measurement link (Fig. 2).

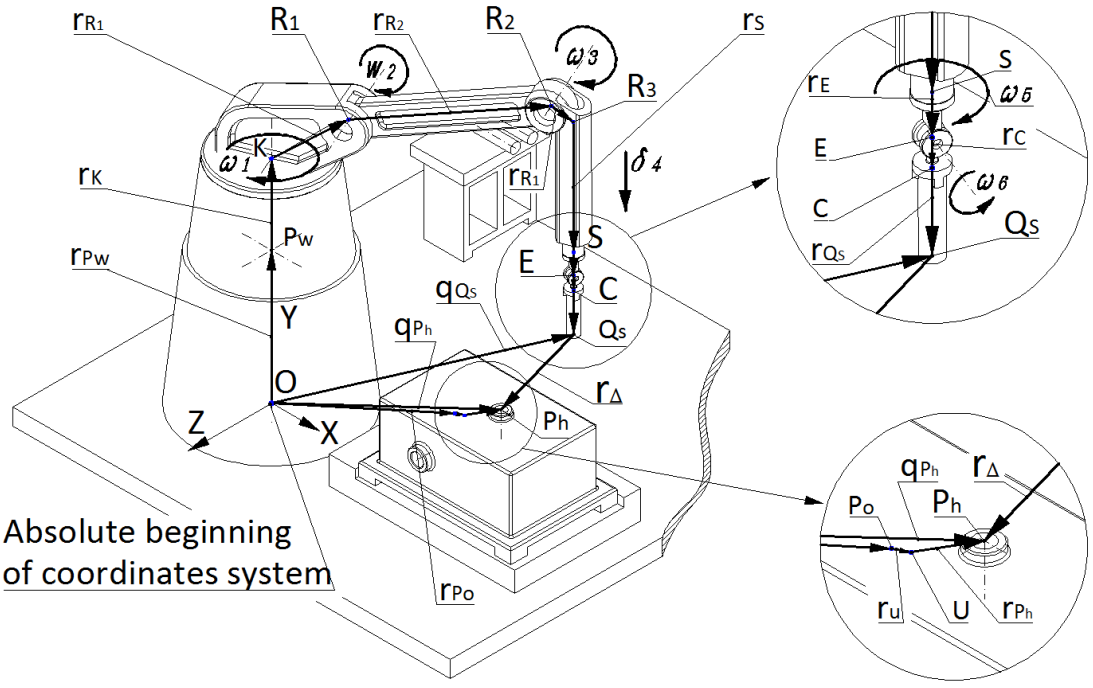

Fig. 2. Location of the assembly system components

In the general case, the value of the closing link r_Δ, the spatial measurement chain of the assembly system, is calculated from Formula (4):

$$r_\Delta = q_{Q_s} - q_{P_h} = r_{P_w} + r_{K+}r_{R_1} + r_{R_2} + r_{R_3} + r_S + r_E + r_C + r_{P_o} + r_U + r_{P_h}, \quad (4)$$

where: q_{Q_s}, q_{P_h} – vectors that determine the position of points Q_s and P_h in relation to the global system of coordinates $OXYZ$, r_{P_w}, r_{P_o}– vectors that determine the position of nodal points P_w and P_o in relation to the global system of coordinates $OXYZ$, $r_{K,}r_{R_1}, r_{R_2}, r_{R_3}, r_{S,}r_E, r_C, r_{Q_s}, r_U, r_{P_h}$ – vectors that determine the position of nodal points $K, R_1, R_2, R_3, S, E, C, Q_s, U, P_h$ that belong to the individual constituent elements of the assembly system in relation to their local systems of coordinates.

4. MODELLING OF SPATIAL MEASUREMENT CHAIN

A description of the assembly system can be considered as a description of the relative position of the local systems of coordinates related to the individual links of the measurement chain: to the reference link (base), the so-called global system $OXYZ$ is attributed (Fig. 2). Such an approach to the description of this system orders and formalizes its modeling both in the area of the kinematics and dynamics of the assembly process.

At every moment, the movable elements of the assembly system accept a specific position in relation to the base and in relation to one another. When making an analysis of the position of this system, the determination is of particular importance of the mutual position of points Q_s and P_h for the specified position of the remaining elements of the system. To the individual links of the assembly system, the following were attributed: the absolute system of coordinates $OXYZ$ related to the immovable base as well as local systems of coordinates connected with main and auxiliary assembly bases of the remaining components.

In the part of the assembly system (base p, the body of the assembly robot k, the arms of the assembly robot r_1, r_2, r_3, servo-motor s, gripper e and its gripping part c and roller w), point Q_s was selected, whose position is in the local system of coordinates $O_{B_{Q_s}}X_{B_{Q_s}}Y_{B_{Q_s}}Z_{B_{Q_s}}$ was determined as vector Q_{S_E}. In a particular case, the position of the centre of the roller with the length being equal to l_o, on its frontal surface, the following is calculated:

$$Q_{S_E} = \begin{bmatrix} 0 \\ -l_o \\ 0 \end{bmatrix}. \quad (5)$$

The same point is described with vector Q_s, which determines its position in the absolute system $OXYZ$:

$$Q_S = R_{P_w} \cdot Q_{S_{P_w}} + T_{P_w}, \quad (6)$$

where:

$$Q_{S_{P_w}} = R_K \cdot Q_{S_K} + T_K, \quad (7)$$

$$Q_{S_K} = R_{R_1} \cdot + T_{R_1}, \quad (8)$$

$$Q_{S_{R_1}} = R_{R_2} \cdot Q_{S_{R_2}} + T_{R_2}, \quad (9)$$

$$Q_{S_{R_2}} = R_{R_3} \cdot Q_{S_{R_3}} + T_{R_3}, \quad (10)$$

$$Q_{S_{R_3}} = R_S \cdot Q_{S_S} + T_S, \quad (11)$$

$$Q_{S_S} = R_E \cdot Q_{S_E} + T_E, \quad (12)$$

$$Q_{S_C} = R_C \cdot Q_{S_C} + T_C, \quad (13)$$

$R_{P_w}, R_K, R_{R_1}, R_{R_2}, R_{R_3}, R_S, R_E, R_C$ – matrices of rotation that determine the rotation of the local systems of coordinates, whose beginnings are in points $P_w, K, R_{R_1}, R_{R_2}, R_{R_3}, S, E$ and C around their axes; $T_{P_w}, T_K, T_{R_1}, T_{R_2}, T_{R_3}, T_S, T_E, T_C$ – vectors that describe the displacements of the local systems of coordinates.

In a part of the assembly system (base p, gripper u and the body with opening o into which roller w is inserted), point P_h was selected, whose position in the local system of coordinates $O_{B_U}X_{B_U}Y_{B_U}Z_{B_U}$ was determined as a vector:

$$P_{h_U} = \begin{bmatrix} X_{B_U} \\ Y_{B_U} \\ Z_{B_U} \end{bmatrix}. \quad (14)$$

The same point is described with vector P_h that determines its position in the absolute system $OXYZ$:

$$P_h = R_{P_o} \cdot P_{h_{P_o}} + T_{P_o}, \quad (15)$$

where:

$$P_{h_{P_o}} = R_U \cdot P_{h_U} + T_U, \quad (16)$$

R_{P_o}, R_U - the matrix of rotation that determines the rotation of the local systems of coordinates, whose beginnings are located in points P_o and R_U around their axes.

5. MODELLING OF A VIRTUAL MODEL OF THE ASSEMBLY SYSTEM

The first stage of the construction of the virtual model of the mounting seat including the assembly system was the creation of models that contain the constructive geometry of its individual parts. This geometry is formed by planes, axes and constructional points as well as the beginning of the local systems of coordinates. The parameters of constructive geometry, which determines the position of the local systems of coordinates, their axes and points were written in the form of modeling variables. The values of these variables correspond to the elements of the matrix of rotation of the vectors described in Equations (5-16).

While being based on the model of the base of the assembly system, the relations were defined that occur between the remaining elements of the assembly. For the purpose of a unique determination of the position of the individual elements of the mechanism, the assembly bases that are adjacent to one another of the components to be combined were used. The view of the virtual mounting seat including the assembly system is shown in Fig. 2.

6. KINEMATIC SYSTEM OF THE ASSEMBLY SYSTEM

The structure of the assembly system shown in Fig. 2 presents the movement capacity of the $RRRPRR$ assembly robot. The movements for the individual axes are obtained with the aid of drives that transfer kinematic energy to the mobile members.

In order to determine the position and orientation of gripper e with roller w inserted in relation to the axis of the opening in the body, into which it is inserted, one needs to assign rectangular systems of coordinates to the links of the assembly system

DOI 10.1515/ama-2015-0024

in accordance with the previously presented Formulae (5-16). From the point of view of the assembly process, the determination is the most important of the mutual position of the axis of the elements to be combined: of the roller w and the axis of the opening in the body o. Hence, in further studies, the position and orientation of the roller will be analyzed. The roller w is permanently connected with the auxiliary assembly bases of the gripping part c of the gripper e, and its symmetry axis includes point Q_s, whose vector of position is described with Formula (6).

In the simulation model of the SolidWorks Motion software, in order to determine the dependencies between the configuration coordinates and the base coordinates $(\Omega_1, \Omega_2, \Omega_3, \delta_4)$ of the position and orientation of the roller in (Ω_5, Ω_6), temporary $3D$ connections were introduced that determine the position of the assembly system and its elements in the mounting seat in the starting and final positions.

One needs to take note of the fact that the local system of coordinates $O_{B_E}X_{B_E}Y_{B_E}Z_{B_E}$ with the roller w inserted is connected with the working space and it constitutes the basic system when determining the mutual positions of the elements to be combined. The system $O_{B_{R_1}}X_{B_{R_1}}Y_{B_{R_1}}Z_{B_{R_1}}$ is connected with the link r_1 and it can rotate solely by the angle Ω_1 in relation to the axis $X_{B_{R_1}}$. The local systems of coordinates $O_{B_{R_2}}X_{B_{R_2}}Y_{B_{R_2}}Z_{B_{R_2}}$ and $O_{B_{R_3}}X_{B_{R_3}}Y_{B_{R_3}}Z_{B_{R_3}}$ are connected with the r_1 and r_2 links. For these systems, rotations are possible by the angle Ω_2 in relation to the axis $Z_{B_{R_2}}$ and around the axis $Z_{B_{R_3}}$. The system of coordinates $O_{B_S}X_{B_S}Y_{B_S}Z_{B_S}$ of the linear servo-motor s is displaced in the direction of the gripper e by value δ_4. The system of coordinates $O_{B_E}X_{B_E}Y_{B_E}Z_{B_E}$ of the gripper e is placed in the central part of the gripper and is determined by rotations by the angle Ω_5 in relation to the axis Z_{B_E} and Ω_6 around the axis Y_{B_E}.

Forcing of the relative motion of the roller in order to perform a simulation of the motion was obtained through the use of virtual engines that perform a rotary motion with the following velocities: $\omega_1, \omega_2, \omega_3, \omega_4$ and ω_6. In the position of the positioning of the roller, the linear engine v_1 was started that forces the translational motion of the gripper e.

7. POSITION AND ORIENTATION OF THE ASSEMBLY ROBOT

In order to conduct simulation tests, the assembly system was selected that is presented in Fig. 2. To describe the movement path of the roller that is inserted in the opening in the sleeve, P_h and Q_s points were selected. It was accepted that these points are located on the symmetry axes of the roller and the sleeve on their frontal surfaces. The positions of these points are sought on their trajectories that are the result of the constraints imposed by the individual member and kinematic pairs of the assembly system.

Forcing of the relative motion of the roller inserted, in order to perform a simulation of the movement, was obtained by the use of the virtual drives of the individual elements of the assembly robot in accordance with the motion parameters contained in Tab.1.

The numerical analysis of the relative position of the elements of the assembly system was conducted for the centre of the roller Q_s inserted in relation to the motionless centre of the sleeve P_h. The distance between these centers ω_Δ was calculated from the following formula:

$$\omega_\Delta = \sqrt{\Delta_X^2 + \Delta_{Z_U}^2}, \tag{17}$$

where:

$$\Delta_X = X_{Q_s} - X_{P_h}, \quad \Delta_Z = Z_{Q_s} - Z_{P_h}. \tag{18}$$

Tab. 1. Parameters motion of the robot assembly

Virtual engine	Speed		Displacement		Time	
	rotational [°/s]	linear [m/s]	angular [°]	linear [mm]	commencement of motion [s]	duration of motion [s]
ω_1	150	-	90	-	0.2	0.6
ω_2	150	-	30	-	0	0.2
ω_3	150	-	30	-	0.2	0.2
v_4	-	0.6	-	120	0.8	0.2
ω_5	150	-	45	-	0.2	0.3
ω_6	180	-	90	-	0.1	0.5

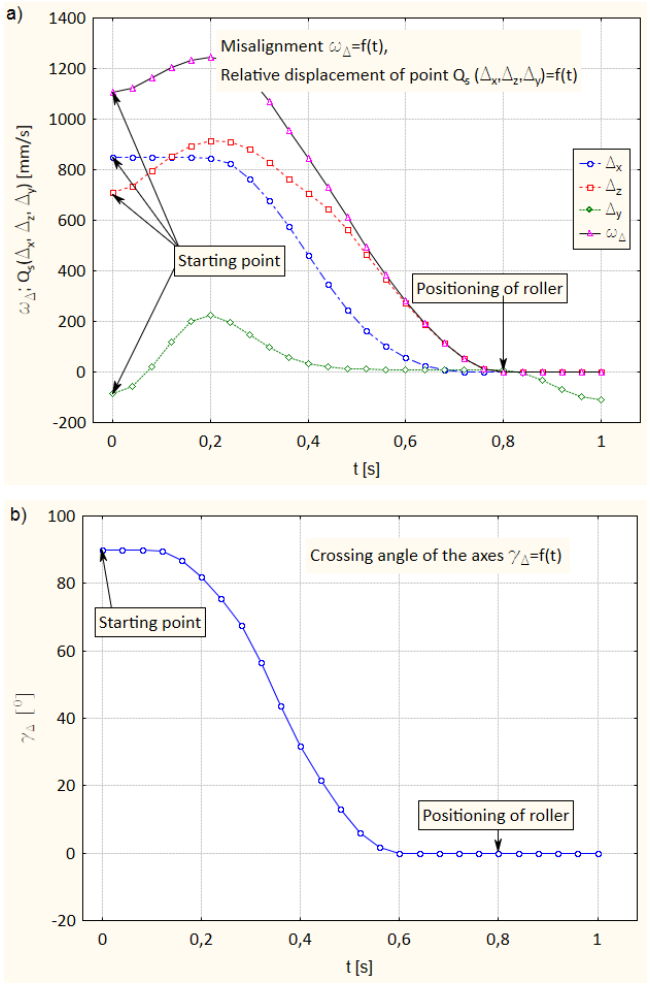

Fig. 3. Misalignment and crossing angle of the axes of the parts to be combined

The simulation model developed facilitated an easy determination of the trajectory for the known position of the point Q_s

in the global system of coordinates $OXYZ$. Fig. 3 presents the values of misalignment in the global system of coordinates $OXYZ$ and the warping angles of their axes γ_Δ of the parts to be combined along the assembly path, where Δy specifies the change of the distance between the frontal surfaces of the roller and of the sleeve. Numerical tests were conducted for the assembly system, where the individual elements are performed with absolute accuracy. This means that the value of the closing link at the moment of positioning is ω_Δ=0 mm (Fig. 3a) and the crossing angle of the axes γ_Δ = 0° (Fig. 3b).

Fig. 4 presents the formation of the misalignment ω_Δ and the warping angles y_Δ of the axes of the parts to be combined depending from the linear EL and angular EA accuracy of the elements of the assembly system and the positioning accuracy EP of the virtual engines. In the simulation tests, assembly was accepted by means of the complete variability method with identical workmanship tolerance for all the links of the measurement chain. For linear measurements, a workmanship accuracy was accepted of 8 μm, while for angular measurements, this accuracy amounted to 0.02°. The positioning accuracy of the virtual rotating engines was $\omega_{\Delta_i} = \pm$ 0.02°, and for the virtual translational servomotor, this was $\partial_{\Delta_4} = \pm$0.02mm.

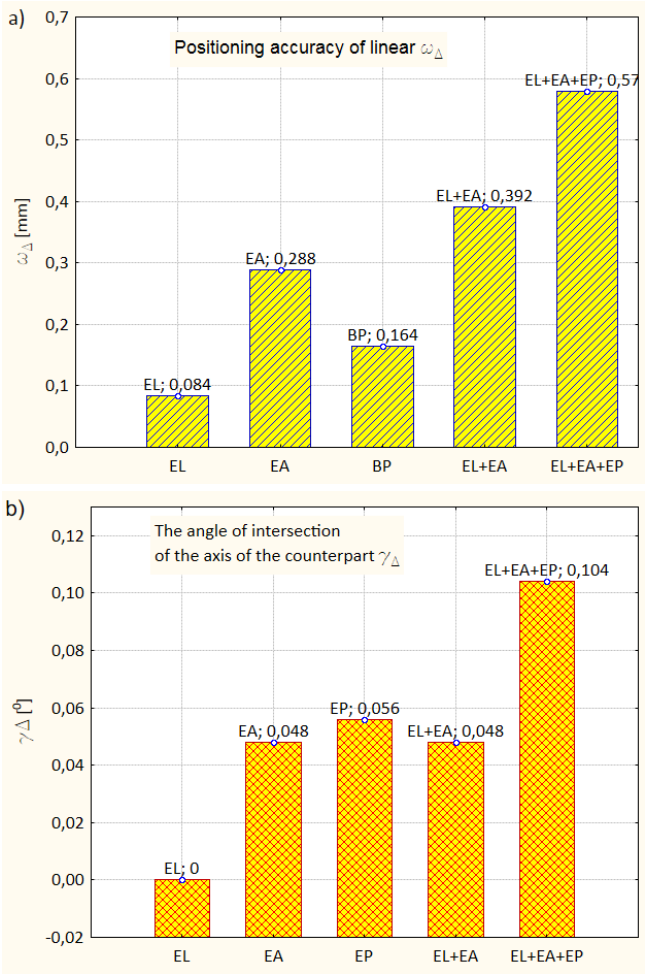

Fig. 4. Misalignment and crossing angle of the axes of the parts to be combined

The results presented of the simulation tests for the summary constituent errors $(EL + EA + EP)$ show that the greatest misalignment is ω_Δ = 0.579 mm, and the warping angle is y_Δ = 0.104°.

Owing to the values found of positioning errors, it is possible to verify the possibility of an automatic assembly of parts of the roller-sleeve type depending from the mountability conditions that are described with Equations (2 and 3). For the system under analysis, with the friction coefficient between the surfaces of the parts to be combined being μ=0.15, automatic assembly will be possible solely for clearances in combination:

8. CONCLUSIONS

This article presents the potential of the present-day CAD/CAE systems for modeling and a kinematic analysis of a virtual assembly system. The simulation model developed makes it possible to conduct numerical analyses of the assembly system based on a spatial measurement chain. Among others, this allows one to:

- investigate the accuracy of positioning and mountability conditions in automatic assembly taking into account the workmanship accuracy of the individual parts and units of the assembly system;
- determine the impact of the accuracy of the motion of those engines that drive the movable elements of the assembly system on the positioning accuracy, which will facilitate an optimal selection of the assembly robot (Żurek et al., 2011; Kuzmierowski, 2010).

The virtual simulation model constructed of an assembly system with the use of CAD/CAE computer technology takes into account numerous parameters of real assembly. The advantages that follow from the analytical model presented are huge as they allow a thorough assessment of the designs made of technical systems. The results presented in the study of simulation tests contain an illustration only of selected factors that have an influence on the work of the assembly system.

REFERENCES

1. **Ahn K., Cho D**. (2013), Proposition for a Volumetric Error Model Considering Backlash in Machine Tools, *The International Journal of Advanced Manufacturing Technology*, Vol. 15, Issue 8, 554-561.
2. **Bil T.** (2010), Kinematic analysis of a universal spatial mechanism containing a higher pair based on tori. *Mechanism and Machine Theory*. Vol.46, Issue 4, 412–424.
3. **Bil T.** (2012), Analysis of the Bennett linkage in the geometry of tori. *Mech. & Mach. Theory*, Elsevier, Vol.53, 122-127.
4. **Budniak Z.** (2013), Modeling of spatial dimension chains of mounting systems using techniques CAD/CAE. *Pomiary Automatyka Kontrola*, vol. 59, 652-655.
5. **Budniak Z.** (2014), Mountability parts of machine with rotating surface, fitted with positive clearance. *Zeszyty Naukowe Politechniki Śląskiej. Transport*, 83, 29-38.
6. **Budniak Z., Bil T.** (2012), Simulation of the movement of four-bar spatial linkage. *International Journal of Applied Mechanics and Enginering*, vol.17, No.4, 723-732.
7. **Chang K-H.** Motion Simulation and Mechanism Design with SolidWorks Motion 2011. *Schroff Development Corporation*, 1-19.
8. **Chen Y., Xie F., Liu X., Zhou Y.** (2014), Error modeling and sensitivity analysis of a parallel robot with SCARA (selective compliance assembly robot arm) motions. *Chinese Journal of Mechanical Engineering*, Vol. 27, Issue 4, 693-702.
9. **Huang S., Tsai J**. (2005), Robotic automatic assembly system for random operating condition, *The International Journal of Advanced Manufacturing Technology*, Vol. 27, Issue 3, 334-344.

DOI 10.1515/ama-2015-0024

10. **Kacalak W., Majewski M., Budniak Z**. (2015), Worm Gear Drives With Adjustable Backlash, *Journal of Mechanisms and Robotics*, Vol.8, Issue 1, p.7.
11. **Kuźmierowski T**. (2010), Analysis of the geometrical accuracy of the positioning of the effector of the parallel manipulator spatial type triplanar. *Acta Mechanica et Automatica*, Vol.4 no.1, 56-60.
12. **Liu J., Zhang Z., Liu Y.** (2012), Universal mechanism modeling method in virtual assembly environment. *Chinese Journal of Mechanical Engineering*, Vol. 25, Issue 6, 1105-1114.
13. **Liu Z., Nakamura T.** (2007), Combination of robot control and assembly planning for a precision manipulator. *The International Journal of Advanced Manufacturing Technology*, Vol. 31, Issue 7-8, 797-804.
14. **Storch B., Wierucka I.** (2007), Optyczne pomiary zarysów powtarzalnych wykorzystaniem technik przetwarzania obrazu, *Acta Mechanica et Automatica*, Vol.1, nr 2, 59-62.
15. **Tabara I., I. Dugaesescu I.** (2013), The Analysis of Part Positioning and Orientation in Robotic Assembly by Insertion. *New Trends in Mechanism and Machine Science Mechanisms and Machine Science*, Vol. 7, 509-517.
16. **Yun Y., Li Y.** (2010), Design and analysis of a novel 6-DOF redundant actuated parallel robot with compliant hinges for high precision positioning. *Nonlinear Dynamics*, Vol. 61, Issue 4, 829-845.
17. **Żebrowski-Kozioł M., Tarnowski W.** (2009), Diagnozowanie stanu luzów w połączeniach przegubowych przedniego zawieszenia samochodu, *Acta mechanica et automatica*, vol.3 no.2, 122-124.
18. **Zhu W., Mei B., Yan G., Ke Y.** (2014), Measurement error analysis and accuracy enhancement of 2D vision system for robotic drilling. *Robotics and Computer-Integrated Manufacturing*, Vol. 30, Issue 2, 160-171.
19. **Żurek J., Ciszak O., Cieślak R., Suszyński M.** (2011), Assessment and choice of an industrial robot with the use of AHP method. *Archives of Mechanical Technology and Automation*, Vol. 31, nr 2, 201-211.
20. **Żurek J., Wiśniewski M.** (2013), The methodology and research conditions of Fanuc M-16iB industrial robot positioning accuracy and repeatability. *Technologia i Automatyzacja Montażu*, 2013, Vol.1, 31-34.

This project has been funded by the National Science Centre on the basis of the decision no. DEC-2012/05/B/ST8/02802.

ACCURACY OF POSITIONING AND ORIENTATION OF EFFECTOR OF PLANAR PARALLEL MANIPULATOR 3RRR

Monika PRUCNAL-WIESZTORT*

*Faculty of Mechanical Engineering, Wrocław University of Technology, ul. Łukasiewicza 5, 50-371 Wrocław, Poland

monika.prucnal@pwr.wroc.pl

received 25 November 2014, revised 9 October 2015, accepted 15 October 2015

Abstract: Parallel manipulator belongs to group of mechanisms with closed kinematic chains. This feature involves both advantages and disadvantages. The study examined the issue of accuracy of a planar system with three degrees of freedom, with revolute pairs, showing the effect of errors of the drives settings on effector positioning deviation. Enclosed is a numerical example for which analyzed the deviation in motion manipulator when going through the singular configuration. Based on the analysis was determined the area around the singular positions for which to obtain the orientation of the assumed accuracy is impossible.

Key Words: Accuracy, Planar Parallel Manipulator, Singularities

1. INTRODUCTION

Parallel manipulator belongs to group of mechanisms with closed kinematic chains. This feature involves both advantages and disadvantages. Desirable features include ability to transfer heavy loads, stiffness, accuracy of trajectory mapping (or positions), ability to gain high speed of operating element, which is result of good dynamic properties of the system due to possibility to placing of heavy active elements at the basis. But closure of the kinematic chain significantly reduce range of motion of the effector (Bikhari et al., 2014). Additionally, dividing the work zone, resulting from the range of possible positions of the intermediate elements and active elements on areas dependent on the mutual configuration of the system on subzones achievable for certain mutual configurations of the system elements, causes that moving between the subzones is possible after disassembly and assembly of the mechanism. Division into subzones is caused by occurrence of singular positions from direct kinematics inside of zone indicated by singular positions of inverse kinematics.

The particular configuration of the mechanism, called singular position, influencing on properties of the system – ceases to be effectively controllable (in this configuration the system loses its properties staring from motility, although they are characteristic within all other areas of the working zone). Singular positions appears in many analysis of parallel manipulator movements independently to adopted method of description (Bałchanowski, 2014).

2. SCOPE OF WORK

Scope of this study was to show the impact of the errors of the drive settings on deviation of effector's positioning and orientation. There was examined accuracy of parallel mechanism with three degrees of freedom with rotating kinematics pairs – 3RRR. Was done description of configuration of the mechanism and derived deviation equations. The whole was illustrated by an example. Purpose of attached numerical example was to show deviations of effector movement while passing trough singular positions.

3. DESCRIPTION OF THE MANIPULATOR CONFIGUATION

Studied parallel manipulator contains three kinematic chains connecting the effector 7 with the base (Fig. 1). Active elements 1, 2, 3 are placed at the base. Intermediate elements 4, 5, 6 connect active elements with effector.

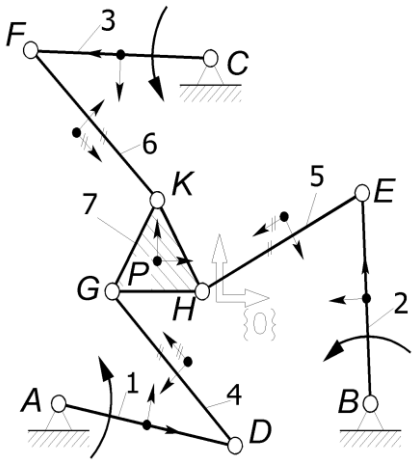

Fig. 1. The parameters of description of the position of elements in absolute coordinates

Description of the configuration of the mechanism was made using absolute coordinates. Every element was bound with local coordinate, which position and orientation described with vector $\boldsymbol{q}_i = [x_i \; y_i \; \Theta_i]^T$ are the same as position of element i. Configuration of the mechanism is described then by the following system:

DOI 10.1515/ama-2015-0025

$$\Phi_l(\mathbf{q},t)=\begin{bmatrix}\Phi^W(\mathbf{q})\\ \Phi_l{}^C(\mathbf{q},t)\end{bmatrix}=0. \quad (1)$$

First group of equations Φ^W describes chains of kinematic pairs, second group is kinematic motion describing movement of active elements $\Phi_l{}^C$, where l ={1,2} depending on direct or inverse kinematic.

After differentiation of equation (1) velocity equation is given as

$$\Phi_{l_q}(\mathbf{q},t)\dot{\mathbf{q}}=-\Phi_t\equiv v. \quad (2)$$

This record is compatible with the derivatives of the Lagrangian symbology, wherein the index t is the time derivative and Φ_{l_q} is jacobian $\Phi_{l_q}=\partial\Phi_l/\partial\mathbf{q}$.

After transformation equation (2) takes the form

$$\dot{\mathbf{q}}=-\Phi_{lq}^{-1}\Phi_t. \quad (3)$$

It should be noted that equation (3) has solution for det $(\Phi_{l_q})\neq 0$, otherwise there is singular position.

4. ACCURACY ANALYSIS

An important property of the system is accuracy of realization of the movement of the passive element (Briot and Bonev, 2008; Tannous et al., 2014; Yu et al., 2008; Zhang et al., 2014). For the known configuration it is possible to determine values which describe deviations resulting from drives setting errors.

Starting from equation (1) using the variance of function of pair chains Φ^W, deviations are determined

$$\Phi^W=0\rightarrow\Phi_{\mathbf{q}}^W\delta\mathbf{q}=0, \quad (4)$$

where: $\Phi_{\mathbf{q}}^W=\frac{\partial\Phi^W}{\partial\mathbf{q}}$.

Similar to vector of variables it is possible to distinguish vectors of conditional deviations and uninfluenced deviations as:

$$\delta\mathbf{q}=[\delta\mathbf{q}_Z^T\quad\delta\mathbf{q}_C^T]^T. \quad (5)$$

Deviations vector $\delta\mathbf{q}_C$ is given value coming from type of used drivers and control system. After taking into account (5) equation (4) transforms to

$$\Phi_{qZ}^W\delta\mathbf{q}_Z+\Phi_{qC}^W\delta\mathbf{q}_C=0 \quad (6)$$

and allows to find conditional deviations from equation:

$$\delta\mathbf{q}_Z=-\left[\Phi_{qZ}^W\right]^{-1}\Phi_{qC}^W\delta\mathbf{q}_C \quad (7)$$

the equation has unique solution for det $(\Phi_{qZ}^W)\neq 0$.

Equation (7) allows to determine deviations of point P in relation to nominal positions under condition of knowledge of value and sign of drives setting error $\delta\mathbf{q}_C$. Because at stage theoretical considerations information about used drive and control system (errors of setting of active elements) is not available, then the maximum deviation values are determined resulting from errors of setting of n drives basing on relation (8)

$$\begin{aligned}\delta x_{P\max}&=\textstyle\sum_{i=1}^3|w_{xi}\delta q_{Ci}|\\ \delta y_{P\max}&=\textstyle\sum_{i=1}^3|w_{yi}\delta q_{Ci}|\\ \delta\Theta_{3\max}&=\textstyle\sum_{i=1}^3|w_{\Theta_{3i}}\delta q_{Ci}|\end{aligned}. \quad (8)$$

In equation (8) values of $\delta\mathbf{q}_i$ are known, and values of w_{xi}, w_{yi}, $w_{\Theta_{3i}}$ are influence factors defined according to equations:

$$\begin{aligned}w_{xi}&=\frac{\delta x_P}{\delta q_{Ci}}\\ w_{yi}&=\frac{\delta y_P}{\delta q_{Ci}}\\ w_{\Theta_{3i}}&=\frac{\delta\Theta_3}{\delta q_{Ci}}\end{aligned}. \quad (9)$$

Values of influence factors from individual drives are determined basing on known components of vector $\delta\mathbf{q}_C$, while calculating influence of setting error of drive k $\delta\mathbf{q}_{C_k}$), remaining two has value of zero: $\delta\mathbf{q}_{C_m}=\delta\mathbf{q}_{C_j}=0$ for $m,j\neq k$.

Value of influence factor depends only on configuration of the system and allows the accuracy analyze independent from values of errors of setting of individual drives.

5. CALCULATION EXAMPLE

Model described above was implemented into mechanism described on Fig. 2, which dimensions are presented in Tab. 1.

Tab. 1. Dimensions of the analyzed manipulator

Element	symbol	mm
Base	$AB=BC=CA$	173
Crank	$l_1=l_2=l_3$	200
Connector	$l_4=l_5=l_6$	200
Effector	$GH=HK=KG$	100

In order to use method described above, condition of solution of equation (7) must be checked. This equation has solution for det (Φ_{qZ}^W) ≠ 0 (Choi et al., 2013; Firmani and Podhorodeski, 2009; Huang and Thebert, 2010). Following is determinant of the matrix Φ_{qZ}^W (Gronowicz and Prucnal-Wiesztort, 2006):

$$\begin{aligned}det\,(\Phi_{qZ}^W)\;=\;&({}^4x_G-{}^4x_D)({}^5x_H-{}^5x_E)({}^6x_K-{}^6x_F)\\ &\{sin(\Theta_6-\Theta_5)\,({}^7x_G\,sin(\Theta_4-\Theta_7))-{}^7y_G\,cos(\Theta_4-\Theta_7))\\ &+sin(\Theta_4-\Theta_6))({}^7x_H\,sin(\Theta_5-\Theta_7)-{}^7y_H\,cos(\Theta_5-\Theta_7))\\ &+sin(\Theta_5-\Theta_4))({}^7x_K\,sin(\Theta_6-\Theta_7)-{}^7y_K\,cos(\Theta_6-\Theta_7))\}\end{aligned} \quad (10)$$

which corresponds to the value of determinant of Jacobian matrix for direct kinematic.

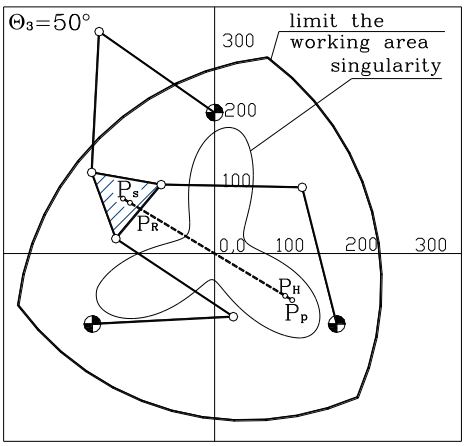

Fig. 2. Realized trajectory

Singular positions of direct kinematic are possible to determine for planar kinematic systems with three degree of freedom using their graphic interpretation (Fig. 3).

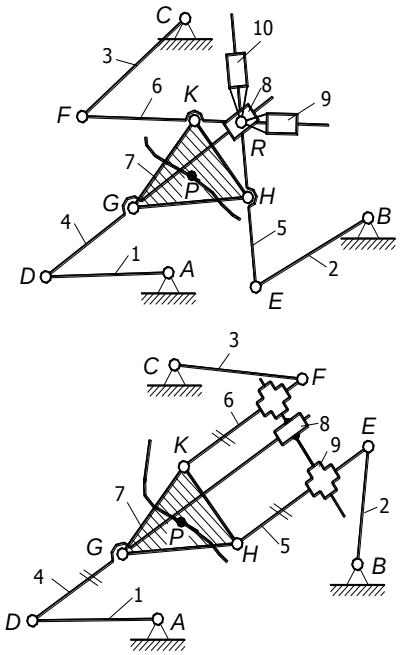

Fig. 3. Supporting mechanisms

After implementation of additional elements, mobility of supporting mechanisms for: n=11, p1=14, p2=0 is equal to:

$$W = 3(n-1) - 2p_1 - p_2 = 3 \cdot 10 - 14 \cdot 2 = 2. \qquad (11)$$

For known orientation of effector degree of freedom is 1, which indicates continuity of singular configuration for given orientation. Working area for chosen orientation of effector with singular positions is presented on Fig. 4.

In this situation answer for question about value of deviations of positions and orientation of effector caused by errors of setting of the drives require specific analyze. Because usage of equation (7) throughout the range of motion expected it was decided, that analyze basing on solving of direct kinematic for nominal values of setting of the drives will be performed, and then the solution of a direct kinematic for all conceivable variations of displacement settings of the three drives. This is the basis for the adoption of additional procedures for analyzing all the deviations and selecting maximum disadvantageous of their systems, which in turn allows to specify the range of possible trajectory deviations. For this purpose algorithm was built (Fig. 5). Analyze of the accuracy of realization of the trajectory was determined as the difference between the nominal values of the position and orientation of the effector and the designated coordinates of the point P and the orientation Θ_3 of specific effector assumed with misalignment of the drives. Near the singular positions algorithm for the positions go on polynomial record, where the variable was the angle of orientation of the platform Θ_3. The displacement values of the drives set were assumed on the level of Δu_i=±0.001rad.

In Tab. 2 were shown parameters of realized trajectory, where P_S is starting point, P_R is the point from which traffic moves at a constant speed v_P, P_H – the point at which braking occurs,

In the Tab. 2 shows the parameters of the realized trajectory, the P_S is the starting point, P_R point from which traffic is moving at a constant velocity v_P, P_H - the point at which braking occurs, P_P - staging point lasting for the duration of T_P, followed by return to the P_S.

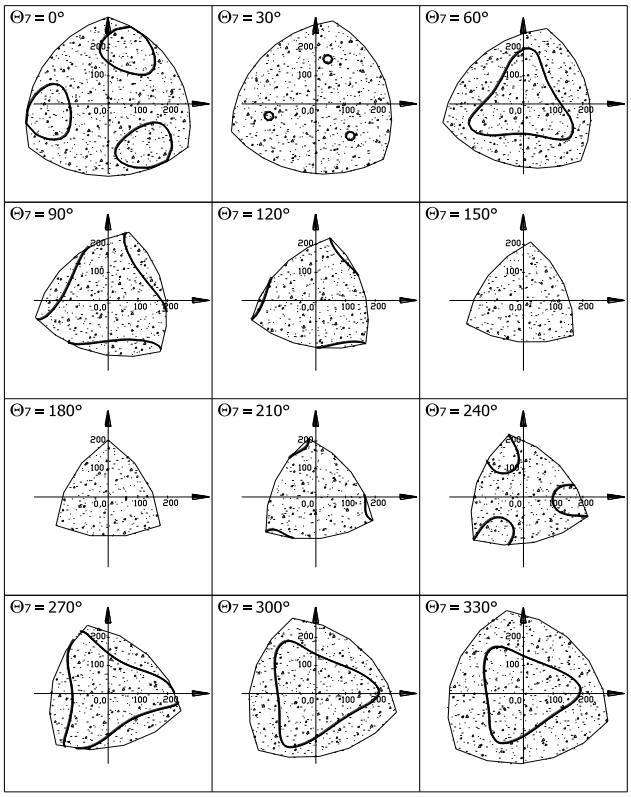

Fig. 4. Singular position against the work area

Tab. 2. Parameters of trajectory

$P_S\ (x,y)$ mm	$P_R\ (x,y)$ mm	$P_H\ (x,y)$ mm	$P_P\ (x,y)$ mm	T_P s	v_P m/s
-130, 78	-120, 72	100, -60	110, -66	3	0.06

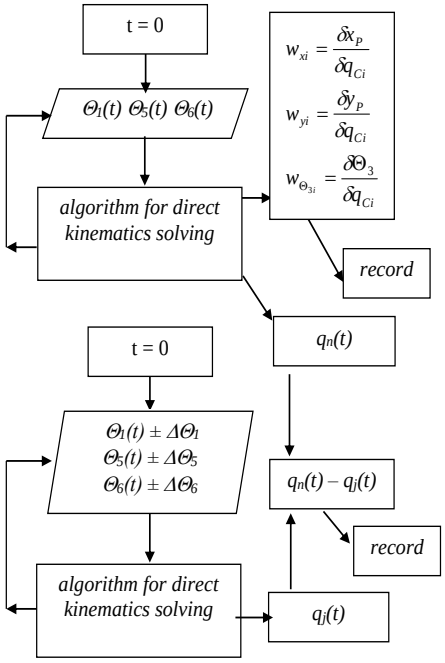

Fig. 5. A block diagram of algorithm accuracy

DOI 10.1515/ama-2015-0025

The results show that the trajectory in the working area with singular positions deviation of positioning and orientation of the effector dramatically increases. Fig. 6 shows the resulting deviation of the effector orientation.

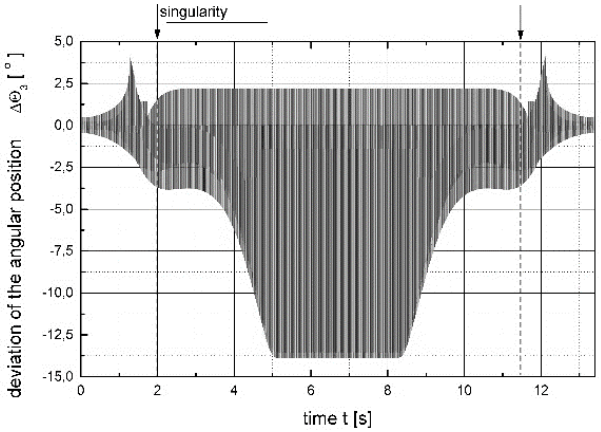

Fig. 6. Deviation of orientation $\Delta\Theta_3$

Permissible error of effector orientation was adopted at 3°. Such an approach entails a condition limiting the permissible zone.

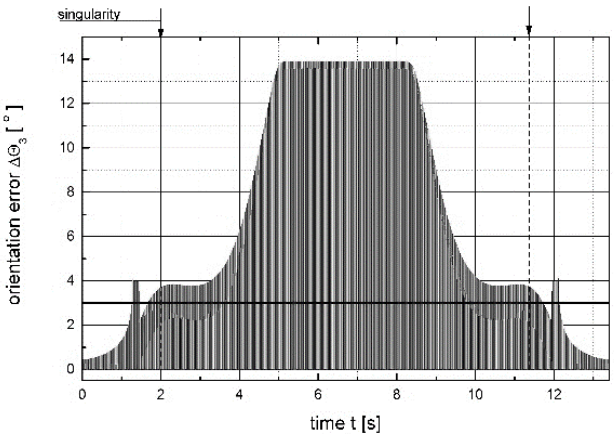

Fig. 7. Deviation of orientation during effector movement $\Delta\Theta_3$

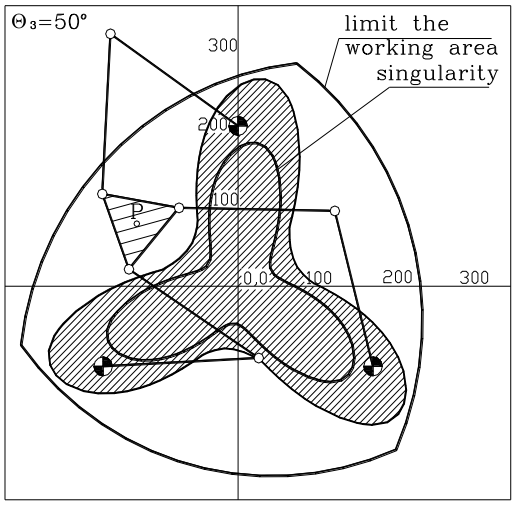

Fig. 8. Permissible working area for orientation of effector $\Delta\Theta_3$=50° (criterion of accuracy)

Basing on the analysis was defined area around the singular positions, for which achievement of orientation at predetermined accuracy is not possible (hatched in Fig. 8).

Working area for the orientation of the effector $\Delta\Theta_3$=50° has been significantly reduced. Practically the entire central portion is not available.

6. CONCLUSION

The study examined the issue of accuracy of the parallel mechanism with three degrees of freedom – $3RRR$. After derivation of equation of the deviation a numerical example was presented, for which is given manipulator working zone with different orientations including singular positions of the direct kinematics. Purpose of attached numerical example was to show deviations of effector movement while passing trough singular positions.

Based on the analysis was determined the area around the singular positions for which to obtain the orientation of the assumed accuracy is impossible (hatched in Fig. 8). Work area for effector orientation $\Delta\Theta_3$=50° has been significantly reduced. Practically the entire central portion is not available. This points to the need for a significant limitations and such a small work area of analyzed manipulator, which may preclude it from practical applications.

REFERENCES

1. **Bałchanowski J.** (2014), Topology and analysis of the singularities of a parallel mechanism with three degrees of freedom, *Archives of Civil & Mechanical Engineering*, 14(1), 80-87.
2. **Banke B., Dhiraj K., Chandan J., Vijay S.** (2014), Rathore and Anjan Kumar Dash A geometric approach for the workspace analysis of two symmetric planar parallel manipulators, *Robotica*, FirstView, 1 – 26.
3. **Briot S., Bonev I. A.** (2008), Accuracy analysis of 3-DOF planar parallel robots, *Mechanism and Machine Theory*, 43(4), 445-458.
4. **Choi J. H., Seo T., Lee J. W.** (2013), Singularity Analysis of a Planar Parallel Mechanism with Revolute Joints based on a Geometric Approach, *International Journal of Precision Engineering and Manufacturing*, 14(8), 1369-1375.
5. **Firmani F., Podhorodeski R. P.** (2009), Singularity analysis of planar parallel manipulators based on forward kinematic solutions, Mechanism & Machine Theory, 44 (7), 1386-1399.
6. **Gronowicz A., Prucnal-Wiesztort M.** (2006), Singular configurations of planar paralel manipulators, *Archves of Civil and Mechanical Engineering*, 6(2), 21-30.
7. **Huang M. Z., Thebert J.-L.** (2010), A study of workspace and singularity characteristics for design of 3-DOF planar parallel robots, *International Journal of Advanced Manufacturing Technology*, 51(5-8), 789-797.
8. **Tannous M., Caro S., Goldsztejn A.** (2014), Sensitivity analysis of parallel manipulators using an interval linearization method, *Mechanism & Machine Theory*, 71, 93-114.
9. **Yu A., Zsombor-Murray P., Bonev I. A.** (2008), Geometric approach to the accuracy analysis of a class of 3-DOF planar parallel robots, Mechanism and Machine Theory, 43(3), 364-375.
10. **Zhang Q. H, Fan X. R., Zhang X. M.** (2014), Dynamic Analysis of Planar 3-(R)under-barRR Flexible Parallel Robots with Dynamic Stiffening, Shock and Vibration, Article ID 370145, 1-13.

APPLICATION OF SHAPE MEMORY ALLOY IN HARVESTO-ABSORBER SYSTEM

Krzysztof KĘCIK*

*Faculty of Mechanical Engineering, Department of Applied Mechanics, Lublin University of Technology, 20-618 Lublin, Poland

k.kecik@pollub.pl

received 4 May 2015, revised 27 October 2015, accepted 28 October 2015

Abstract: This paper presents a conception of the harvester-absorber system consisting of two parts. The first is the pendulum attached to the main system (oscillator), which is suspended on the linear damper and the nonlinear spring made of shape memory alloy. The spring is modelled as a polynomial function based on Landau–Ginzburg theory of phase transitions (similar as ferroelectric and ferromagnets). The obtained results show, that SMA element can increase harvesting energy level, while the absorber effect can be impaired (but not loss). Additionally, introducing SMA element causes changes in dynamics, introduces a new unstable solutions and bifurcations. The analysis was done by classical integration and continuation solution methods.

Key words: Pendulum, SMA Spring, Energy Harvester, Vibration Absorber, Control, Continuation Method

1. INTRODUCTION

The dynamic vibration absorber is proved to be a very simple and effective vibration suppression device, with many practical implementations in civil and mechanical applications. While, the energy harvesting is a promise to recovery energy from unwanted vibrations (Kecik and Borowiec, 2013). The pendulum mechanism can be used in different mechanical systems for various purposes. The application for vibration absorption or energy harvesting is one of the most common. The dynamic vibration absorbers (DVAs), also called Vibration Neutralizers (VNs) or Tuned Vibration Absorbers (TVAs), are mechanical appendages comprising inertia, stiffness, and damping elements which, once connected to another mechanical system, or structure called the primary system or machine are capable of absorbing on controlling the vibrations (Liao et al., 2011).

In the literature studies (Kaynia et al., 1981; Regis, 2010, Sladek and Klingner, 1983; Soto-Brito and Ruzi, 1999) it is shown, that the effectiveness of linear vibration absorbers is limited to the close neighborhood of a vibration mode. This frequency robustness limitation called for the development of nonlinear vibrations absorber (NLVA). On the most popular NLVA are the autoparametric vibration absorbers (AVAs) (Kecik, 2015). The idea of such solutions lies in attaching the absorber to the primary structure in such a manner that it experiences a parametric base excitation, and therefore, the absorber frequency is tuned around one-half of the troublesome frequency value. The equations of motion of such system include the quadratic nonlinearities, and inertial terms, which can influence parametric resonance (Warminski and Kecik, 2009).

Moreover, such systems exhibit different nonlinear mechanism (e.g., saturation (Oueini et al., 1997), quenching, sub/ superharmonic resonances, autoparametric resonances (Warminski and Kecik, 2009), 0:1 resonances (Lacarbonara, 2012)) can be leveraged to produce effective actuator actions for resonance rejection in nonlinear lumped and distributed-parameter systems. Additionally, they are very sensitive to system's parameter, therefore the control method to maintain demand solution should be applied.

In this aim, the application of smart material (SM) seems very promising. Nowadays, the most used materials are the shape memory alloys (SMA), the piezoelectric materials (PM), the magnetostrictive materials (MSM) and the electro- and magneto-rheological fluids (MRF) (Janocha, 2007). These materials have the ability of changing their shape, stiffness, among other properties, through the imposition of temperature or stress, electrical or electro-magnetic fields. The SMAs are a kind of smart materials whose physical properties change as a function of temperature. This effect can be exploited to build tunable and adaptive devices.

On the other hand, in nonlinear vibrating systems energy harvesting (EH) recovery is possible, too (Kecik and Borowiec, 2013; Xu and al., 2007; Wiercigroch, 2011). EH has been an active research area and systems refer to devices that capture and transform energy into electricity. Usually, the energy could be recovered from the kinetic energy of moving or vibrating structures. The vibration based energy harvesters can be categorized into three main types, namely: electromagnetic, piezoelectric, and electrostatic (depending on the medium of the transducer).

The civil structures and pendulum absorbers usually exhibit low frequency structural vibrations, which make it difficult for an energy harvester to extract energy. Therefore, tuning of such systems is very important. The vibrational energy harvesters achieve their highest output power nearly resonance regions (because of the highest amplitude of vibration) (Gu and Livermore, 2010). The application of smart elements can increase the resonance region (Kecik, 2015) and improved power recovery. The novel conception for simultaneous vibration absorption and the energy recovery in this paper is proposed. The harvesto-absorber system consists of oscillator with added absorber (pendulum). In the pivot of absorber, the energy harvesting device is mounted.

The proposed conception can be used for swinging or rotation of the pendulum. To control of dynamics, the SMA spring mounted in the suspension of the main system is applied. The SMA spring

DOI 10.1515/ama-2015-0026

beahavior is described by the polynomial model, which characterizes relationship between strain, stress and temperature. The main idea of this work is influence analysis of nonlinearity of SMA spring on dynamics, absorption effect and energy harvesting problem.

2. ENERGY HARVESTING DYNAMIC VIBRATION ABSORBER (EHDVA)

2.1. Model of a pendulum-like system

A schematic diagram of the proposed energy harvesting dynamic vibration absorber (EHDVA) is shown in Fig. 1. The system consits of two main parts. The first is a pendulum (absorber) made up two masses (m_2 and m_3) and a length denoted as l. The second part is called the main system (oscillator) suspended on the linear damper (where c is a viscous damping coefficient) and nonlinear SMA spring. Assumed, that the main system can move only in vertical direction.

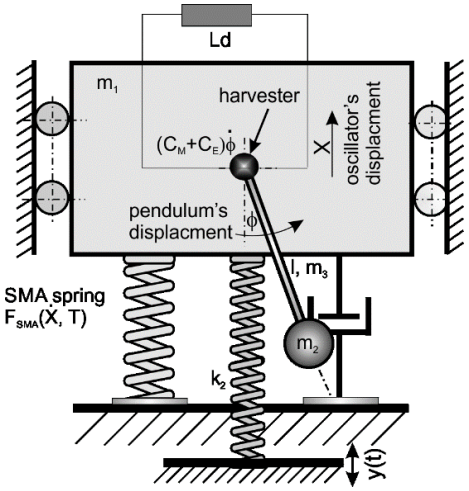

Fig. 1. Schematic diagram of the energy harvesting vibration absorber

Fig. 2. Real view of EHDVA system with SMA oscillator's spring

The system is excited with help of the linear spring with stiffness denoted as k_2 (kinetic excitation). The excitation of end spring is a harmonic function $y(t) = Qcos(\omega t)$. The system has two degree of freedom: x vertical displacement of the oscillator and ϕ angular displacement of the pendulum. In the pendulum pivot, the energy harvesting device is mounted. Therefore, the total damping of the pendulum consists of the mechanical viscous (c_M) and electrical (c_E) damping.

The harvester device is connected directly to the electric load (Ld). Note that parameters of model identified on the experimental system, presented in Fig. 2. Detailed information about experimental system can be found in Kecik (2015).

2.2. Model of SMA spring

The most popular constitutive models for describing the behavior of SMAs come from the original Landau-Ginzburg theory of phase transitions. This theory describes the constitutive information about SMA material by a polynomial free-energy, function whose partial derivatives provide constitutive equations for strain (ε) and entropy. In Falk (1980), Falk proposed a Landau-Devonshire like free-energy function based on the analogy between SMA uniaxial stress-strain curves and the electric field magnetization curves of ferromagnetic materials. This model assumes a polynomial free energy potential, which allows pseudoelasticity and SME description. The free energy potential (W) is defined as

$$W(T,\varepsilon) = \frac{a_1}{2}(T - T_1)\varepsilon^2 - \frac{1}{4}a_2\varepsilon^4 + \frac{a_2^2\varepsilon^6}{24a_1(T_A - T_M)}, \quad (1)$$

where parameters a_1, a_2 are positive constants, while T_M and T_A are the temperature below the martensitic and austenite phase are stable, while T is activated SMA temperature.

By applaying the stress-strain relation

$$\sigma(\varepsilon,T) = \frac{\partial W(\varepsilon,T)}{\partial \varepsilon}, \quad (2)$$

and replacing strain by the displacement, obtained function describing ellogation of SMA spring versus temperature

$$F_{SMA}(x,T) = \tilde{a}_1(T - T_M)x - \tilde{a}_2x^3 + \frac{\tilde{a}_2^2x^5}{4a_1(T_A - T_M)}. \quad (3)$$

The parameters $\tilde{a}_1$, $\tilde{a}_2$, $\tilde{a}_3$ are positive material constants includes cross-section of the SMA material spring.

2.3. Energy harvesting device conception

A typical vibration EH system consists of a mechanical system with external excitation, a transducer that converts the vibration energy into electric energy, mechanisms for motion transmission and magnification, power electronics and energy storage elements, and energy management.

The rotatory harvester device is mounted in the pendulum suspension. The harvester consists of two main elements, a stator and a rotor. Additionally, it includes two identical windings fixed to housing. When the pendulum is rotating or swinging, the converter generates electricity due to magnetic induction. Generally, inductive energy depends on a relative velocity between the coil and the magnet and electrical properties of circuits. Because of small size of harvester device (compared to total system), assumed that it is dynamics not influence on vibrations of other components. The

scheme of energy harvester system and electric circuit in Fig. 3 is shown. The parameter ρ denotes housing radius, while δ is a transduction factor, which depends on numbers of coil turns, average magnetic field strength, and the coil length.

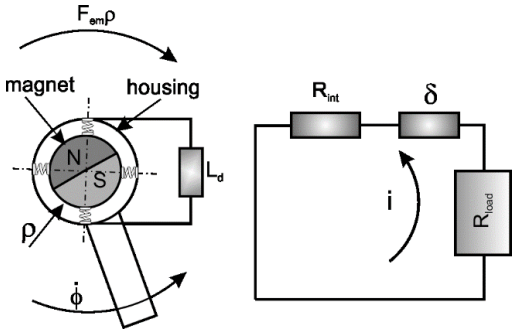

Fig. 3. Schematic diagram of inductive energy and equivalen circuit

The total electromotive (electromagnetic) force generated by the windings denoted F_{em}, can be written as (Ma et al., 2012)

$$F_{em} = \delta i = c_e \dot{\varphi}. \tag{4}$$

The coupling term of the mechanical system with the electric circuit is directly proportional to the angular velocity and electrical damping of the electrical device (Kecik and Borowiec, 2013). This means that is equivalent to a viscous damping force with a damping coefficient c_e. From mathematical point of view, equations of motion for the pendulum harversto-absorbers system are identical as system without harvester device. However, the harvester devices slightly increases damping of the pendulum.

To calculate the electrical damping coefficient c_e, the equation for the electrical circuit is used by applying Kirchhoff's law

$$i(R_{load} + R_{\text{int}}) - \delta\rho\dot{\varphi} = 0, \tag{5}$$

where R_{load} is the resistance of the external load, R_{int} is the internal resonance.

The recovered voltage can be calculated using classical Ohm's law

$$U = iR_{load} = \delta \frac{\rho R_{load}\dot{\varphi}}{(R_{load}+R_{\text{int}})}, \tag{6}$$

where i denotes current.

Then, the electrical damping coefficient can be calculated

$$c_E = \frac{\rho\delta^2}{(R_{load}+R_{\text{int}})}, \tag{7}$$

which depends on the construction of harvester device and property of electrical circuit.

2.4. Dimensional and non-dimesional equations of motion

The dynamics of the primary mass (m_1), and the absorber (m_2 and m_3), can be described by two coupled ordinary differential equations (ODE). The equations are coupled by inertial terms, which is typical for autoparametric systems. The equations of motion of model presented in Fig. 1 have form:

$$(m_1 + m_2 + m_3)\ddot{x} + c\dot{x} + F_{SMA}(T,x) + (m_2 + m_3/2)l\,(\ddot{\varphi}\sin\varphi + \dot{\varphi}^2\cos\varphi) = k_2 Q\cos(\omega t), \tag{8}$$

$$(m_2 + m_3)l^2\ddot{\varphi} + (c_M)\dot{\varphi} + (m_2 + m_3/2)l(\ddot{x} + g)\sin\varphi + \delta i = 0, \tag{9}$$

where F_{SMA} describes force of SMA spring which depends of temperature and its deflection.

Introducing dimensionless time $\tau = \omega_o t$, where ω_o is a natural frequency of the oscillator, $X = x/x_{st}$ (where x_{st} is a static displacement of the oscillator) and replacing part δi (eq. (4)) obtained eqs. (8) and (9) in dimensionless form are:

$$\ddot{X} + \alpha_1\dot{X} + (\theta - 1)X - \beta_1 X^3 + \beta_2 X^5 + \mu\lambda(\ddot{\varphi}\sin\varphi + \dot{\varphi}^2\cos\varphi) = q\cos(\vartheta\tau), \tag{10}$$

$$\ddot{\varphi} + (\alpha_2 + \kappa)\dot{\varphi} + \lambda(\ddot{X} + 1)\sin\varphi = 0. \tag{11}$$

The dimesionless parameters are defined:

$$\begin{aligned}
&\tau = \omega_0 t,\quad \omega_0^2 = \sqrt{\frac{a_1 T_M}{M}},\quad X = \frac{x}{x_{st}},\quad \vartheta = \frac{\omega}{\omega_0},\quad \theta = \frac{T}{T_M},\\
&\theta_c = \frac{T_A}{T_M},\ \beta_1 = \frac{a_2 x_{st}^2}{\omega_0^2 M},\ \beta_2 = \frac{\beta_1^2}{4(\theta_c - 1)},\ x_{st} = \frac{gM}{a_1 T_M},\\
&M = \textstyle\sum_{i=1}^{3} m,\ \alpha_1 = \frac{c}{\omega_0 M},\ \alpha_2 = \frac{c_M}{\omega_0 l^2(m_2+m_3/3)},\\
&\lambda = \frac{(m_2+m_3/2)x_{st}}{(m_2+m_3/3)l}, \mu = \frac{(m_2+m_3/2)l^2}{Mx_{st}^2},\\
&q = \frac{k_2 Q}{(k+k_2)x_{st}},\ \kappa = \frac{c_E}{(m_2+m_3/3)l\omega_0}.
\end{aligned} \tag{12}$$

The dimensionless equations of motion are easy to analysing because of lack of units and small number of parameters.

In the dimensionless form the eq. (3) resorting force of SMA spring has a form

$$F_{SMA}(X,T) = (\theta - 1)X - \beta_1 X^3 + \beta_2 X^5, \tag{13}$$

where definition of dimesionless material constant are explained in (12). Note, for $\beta_1 = \beta_2 = 0$ and θ=2, SMA's model exhibits linear behavior like classical linear spring. The examplary characteristics of SMA spring model in Fig. 4 are presented. The black line presents classical linear characteristics, while blue line denotes temperature θ=0.75, green θ=1 and red θ=1.5.

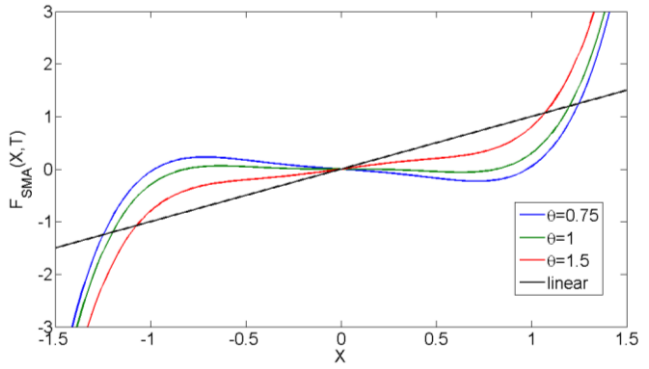

Fig. 4. Force-displacement characteristics of SMA spring for β_1=0.6, β_2=0.9

The proposed model shows strongly nonlinear behaviour, especially for large displacement. For small value of displacement (x <0.5) characteristics are close to linear. All parameters describing the harvesto-absorber system and SMA spring are identified on the laboratory rig.

DOI 10.1515/ama-2015-0026

3. NUMERICAL ANALYSIS

3.1. Influence of the SMA spring on absorption effect

The absorption region for the pendulum absorber system with the classical linear spring is known very well (Warminski and Kecik, 2006). This region, existing for properly tuned system, near the resonace peak (Kecik et al., 2014). However, for system with the SMA spring the dynamics can diametrically changed. Considering the system as a dynamic absorber, it is necessary to understand the infuence of SMA stiffness spring on this effect. Additionally, the application of SMA spring in oscillator's suspension can be an alternative way to control the absorber dynamics. The suspension with the SMA spring is easy to apply in the real construction. Note, that the control by the element mounted in the pendulum pivot (e.g. rotatory damper) is difficult due to the harvester. Alternative control for such systems can be realized by the oscillator's damper. In papers (Cartmell and Lawson, 1994; Vazquez-Gonzalezal and Silva-Navarro, 2008), the effective control by magnetorheological damper mounted in the oscillator's suspension is proposed.

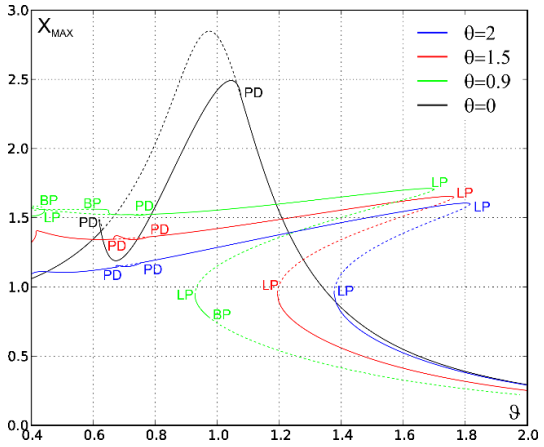

Fig. 5. Frequency response curves for the oscillator, for β_1=0.6, β_2=0.9 and different temperature ratio

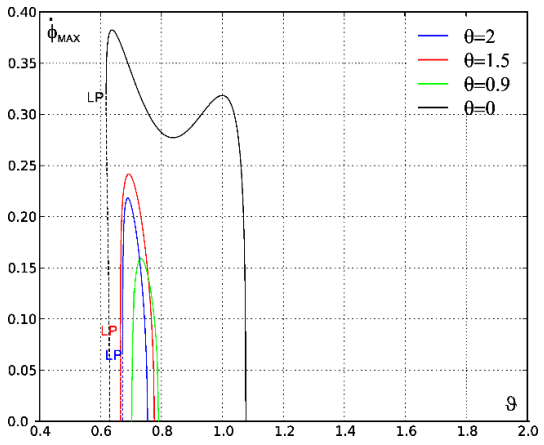

Fig. 6. Frequency response curves for the pendulum velocity, for β_1=0.6, β_2=0.9 and different temperature ratio

The calculations in this section have been performed using software for numerical continuation, Auto07p (Doedel at al., 2011). The results that have been obtained by continuation give us an overview of system dynamics demonstrating all possible periodic solutions. The exemplary frequency response curves are presented in Fig. 5.

The simulation parameters are: α_1=0.32, α_2=0.0769, q=0.9, μ=17.2, λ=0.12, κ=0.0031. The dashed dotted line denotes unstable, while continous lines stable solutions. The labeled point describes the bifurcations points (PD –pediod doubling, LP – limit (fold) point, BP branch point).

The frequency response curves, for harvesto-absorber system with clasical spring (θ=2, β_1=β_2=0), marked by the black line in Figs. 5 and 6 are presented. The absorption region is clearly visible, for frequency range ϑ≈0.6-1.05. Unfortunatelly, for system with the SMA spring, the absorption region is very small, and located between 0.65 and 0.8. The size of this region depends on the temperature, and additionaly, the effectivness level of vibration absorption is very low. However, the amplitude of semi-trivial solution (vibrates only the main system) is significantly reduced. The resonance curves were bent in the rigt side, and for lower temperature, the semi trivial solution changes in unstable (see, the green line in Fig. 5).

The SMA spring can be used to control of the pendulum velocity, as shown in Fig. 6. The temperature changes cause increase or decrease in the pendulum velocity. This effect can be used to find compromise beetween vibration absorption and energy harvesting. Note, that application of SMA spring reduces non-trivial solution from right side (from the higher frequency).

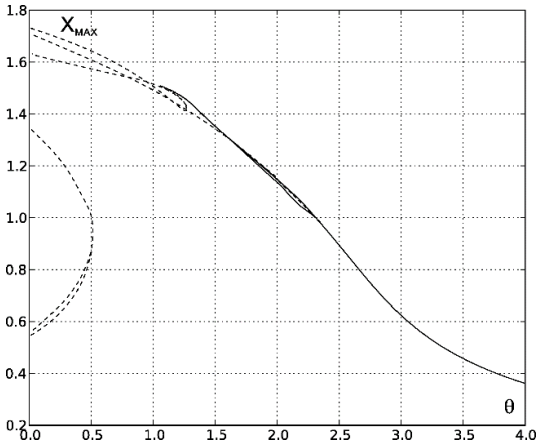

Fig. 7. Influence of temparature on amplitude of the oscillator, for ϑ=0.7 (absorption region), β_1=0.6, β_2=0.9

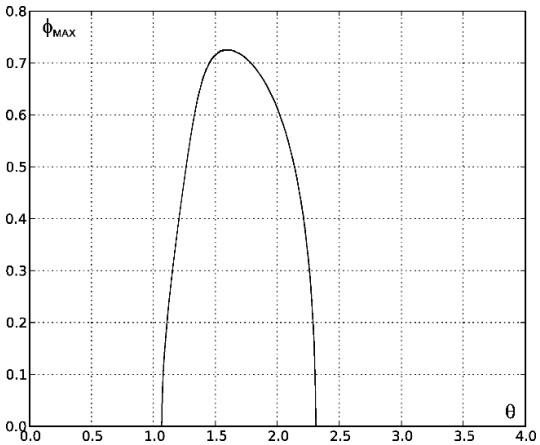

Fig. 8. Influence of temparature on amplitude of the pendulum, for ϑ=0.7(absorption region), β_1=0.6, β_2=0.9

The effect of temperature (parameter θ) on the oscillator and pendulum amplitudes has been investigated (Figs. 7 and 8). The stable solutions are observed for $\theta > 1$.The pendulum executes motions for range of θ from 1.1 to 2.3.

3.2. Influence of SMA spring on energy harvesting

The energy harvesting level strongly depends on the construction of the harvester device. Usually, these devices are mounted in the pendulum suspension. This construction is very difficult to control by applied the pendulum's damping. Therefore, this paper proposes allternative method of control by SMA element mounted in the suspension. In this section influence of SMA spring on energy harvesting is studied in detail.

Firstly, the influence of temperature on recovery voltage is analysed (Fig. 9). The resonance region is clearly visible, nerly frequency ϑ=0.7-0.8. This result agrees with the resonance curves, presented in Figs. 7 and 8. The maximal recovered voltage was about 6mV. Of course, the values depend on electrical parameters of harvester (for analysis taken: R_{int}=55Ω, R_{load}=140Ω, δ=7.752Vs/m, ρ=0.01m). The range of temperature in which voltage is recovered equals θ=0.5 to θ=2.3, but the best is located for θ=1.5 to θ=2.

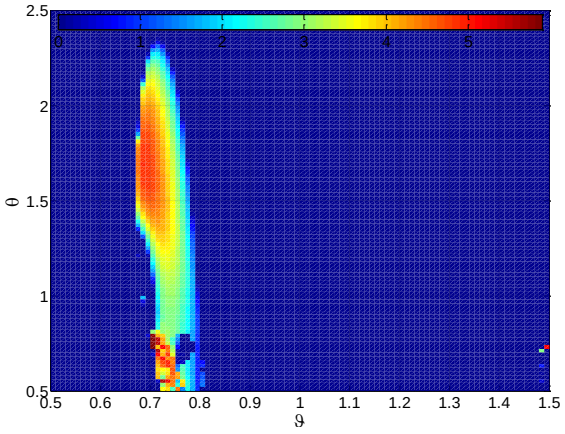

Fig. 9. The 3D plot: temperature vs. frequency vs. voltage, for β_1=0.6, β_2=0.9

Next, parameters describing material of which the SMA spring is made (β_1, β_2) are analyzed. The parameter β_1 depends of natural frequency of the oscillator and static displacement, also (see eq. (12)). While, parameter β_2 comes from β_1 and depends on austenite and martesite temperature phases.

The relationship beetwen temperature θ and parameter β1 versus voltage harvesting in Fig. 10 is shown as 3D plot. This result was obtained near the absorption region (for frequency ϑ=0.7). The maximal recoverd voltage equals 6mV, and can be recoverd for θ=1.4-2.4 in range of β_1 larger then 0.4. Additionally, the small regions in which 6mV recovered can be observed for lower temperature (martensite phases temperature). However, these regions are narrow.

The second parameter β_2 is much more difficult to choose. The region with high level of energy recovery (12mV) is very narrow (Fig. 11). Moreover, this parameter depends on β_1 (eq. (12)). The obtained results from both diagrams show that properly choosen parameters can incrase recovered voltage.

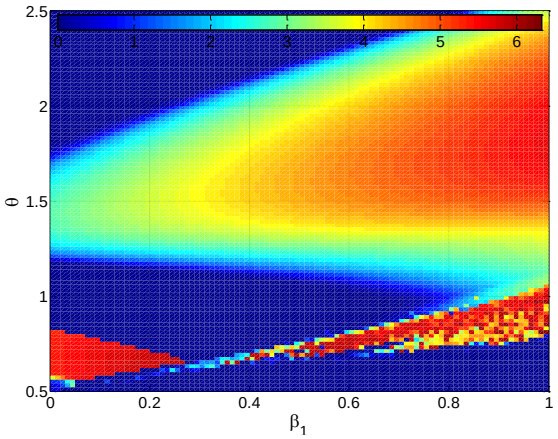

Fig. 10. The 3D plot: temperature vs. parameter β_1 vs. voltage, for β_2=0.9

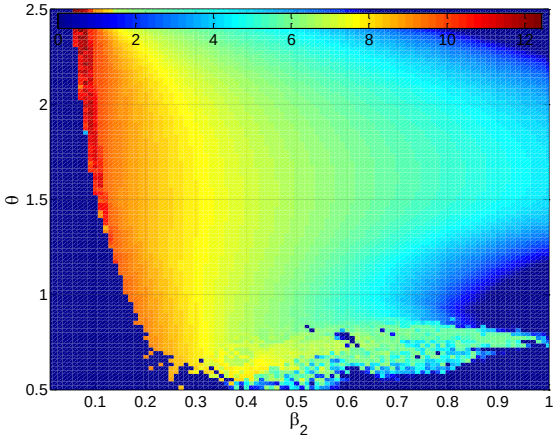

Fig. 11. The 3D plot: temperature vs. parameter β_2 vs. voltage, for β_1=0.6, ϑ=0.7

The influences of total damping (mechanical and electrical) on energy harvesting is shown in Fig. 12. The critical damping has practically similar value , equals about 0.07-0.08. Note, that for the pendulum damping close to zero and temperature θ=0.5-0.9, the recovered energy is highest and equals about 12mV.

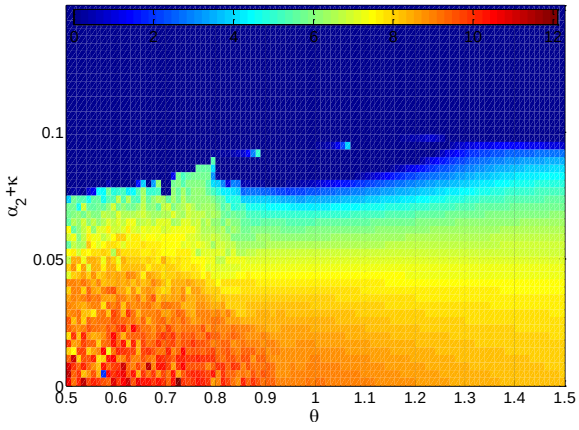

Fig. 12. The 3D plot: temperature vs. parameter β_2 vs. voltage, for β_1=0.6, ϑ=0.7

All the above results presented in this section have been done for fixed initial conditions: $X = \dot{X} = \dot{\varphi} = 0$ and $\varphi = 0.1$.

DOI 10.1515/ama-2015-0026

The obtained results show, that properly confiruration of SMA parameters (ϑ, β_1 and β_2) can increase energy recovery. However, the application of SMA spring in dynamic absorbers should be detailed checked by numerical studies.

4. CONCLUSIONS AND FINAL REMARKS

This paper presents an autoparametric system with added harvester device mounted in the pendulum pivot. This conception of rotatory pendulum harvester, practically prevents control of motion by the pendulum's damping. Therefore, the other solution based on SMA spring mounted in suspension is proposed.

The conception was analyzed in two aspects. Firstly the influenece of SMA spring on absorption region was studied. Next, the problem of energy harvesting under SMA spring was analyzed. The SMA spring significantly reduce the absorption effect (but not eliminate it), what is problem for dynamic absorbers. The frequency response curves for SMA spring are bents in the right side. For, some parameters the solution changes from stable into unstable motion and a new bifurcation point can appears.

The SMA spring significantly influence on energy recovery. Change in the SMA springs parameters the increase or decrease enegy harvesting is possible. The best range of the temperature for EH equals θ=1.5-2.The properly choose of SMA parameters can incraeases recovered voltage up to 12mV.

The next step will be experimental verification of obtained results and appied control algorithm to highest energy recovery.

REFERENCES

1. **Cartmell M. P., Lawson J.** (1994), Performance enhancement of an autoparametric vibration absorber by means of computer control, *Journal of Sound and Vibration*, 17(2), 173–195.
2. **Doedel E., Oldeman B., Champneys A., Dercole F., Fairgrieve, Kuznetsov Y., Paenroth R., Sandstede B., Wang X., Zhang C.** (2011), *AUTO-07P: Continuation and bifurcation software for ordinary differential equations*, Concordia University (Montreal, Canada, 2011).
3. **Falk F.** (1980), Model free energy mechanics and thermodynamics of shape memory alloys, *Acta Metallurgica*, 28, 1773–1780.
4. **Gu L., Livermore C.** 2010), *Pendulum-Driven Passive Self-Tuning Energy Harvester for Rotating Applications*, Presented at Power MEMS Workshop, Leuven, Belgium.
5. **Janocha H.** (Ed.), (2007*), Adaptronics and Smart Structures*, *Springer-Verlag*, Berlin Heidelberg New York.
6. **Kaynia A. M., Veneziano D., Biggs J. M.** (1981), Seismic effectiveness of tuned mass dampers, *Journal of Structural Engineering*, 107(8), 1465–1484.
7. **Kecik K.** (2015), Dynamics and control of an autoparametric system, *International Journal of Non-linear Mechanics*, 70, 63-72.
8. **Kecik K., Borowiec M.** (2013), An autoparametric energy harvester, *Th Europen Physical Journal Special Topics*, 222(7), 1597–1605.
9. **Kecik K., Mitura A., Sado D., Warminski J.** (2014), Magnetorheological damping and semi-active control of an autoparametric vibration absorber, *Meccanica*, 49(8), 1887-1900.
10. **Lacarbonara W.** (2012), Nonlinear dynamics enabled systems design and control, *Journal of Physics: Conference Series*, 382**,** ID 012001, 1-9.
11. **Liao G. J., Gong X. L., Kang C. J., Xuan S. H. (**2011), The design of an active–adaptive tuned vibration absorber based on magnetorheological elastomer and its vibration attenuation performance, *Smart Material Structure*, 20, ID 075015, 1-11.
12. **Ma T. W., Zhang H., Xu N. S.** 2012), A novel parametrically excited non-linear energy harvester, *Mechanical Systems and Signal Processing*, 28, 323–332.
13. **Oueini S. S., Nayfeh A. H., Golnaraghi M. F. A.** (1997), A theoretical and experimental implementation of a control method based on saturation, *Nonlinear Dynamics*, 13, 189-202.
14. **Regis V.** (2010), *Tuning Methodology of Nonlinear Vibration Absorbers Coupled to Nonlinear Mechanical Systems*, PhD Thesis.
15. **Sladek J. R., Klingner R. E.** (1983), Effect of tuned mass dampers on seismic response, *Journal of the Structural Division*, 109, 2004–2009.
16. **Soto-Brito R., Ruiz S. E.** (1999), Influence of ground motion intensity on the effectiveness of tuned mass dampers, *Earthquake Engineering and Structural Dynamics*, 28, 1255–1271.
17. **Vazquez-Gonzalezal B, Silva-Navarro G.** (2008), Evaluation of the autoparametric pendulum vibration absorber for a Duffing system, *Shock and Vibration*, 15, 355–368.
18. **Warminski J., Kecik K.** (2006), Autoparametric vibrations of a nonlinear system with pendulum. *Mathematical Problems in Engineerin*g, 1-19.
19. **Warminski J., Kecik K.** (2009), Instabilities in the main parametric resonance area of mechanical system with a pendulum,*Journal of Sound Vibration*, 332, 612-628.
20. **Wiercigroch M**., **Najdecka A., Vaziri V.** (2011), Nonlinear Dynamics of Pendulums System for Energy Harvestin, Vibration Problems ICOVP 2011, *Book Series: Springer Proceedings in Physics*, Edited by: Naprstek J., Horacek J., Okrouhlik M., Marvalova B., Verhulst F., Sawicki J.T., 139, 35-42.
21. **Xu X., Pavlovskaia E. E., Wiercigroch M., Romeo F., Lenci S.** (2007), Dynamic interactions between parametric pendulum and electro-dynamical shaker, *ZAMM Journal of applied mathematics and mechanics*, Zeitschrift für angewandte Mathematik und Mechanik, 87(2), 172–186.

Acknowledgments: This work was financially supported under the project of National Science Centre according to decision no. DEC-2013/11/D/ST8/03311.

NUMERICAL MODELLING OF HUMID AIR FLOW AROUND A POROUS BODY

Aneta BOHOJŁO-WIŚNIEWSKA*

*Division of Heat Engineering and Refrigeration, Białystok University of Technology, Białystok

a.bohojlo@pb.edu.pl

received 27 November 2014, revised 23 October 2015, accepted 26 October 2015

Summary: This paper presents an example of humid air flow around a single head of Chinese cabbage under conditions of complex heat transfer. This kind of numerical simulation allows us to create a heat and humidity transfer model between the Chinese cabbage and the flowing humid air. The calculations utilize the heat transfer model in porous medium, which includes the temperature difference between the solid (vegetable tissue) and fluid (air) phases of the porous medium. Modelling and calculations were performed in ANSYS Fluent 14.5 software.

Key words: Numerical Modelling, Heat Transfer, Air Flow, Mass Transfer, Chinese Cabbage

1. INTRODUCTION

Fresh vegetables and fruit are living tissues, which after being harvested undergo a number of biological processes. Most important of these – directly influencing the nutritional and commercial value – are: respiration, ripening, transpiration. The processes are greatly influenced by temperature and external air humidity. It is therefore essential for the product to be stored in optimal conditions - low temperature and adequate humidity - in order to minimize the product loss. Achieving such conditions in cold stores is possible thanks to cooling units with forced air circulation. Because of the number and complexity of the physical phenomena taking place in agricultural produce store chamber, this issue is a new and difficult field for Computational Fluid Dynamics (CFD).

Most of the publications concerning the cold storage, and the experimental data gathered in this field, suggest that air parameters in storage chambers are characterized by significant nonuniformity, both in the empty areas, as well as in areas occupied by storage containers (Moureh et at., 2009, 2009a, 2009b; Tapsoba et at., 2007; Ben Amara et at., 2004; Delele et at., 2009a, 2009b; Hoang et at., 2000; Than et at., 2008). This means that there are regions in the bed of vegetables where the temperature is too high, which causes the produce to dry, and areas where the temperature is too low, resulting in cold damages. Therefore there is a need to focus the research on finding a solution, which would eliminate, or at least significantly limit, this problem. Computational analysis done on an experimentally verified mathematical and computational model may serve as a tool for assessing the air parameters in cold storage, as well as the state of fruit and vegetable stored there, without the need to conduct time-consuming, expensive and complicated experimental analysis. It will be a relatively cheap and flexible tool for solving this problem.

Because of complex internal geometry of the vegetables bed in a cold store, and the scale difference between the storage chamber and a single vegetable, the most important element of the air flow model in a cold store is treating bed of vegetables as a porous medium. Direct modelling, i.e. modelling which includes the shape of vegetable is impossible in such a large space. The vegetables bed can be homogenized in two ways: taking into consideration the temperature difference between vegetables and flowing air, or disregarding it. In recent years there is a tendency in professional publications to include the temperature difference between the solid phase (vegetable) and the liquid phase (air) of the porous medium (vegetable load), because such a model of heat transfer better expresses the processes taking place in the load. The consequence of adopting this model of heat transfer is the need to determine the heat transfer coefficient on the boundary between solid and liquid phase of the porous medium.

The value of heat transfer coefficient depends on a number of factors, most important of which are: vegetable shape, load arrangement, pore velocity and local turbulence intensity (Kondjovan et al., 2006). Therefore it is a function of location within the load. Experimental determination of the heat transfer coefficient spatial distribution is very difficult, if not impossible. In this situation the Computational Fluid Dynamics (CFD) might prove useful. It allows us to model a small bed of vegetables directly, that is taking into consideration the shape of vegetables. This type of modelling does not require the knowledge of the heat transfer coefficients, provided that the model includes the heat conduction within the vegetables. The direct modelling allows us to determine surface heat flux between the vegetables and the flowing air, and consequently to determine the heat transfer coefficients at any point of the load treated as a porous medium.

The aim of this work is to present the preliminary stage of direct modelling on the example of humid air flow around a single element of the vegetable load (a head of Chinese cabbage) under conditions of complex heat transfer (i.e. including the heat conduction within the product). This will allow us to create a heat and humidity transfer model between the Chinese cabbage and the flowing humid air. Modelling and calculations were performed in ANSYS Fluent 14.5 software.

DOI 10.1515/ama-2015-0027

2. HEAT AND MASS TRANSFER MODEL BETWEEN A HEAD OF CHINESE CABBAGE AND THE FLOWING HUMID AIR

The flow of air around a single head of Chinese cabbage will be analysed in a test tunnel because in the said tunnel, the experiments of the heat and mass transfer between the suspended cabbage and the stream of humid air will be conducted. The geometric model of the cabbage and the tunnel is presented in Fig. 1.

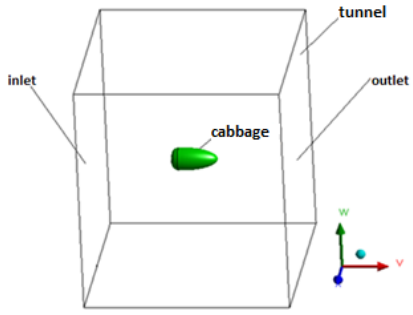

Fig. 1. Geometric model of the tunnel with a single element of the Chinese cabbage load, and the calculation domain

The actual shape of the Chinese cabbage (Fig. 2) and its internal structure are very complex.

Fig. 2. Chinese cabbage head

Fig. 3. Cross-section of a Chinese cabbage

Fig. 3 presents the cross-section of a Chinese cabbage. The photographs presented show that only 2 or 3 external leaves are slightly open at the top of a head. The rest of the leaves form a separate, porous structure, which is almost completely isolated from the surrounding air. Therefore in the proposed model we treat the inside of a Chinese cabbage as porous medium and assume that the airflow within the porous medium has a velocity close to zero, i.e. we assumed a very high resistance of the medium. The calculations do not take into account the porous structure of vegetable tissue (cabbage leaves).

The domain of solution is divided into subdomain occupied by the air flowing around the cabbage head (tunnel) and the subdomain of cabbage itself, modelled as a porous medium. The calculations utilize the heat transfer model in porous medium, which includes the temperature difference between the solid (vegetable tissue) and fluid (air) phases of the medium.

The porosity of the medium is defined as the ratio of the pore volume V_p to the total volume of the porous medium V (Strzelecki et at., 2008):

$$\varepsilon_m = \frac{V_p}{V} = 1 - \frac{\rho_p}{\rho_s}, \qquad 0 \le \varepsilon_m \le 1. \tag{1}$$

In the equation (1) ρ_p is the apparent density of the porous medium, and ρ_s is the true density of a solid (cabbage leaf). Porous medium is a fictitious continuum, with flow resistance equal to the resistance of a real obstacle. This resistance is included in the balance equation by adding an additional source term to the momentum equation (ANSYS FLUENT 14.5):

$$S_i = -\left(\sum_{j=1}^{3} D_{ij}\mu v_j + \sum_{j=1}^{3} C_{ij}\frac{1}{2}\rho|v|\, v_j\right), \tag{2}$$

where: i, j is the spatial direction (x, y, z), D_{ij} and C_{ij} are the resistance coefficient matrices, viscous and inertial respectively, μ – is the viscosity of fluid phase of the porous medium, including the turbulent viscosity, v_j – denotes the respective velocity component. In the model proposed, because of the Chinese cabbage internal structure, the convection within the medium is negligible. Therefore we assumed a very high resistance value, which almost eliminates motion of the medium.

The operating medium in the tunnel subdomain was humid air, treated as a non-compressible ideal gas, being a mixture of oxygen (O_2), nitrogen (N_2) and water vapour (H_2O) (species transport model without chemical reactions). The thermo-physical properties of O_2, N_2 and H_2O are dependent on the temperature according to the 4th order polynomial, according to ANSYS Fluent theory Guide 14.5. The cabbage subdomain was treated as a porous medium, where the solid material is the cabbage leaf tissue, whilst the fluid phase is the humid air. Within the porous medium we adopted a heat transfer model which includes the temperature difference between solid and fluid phases.

The flow in the computational domain is described by the continuity equation:

$$\frac{\partial(\varepsilon_m\rho_m)}{\partial t} + \nabla\cdot(\varepsilon\rho_m\vec{v}_m) = 0, \tag{3}$$

where: ε_m – is the porosity (for the *tunnel* subdomain ε_m= 1), ρ_m is the mixture density, v_m – its velocity, and the momentum equation which includes the natural convection term:

$$\frac{\partial(\varepsilon_m\rho_m\vec{v}_m)}{\partial t} + \nabla\cdot(\varepsilon_m\rho_m\vec{v}_m\vec{v}_m) = (\rho_m - \rho_0)g - \varepsilon_m\nabla p + \nabla\cdot \left(\varepsilon_m\mu_m(\nabla\vec{v}_m + \nabla\vec{v}_m^T)\right) + S, \tag{4}$$

where: p is the pressure, ρ_0 – reference density, and S – an additional source term resulting from the use of porous media model.

Because of the use of species transport model for describing the humid air flow, the system of equations is supplemented with two transport equations for oxygen and water vapour of the form:

$$\frac{\partial}{\partial t}(\rho Y_i) + \nabla\cdot(\rho\,\vec{v}_m Y_i) = -\nabla\cdot\vec{J}_i + S_i, \tag{5}$$

where i-denotes the species, Y_i– is the „ i" species mass fraction, S_i –user defined source of „ i" species (Nitrogen mass fraction is defined as the supplement to 1). J_i is the diffusion flux

of species „i" due to temperature and concentration gradients. In turbulent flow it is expressed as:

$$\vec{J}_i = -\left(\rho D_{i,m} + \frac{\mu_t}{Sc_t}\right) \nabla Y_i - D_{T,i} \frac{\nabla T}{T}, \quad (6)$$

where: $Sc_t = \mu_t/\rho D_t$ is the effective Schmidt number for turbulent flow (μ_t – turbulent viscosity, D_t – the effective mass diffusion coefficient due to turbulence), $D_{i,m}$ – is mass diffusion coefficient for species „i", $D_{T,i}$ – is the thermal diffusion coefficient, T – temperature.

The species transport model allowed us to include the moisture source due to transpiration from the inner leaves of the cabbage (Si source in (5) equation for water vapour), as well as its diffusion.

Within the cabbage subdomain we will therefore solve two energy equations – one for air (7) and one for cabbage leaves (8):

$$\frac{\partial}{\partial t}(\varepsilon_m \rho_m E_m) + \nabla \cdot (\vec{v}_m(\rho_m E_m + p)) = \nabla \cdot (k_m \nabla T_m) - \sum_i h_j J_i + (\bar{\bar{\tau}}_{eff} \cdot \vec{v}_m) + S_m^h + h_{fs} A_{fs}(T_f - T_s), \quad (7)$$

$$\frac{\partial}{\partial t}((1-\varepsilon_m)\rho_s E_s) = \nabla \cdot ((1-\varepsilon_m) k_s \nabla T_s) + S_s^h + h_{fs} A_{fs}(T_s - T_f), \quad (8)$$

where: $E_m = h_m + p/\rho_m + v_m^2/2$ is the fluid phase (humid air) total energy and E_s – solid phase (Chinese cabbage leaves) total energy; T_m and T_s – the temperature of humid air and cabbage leaves, respectively; k_m is the fluid phase thermal conductivity (including the turbulent contribution); ρ_s, k_s – density and conductivity of the solid phase (leaves); h_{fs} – the heat transfer coefficient for the leaves-humid air interface; A_{fs} – is the interfacial area density, that is the ratio of the contact area between leaves and air to the volume of the porous medium (cabbage head), S_m^h, S_s^h – fluid and solid enthalpy source terms, respectively.

The heat transfer coefficient for the interface between vegetable tissue and the air within the cabbage was determined from the correlation for natural convection (Wiśniewski and Wiśniewski, 2000):

$$Nu = 0.13 Ra^{1/3}, \quad (9)$$

where the Nusselt number is defined as:

$$Nu = \frac{hl}{k}, \quad (10)$$

l – the length scale, k – heat conductivity, h – convective heat transfer coefficient.

Rayleigh number is given as:

$$Ra = GrPr. \quad (11)$$

Grashof number is defined as:

$$Gr = \frac{g\beta(T_s - T_\infty)l^3}{\nu^2}, \quad (12)$$

where: g – acceleration due to gravity, β – volumetric thermal expansion coefficient, ν – kinematic viscosity, T_s – surface temperature, T_∞ – bulk temperature.

Prandtl number is defined as:

$$Pr = c_p \frac{\mu}{k}, \quad (13)$$

where: c_p – specific heat, μ – dynamic viscosity.

The proposed model includes heat processes taking place in the vegetable, biological process – the heat of respiration, being the positive source in equation (8) and the heat of transpiration being the negative source in equation (7), due to evaporative cooling. In the water vapour transport equation (6) we include the positive source, due to transpiration from the surface of the cabbage leaves. They were placed in cabbage subdomain treated as a porous medium. In the presented model both heat and mass sources are treated as being constant.

In the paper the model SST $k-\omega$ was used. SST model utilizes the advantages of both models: $k-\varepsilon$ and $k-\omega$. The use of a k-ω model in the inner parts of the boundary layer makes the model directly usable all the way down to the wall through the viscous sub-layer, therefore the SST $k-\omega$ model can be used as a Low-Re turbulence model without any extra damping functions. The SST formulation also switches to a k-ε behavior in the free-stream and thereby avoids the common $k-\omega$ problem that the model is too sensitive to the free-stream turbulence properties.

The model is to be applied to the study of phenomena on the border of the bed – empty space in the cold storage then it is to be extended and used for modeling the whole cold storage. For this type of calculation model SST $k-\omega$ works better than other models (Delele et at., 2009a, 2009b, 2012; Norton et at., 2007).

3. COMPUTATIONAL MODEL

The grid was created in ANSYS Meshing 14.5 software. It consists of 2 126 006 control volumes, including: 10896 tetrahedrons, 105834 wedges, 9794 pyramids, 1927387 hexahedrons, 72095 polyhedrons. The grid was created using the cutcell method (Fig. 4).

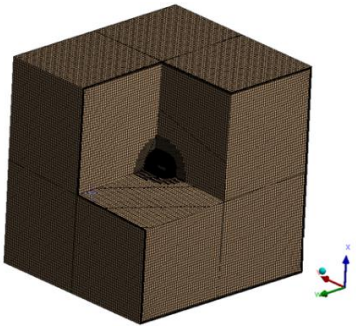

Fig. 4. Computational grid

Tab. 1. Volume, density and porosity of cabbage heads

	Mass	Volume	Volume of the leaves	Apparent density	Density of the leaves	Porosity
	[kg]	[l]	[l]	[kg/m³]	[kg/m³]	
Cabbage #1	0.86483	1.76265	1.12183	490.6419	770.91	0.363555
Cabbage #2	0.7495	1.29366	0.861	579.364	870.4994	0.334446
Cabbage #3	1.1135	1.997	1.19945	557.5864	928.3422	0.399374
Cabbage #4	0.6365	1.465	0.781836	434.471	814.1094	0.466324
			Mean values	**515.5**	**846**	**0.391**

The stability and precision of calculations are strongly affected by the computational grid quality. Cutcell is described by orthogo-

DOI 10.1515/ama-2015-0027

nal quality which ranges from 0 to 1, where values close to 0 correspond to low quality. Our minimum orthogonal quality was 0.296257.

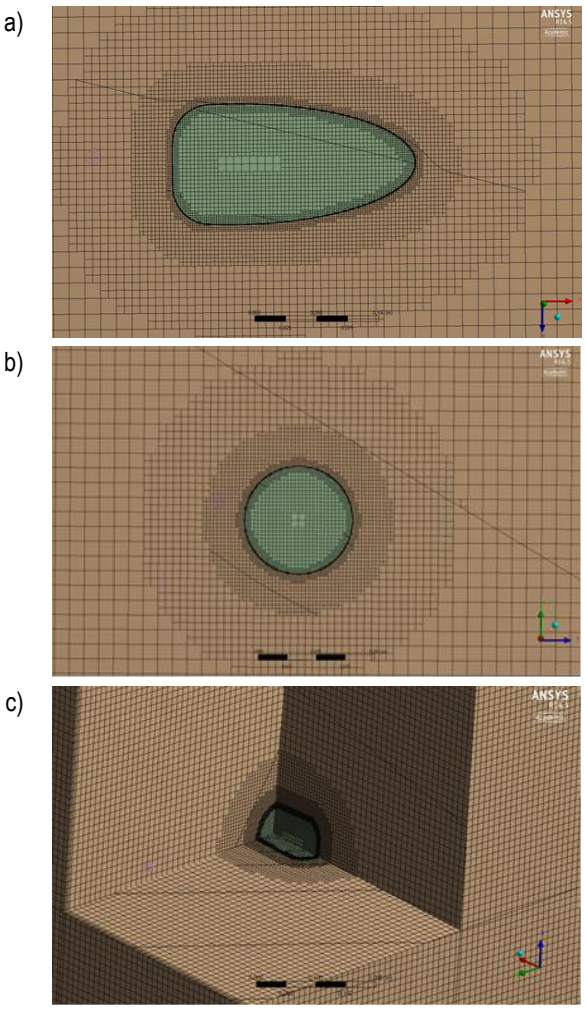

Fig. 5. The meshing of computational model: a) The grid in the symmetry plane of the *cabbage* domain, b) The grid is the cross – section of the *cabbage* domain, c) The grid of the *tunnel* and *cabbage* subdomains

Tab. 2. The area of the cabbage leaves (the interface between leaves and air)

The total area of the leaves [m²]			
Leaves of cabbage #1		0.95636	
Leaves of cabbage #4		0.76182	
$interfacial\ area\ density = \frac{total\ area\ of\ the\ leaves}{volume\ of\ the\ cabbage\ head}$ [m²/m³]			
Cabbage #1	542.5694	Mean value	531.293
Cabbage #4	520.0169		

Some of the cabbage physical properties were taken from various publications, others were determined in experiments. Tab. 1 presents the volume, density and porosity determined experimentally for 4 different Chinese cabbage heads. The average of apparent density, the density of vegetable leaves and porosity were used as input data in numerical calculations. Specialized publications do not contain data for interfacial area for Chinese cabbage (Sadik et at., 2011, Uzokwe et at., 2012, Olfati et at., 2010), so the measurements were performed with a polar planimeter for two heads of Chinese cabbage. The calculations of the average interfacial area density inside the cabbage head is presented in the Tab. 2.

- The following data were used as the input data in the calculations:
- Inlet mass flow rate 3.938 kg/s (maximum mass flow measured experimentally in the channel in which in the future the experiment is planned), relative humidity 80%, air temperature 0.5 °C,
- Heat of respiration for Chinese cabbage at 0.5°C – 3590 kJ/ton/24h (Murata et al. 1992),
- Daily mass loss caused by transpiration, assumed as for white cabbage (no data available for Chinese cabbage) 0.233 % (Watkins and Nock, 2012),
- Thermophysical properties of Chinese cabbage at 0.5°C and relative humidity of 80%:
  - The density of the tissue 846 kg/m³ (Tab. 1),
  - Density of the entire cabbage head (apparent density) 515,5 kg/m³ (Tab. 1),
  - Moisture mass fraction for cabbage m=0.92 (Niesteruk, 1996),
  - Specific heat c_p= 1402+2785·m, c_p=3964.2 J/(kg·K) (Niesteruk, 1996),
  - Thermal conductivity k=0.8 W/(m·K) (Niesteruk, 1996),
  - Porosity ε=0.391 (Tab.1),
  - The mass loss of the load treated as a volume water vapour source: 1.39 x10^{-5} kg/m³·s ,
  - The heat of respiration, treated as a volume heat source: 21.42 W/m³,
  - The volume of the cabbage was 1,12·10^{-3} m³,
  - Heat transfer coefficient 1.98 W/(m²·K),
  - Interfacial area density 531,293 1/m (Tab. 2).

4. RESULTS OF CALCULATIONS

The calculations were performed on a PC computer with Intel Xeon 3,47 GHz CPU, 24 GB RAM with ANSYS Fluent 14.5 code and the Couple algorithm. The parallel environment with 4 parallel processes was used and calculations were done in double precision. The calculations lasted around 1800 iterations. The residual convergence was presented in Fig. 6.

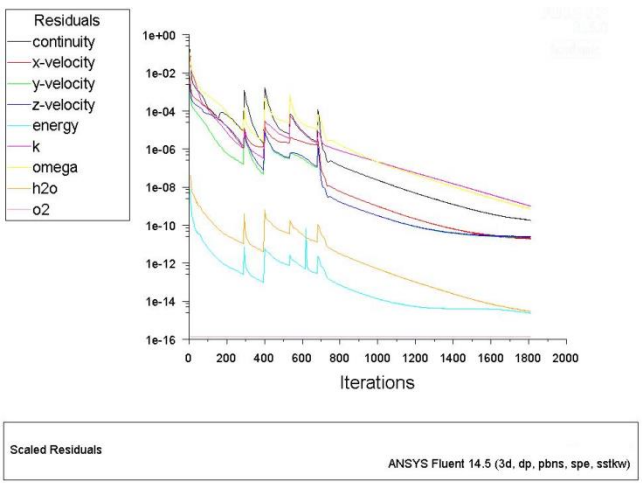

Fig. 6. Residual convergence

The result of calculations were presented in graphic form in Figs. 7-10. Fig. 7 shows the velocity distribution in symmetry plane of the tunnel. The maximum value was 3.84 m/s. A characteristic wake behind the cabbage can be clearly seen in the picture – it was the area of the lowest velocity. Inside the cabbage the velocity was almost equal to zero. The distribution of pressure was presented in the Fig. 8. Around leading edge of the cabbage there is a small area of higher pressure – around 1.5 Pa more than in the trailing area. In the area around the poles of the cabbage the pressure is at its lowest – approx. – 10 Pa. Inside the cabbage the pressure is equal to 0.36 Pa.

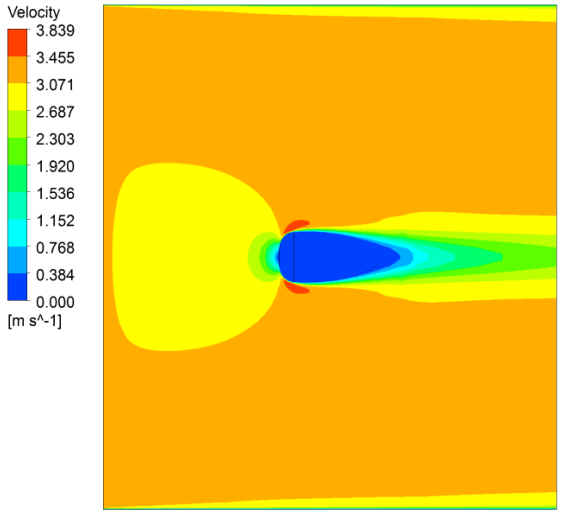

Fig. 7. Velocity distribution in the symmetry plane of the *tunnel*

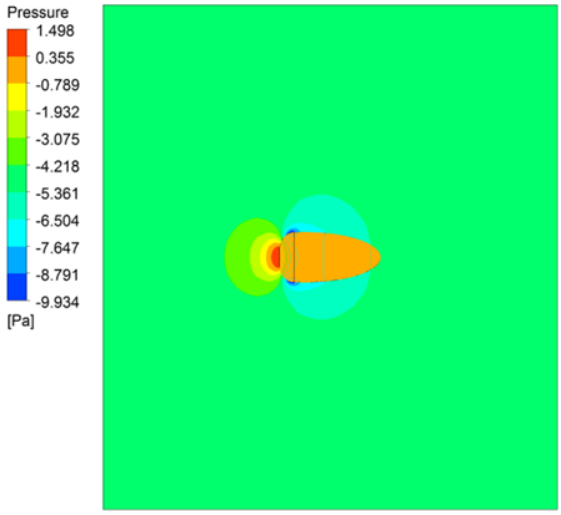

Fig. 8. Pressure distribution in the symmetry plane of the *tunnel*

The temperature contours in the symmetry plane of the tunnel are given in Fig. 9. The distributions of temperature in the tunnel and in the air inside the cabbage are presented in Fig. 9a, whilst in the tunnel and inside the vegetable tissue- in Fig. 9b. Each plot uses a separate temperature scale in order to present the relations in more detail. The highest temperature was observed in the solid phase (leaf tissue) of the cabbage of the porous medium – 0.536°C. The lowest temperature detected was 0.5°C – it was the temperature on the inflow and in the tunnel itself. Both figures clearly show the rise of temperature in areas near the Chinese cabbage head – which is caused by the heat source (heat of respiration). The total heat of respiration for the entire volume of the Chinese cabbage was 86.364 J/h.

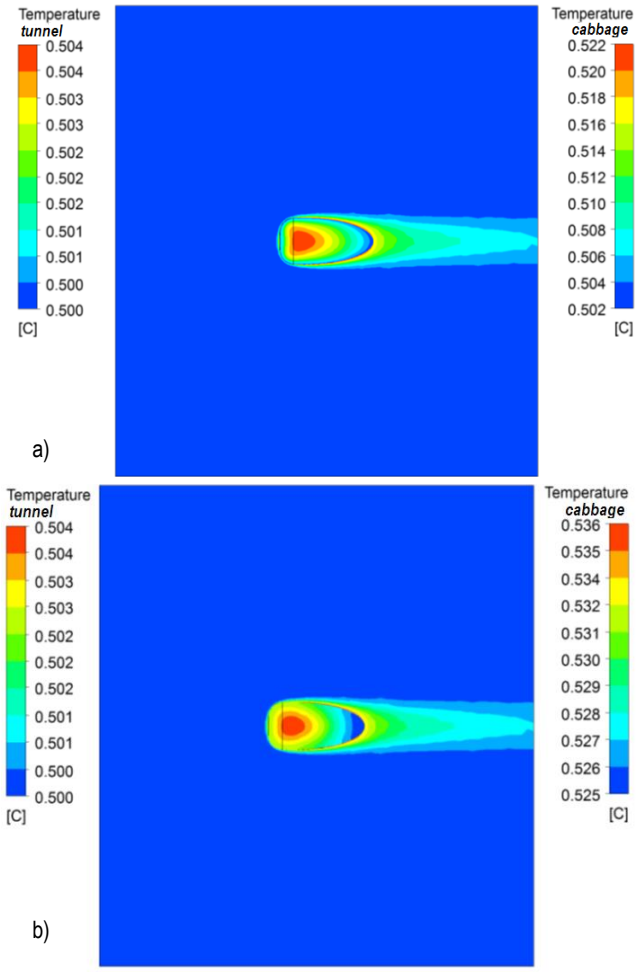

Fig. 9. Temperature distribution in the symmetry plane
a) in the *tunnel* and in the fluid phase (air) of a *cabbage*,
b) in the *tunnel* and in the solid phase (leaves of the cabbage)

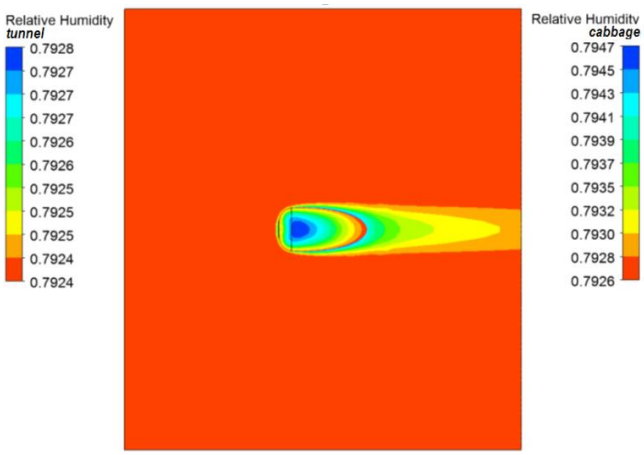

Fig. 10. Relative humidity distribution in *tunnel* and *cabbage* subdomains

Fig. 10 presents the distributions of relative humidity in the symmetry plane. The relative humidity distribution was presented in two different scales – one for air in the tunnel and one for air in the porous medium. In the picture we can see that the relative humidity rises near the cabbage; it is caused by the water vapour

DOI 10.1515/ama-2015-0027

mass transfer from the cabbage in the transpiration process. The water vapour seen on the outer surface of the cabbage is a result of transfer within the product. The water vapour emitted by the Chinese cabbage head was equal to 0.056 g/h.

5. CONCLUSIONS

In the paper preliminary computational model is presented which includes the temperature difference between the solid (vegetable tissue) and the fluid (air) phases of the porous medium representing the Chinese cabbage head. This model is able to calculate velocity, pressure, relative humidity and surface and inner temperature evolution of the vegetable. The temperature and relative humidity differences between the air and the cabbage are very small. Such differences are very difficult to measure in the experiment neither for one nor for a few cabbage heads. Experimentally it is possible to measure such small differences only in larger beds. Unfortunately for such a large space it is impossible to perform numerical computations by direct modelling approach. In the submitted computational model we are able to verify by experiment only velocity of the air.

In the future research it is planned to make the calculations on a larger number of heads of the Chinese cabbage in the test channel . In addition, in the computation model taking into account the intensity of the processes of evaporation and respiration dependent on the temperature and humidity by adding the UDF (User Defined Function) is planned. Unfortunately, the data on the Chinese cabbage are either difficult to reach or do not exist. They are incomplete, ambiguous and therefore some values (porosity of the cabbage head, interfacial area density, total area of the cabbage leaves) were determined experimentally. These processes require further experimental research.

The numerical calculations presented in the paper allowed us to test the computational model and helped to determine the important factors in the analysed problem. Further stages of the analysis will lead us to determine the spatial distribution of the heat transfer coefficient on the outer surface of the vegetable as a result of calculations of heat surface flux.

REFERENCES

1. **ANSYS FLUENT** Theory Guide.
2. **Ben Amara S., Laguerre O., Flick D.** (2004), Experimantal study of convective heat transfer during cooling with low air velocity in a stack of objects, *International Journal of Thermal Science*, 43, 1213-1221.
3. **Delele M. A., Vorstermans B., Creemers P., Tsige A. A., Tijskens E., Schenk A., Opara U.L., Nicolaï B.M., Verboven P.** (2012), CFD model development and validation of a thermo nebulisation fungicide fogging system for postharvest storage of fruit, *Journal of Food Engineering*, 108, 59-68.
4. **Delele M. A., Schenk A., Ramon H., Nicolai B. M., Verboven P.** (2009b), Evaluation of a chicory root cold store humidification system using computational fluid dynamics, *Journal of Food Engineering*, 94, 110-121.
5. **Delele M. A., Schenk A., Tijskens E., Ramon H., Nicolai B. M., Verboven P.** (2009a), Optimization of the humidification of cold stores by pressurized water atomizers based on a multiscale CFD model, *Journal of Food Engineering*, 91, 228-239.
6. **Hoang M. L., Verboven P., De Baerdemaeker J., Nicolai,** (2000), Analysis of the air flow in a cold store by means of computational fluid dynamics, *International Journal of Refrigeration*, 23, 127-140.
7. **Kondjoyan A.** (2006), A review on surface heat and mass transfer coefficients during air chilling and storage of food products, *International Journal of Refrigeration*, 29, 863-875.
8. **Moureh J., Tapsoba M., Flick D.** (2009a), Airflow in a slot-ventilated enclosure partially filled with porous boxes: Part I – measurements and simulations in the clear region, *Computers & Fluids*, 38, 194-205.
9. **Moureh J., Tapsoba S., Derens E., Flick D.** (2009), Air velocity characteristics within vented pallets loaded in a refrigerated vehicle with and without air ducts, *International Journal of Refrigeration*, 32, 220-234.
10. **Moureh J., Tapsoba S., Flick D.** (2009b), Airflow in a slot-ventilated enclosure partially filled with porous boxes: Part II - measurements and simulations within porous boxes, *Computers & Fluids*, 206-220.
11. **Murata S., Miyauchi K., Wang Y.** (1992), *Respiration Rate of Thirteen Kinds of Japanese Fresh Vegetables***,** Laboratory of Agricultural Process Engineering, Faculty of Agriculture, Kyushu University 46 - 05, Fukuoka 812, Japan.
12. **Niesteruk R.** (1996), *Thermophysical properties of food*, Part 1 (in Polish), Wydawnictwo Politechniki Białostockiej.
13. **Norton T., Sun D., Grant J., Fallon R., Dodd V.** (2007), Applications of computational fluid dynamics (CFD) in the modelling and design of ventilation systems in the agricultural industry: A review, *Bioresource Technology*, 98, 2386–2414.
14. **Olfati J.A., Peyvast G. , Shabani H., Nosratie-Rad Z.** (2010), An Estimation of Individual Leaf Area in Cabbage and Broccoli Using Non-destructive Methods, *Journal Of Agricultural Science And Technology*, 12, 627-632.
15. **Sadik S. K., AL-Taweel A. A., Dhyeab N. S.** (2011), New Computer Program for Estimating Leaf Area of Several Vegetable Crops, *American-Eurasian Journal of Sustainable Agriculture*, 5(2), 304-309.
16. **Strzelecki T., Kostecki S., Żak S.** (2008), *Modeling Flow Through Porous Media* (in Polish), Dolnośląskie Wydawnictwo Edukacyjne.
17. **Tapsoba M., Moureh J., Flick D.** (2007), Airflow patterns inside slotted obstacles in a ventilated enclosure, *Computers & Fluids*, 36, 935-948.
18. **Than V. T., Vranken E., Berckmans D.** (2008), Data-based mechanistic modeling of three-dimensional temperature distribution in ventilated rooms filled with biological material, J*ournal of Food Engineering*, 86, 422-432.
19. **Uzokwe E., Borokini T., Lawal I., Audu I., Adams A.,** (2012), Estimating the Leaf Area of Irvingia Gabonensis (Aubry-Lecomte ExO' Rorke) Baill from Linear Measurement, *Journal of Plant Studies*, 1(2), 2012.
20. **Watkins Ch. B., Nock J. F.** (2012), *Production Guide for Storage of Organic Fruits and Vegetables*, Department of Horticulture, Cornell University.
21. **Wiśniewski S., Wiśniewski T. S.** (2000), *Heat Transfer* (in Polish), Wydawnictwo Naukowo-Techniczne.

The paper was supported by project No. PBS1/A8/7/2012.

PARAMETRIC INTEGRAL EQUATIONS SYSTEMS METHOD IN SOLVING UNSTEADY HEAT TRANSFER PROBLEMS FOR LASER HEATED MATERIALS

Dominik SAWICKI[*], Eugeniusz ZIENIUK[**]

[*]Faculty of Mechanical Engineering, Bialystok University of Technology, ul. Wiejska 45C, 15-351 Białystok, Poland
[**]Faculty of Mathematics and Computer Science, University of Bialystok, ul. Konstantego Ciołkowskiego 1M, 15-245 Białystok

sawicki.dominik1@gmail.com, ezieniuk@ii.uwb.edu.pl

received 11 April 2015, revised 26 October 2015, accepted 28 October 2015

Abstract: One of the most popular applications of high power lasers is heating of the surface layer of a material, in order to change its properties. Numerical methods allow an easy and fast way to simulate the heating process inside of the material. The most popular numerical methods FEM and BEM, used to simulate this kind of processes have one fundamental defect, which is the necessity of discretization of the boundary or the domain. An alternative to avoid the mentioned problem are parametric integral equations systems (PIES), which do not require classical discretization of the boundary and the domain while being numerically solved. PIES method was previously used with success to solve steady-state problems, as well as transient heat transfer problems. The purpose of this paper is to test the efficacy of the PIES method with time discretization in solving problem of laser heating of a material, with different pulse shape approximation functions.

Key words: PIES Method, Transient Heat Transfer, Laser Heating, FEM

1. INTRODUCTION

High power lasers found broad application in processing and treatment of materials. They are very popular because of their unique properties, like high degree of special coherence, temporal dependence and beam directivity (Jewtuszenko et al., 2009; Gladush and Smurov, 2011). One of the laser applications is heating up the material in order to change its properties. This process depends highly on the properties of the processed material and the laser itself, therefore modeling and simulation of this phenomenon plays a key role in proper selection of these properties. Analytical methods can be used to simulate these problems (Brugger, 1972; Warren and Spark, 1990; Al-Nimr et al., 2002; Yanez et al., 2002), but they are rather used to solve problems defined with elementary shape areas and elementary boundary conditions. In more complex cases numerical methods are used. The most popular methods are finite element method (FEM) (Lewis et al., 1996) and boundary element method (BEM) (Brebbia te al., 1984; Tanaka et al., 1994; Majchrzak, 2001). FEM requires discretization of the whole domain, while BEM requires only discretization of the boundary. However, when using classical BEM for solving temperature equation, domain integral appears. Numerical integration over the domain requires dividing it into subdomains called cells. Dividing domain into cells in BEM is basically the same as dividing it into elements in FEM, so it loses its main advantage. There are some approaches that allow avoiding domain integrals, like dual reciprocity boundary element method (DRBEM) (Partridge et al., 1992) and multiple reciprocity boundary element method (MRBEM) (Nowak and Brebbia, 1989). However, these modifications have some limitations and cannot be used in all situations. Beside the large number of methods that already exist, it is still very important to search for new ones that would eliminate the disadvantages of the existing methods. An alternative approach is served by a group of methods called meshless methods (Johanssona and Lesnicb, 2008; Xiaokun et al., 2011; Jirousek et al., 1996). These methods require only a number of nodes located inside the domain and on the boundary. Over the past years a method based on the parametric integral equations systems (PIES) has been developed. PIESs are analytical modifications of the classical boundary integral equation (BIE) that allows solving problems without the need of discretization of boundary and domain. It uses Bézier or B-spline curves and patches for modeling. For time dependent problems it also allows to avoid the time discretization, but further research is needed. First, a version of PIES using time discretization should be properly tested. Authors found it interesting to test the method for time dependent boundary conditions.

This paper presents PIES method with time stepping scheme for laser heating of homogeneous materials. Results obtained with PIES have been compared with exact solution and results obtained with FEM.

2. PIES METHOD FOR UNSTEADY HEAT TRANSFER PROBLEMS

The differential equation for unsteady Fourier heat conduction, without internal heat sources, is governed by Brebbia et al. (1984) and Majchrzak (2001):

$$c\frac{\partial T(\mathrm{x},t)}{\partial t} = K\left(\frac{\partial^2 T(\mathrm{x},t)}{\partial x_1^2} + \frac{\partial^2 T(\mathrm{x},t)}{\partial x_2^2}\right), \tag{1}$$

where: $K[W/mK]$is the thermal conductivity, $T(\mathbf{x}, t)$ is the time-dependent temperature field, $c[J/m^3K]$ is the volume-specific

heat capacity, t is time.

The equation (1) is complemented by the given boundary conditions

$$\begin{cases} x \in \Gamma_1 : T(x,t) = T_s, \\ x \in \Gamma_2 : q(x,t) = -K\frac{\partial T}{\partial n} = q_s, \end{cases} \tag{1a}$$

where: is the given temperature on the boundary segment Γ_1, q_s is the given heat flux on the boundary segment Γ_2 and n is the normal vector.

An initial condition is given by

$$\mathrm{x} \in \Omega : \mathrm{T}(\mathrm{x}, 0) = T_0(\mathrm{x}), \tag{1b}$$

where T_0 is the given temperature inside the domain Ω at time $t = 0$.

Classical boundary integral equation (BIE) for (1) is presented in the form of Majchrzak (2001):

$$\begin{aligned} \alpha(\mathrm{x})T(\xi, t^F) &= -\frac{1}{c}\int_{t^0}^{t^F}\int_\Gamma T^*(\xi, \mathrm{x}, t^F, t)q(x,t)\,d\Gamma\,dt \\ &+\frac{1}{c}\int_{t^0}^{t^F}\int_\Gamma Q^*(\xi, \mathrm{x}, t^F, t)T(x,t)\,d\Gamma dt \\ &+\iint_\Omega T^*(\xi, \mathrm{x}, t^F, t^0)T(\mathrm{x}, t^0)d\Omega(\mathrm{x}), \end{aligned} \tag{2}$$

where t^0, t^F is the analyzed time interval and

$$\alpha(\xi) = \begin{cases} 1 & \xi \in \Omega \\ 0.5 & \text{for } \xi \in \Gamma \text{, for a smooth boundary.} \\ 0 & \xi \in \Omega \end{cases}$$

Integrands T^* and Q^* from equation (2) can be found in an explicit form in Majchrzak (2001).

After applying analytical modification to the classical BIE, similar to the one applied for steady problems [16], parametric integral equation system (PIES) (3) for unsteady heat transfer problem has been obtained (Zieniuk et al., 2014).

$$\begin{aligned} &0.5T_l(s_1, t^F) = \\ &= \frac{1}{c}\int_{t^0}^{t^F}\sum_{j=1}^{n}\int_{\bar{s}_{j-1}}^{\bar{s}_j}\bar{T}_{lj}^*(s_1, s, t^F, t)q_j(s,t)J_j(s)dsdt \\ &-\frac{1}{c}\int_{t^0}^{t^F}\sum_{j=1}^{n}\int_{\bar{s}_{j-1}}^{\bar{s}_j}\bar{Q}_{lj}^*(s_1, s, t^F, t)T_j(s,t)J_j(s)dsdt \\ &+\iint_\Omega \bar{\bar{T}}_{lj}^*(s_1, y, t^F, t^0)T(y, t^0)d\Omega(y) \end{aligned} \tag{3}$$

where: $\bar{s}_{l-1} \le s_1 \le \bar{s}_l, \quad \bar{s}_{j-1} \le s \le \bar{s}_j, \quad l = 1,2,3,\ldots,n.$ $\bar{s}_{l-1}, \bar{s}_l\ \bar{s}_{j-1}, \bar{s}_j$ is the beginning and the end of segments, respectively S_l and S_j, and $J_j(s)$ is the Jacobian of the transformation.

Integrands $\bar{T}_{lj}{}^*$, $\bar{Q}_{lj}{}^*$ and Integral Identity $\bar{\bar{T}}$ used for obtaining results inside domain have been presented in an explicit form in Zieniuk et al. (2014).

2.1. Numerical solution of PIES

To solve PIES for transient heat transfer problem (3), a strategy known from BEM and tested previously in PIES (Zieniuk et al., 2014) was used. This strategy involves discretization of the time variable and use of the time stepping scheme, with time step size Δt in order to get results at desired time. Collocation method was used to obtain an algebraic equations system, according to the algorithm provided in Zieniuk et al. (2014). Number of collocation points should be equal to the number of unknown coefficients in the series, used to approximate unknown boundary functions. After solving the algebraic equations system, unknown coefficients from approximating series are obtained. Presented approaches have been used before, to solve potential problems (Zieniuk, 2013) and lately also problems of transient heat transfer (Zieniuk et al., 2014).

3. LASER BEAM CHARACTERISTICS

The main function of the laser in material processing is to generate heat in the processed piece of material. A laser beam can be characterized with set of parameters, like divergence, radius, temporal structure and spatial intensity profile. The efficiency with which a material absorbs an incoming laser beam and converts it to heat depends on the properties of the material, like absorption coefficient, but also on the characteristics of laser beam itself (Jewtuszenko et al., 2009). In the general form, the total laser intensity can be written as

$$\mathrm{q}(\mathrm{r}, \mathrm{t}) = Aq_0\varphi(r)q_t(t), \tag{4}$$

where A is the effective absorption coefficient of the heated material, $\varphi(r)$ describes the (arbitrary) intensity distribution (beam shape) in the cross-section, $q_t(t)$ is the temporal dependence (pulse shape) and q_0 is the characteristic intensity of the laser (Gladush and Smurov, 2011).

Assuming the spatial intensity profile of the beam to be evenly distributed, equation (4) can be presented as

$$\mathrm{q}(\mathrm{t}) = Aq_0q_t(t). \tag{5}$$

Laser pulse shape $q_t(t)$ is often approximated by simple functions, like (Jewtuszenko et al., 2009):

– Rectangular pulse shape:

$$q_t(t) = \begin{cases} 1 & for \quad 0 < t \le t_s, \\ 0 & for \quad t_s < t. \end{cases} \tag{6}$$

– Triangular pulse shape:

$$q_t(t) = \begin{cases} 2\frac{t}{t_r} & for \quad 0 < t \le t_r, \\ 2\frac{(t_s - t)}{(t_s - t_r)} & for \quad t_r < t \le t_s, \\ 0 & for \quad t_s < t. \end{cases} \tag{7}$$

where t_r is the pulse rise time and t_s is the complete pulse time.

For more accurate approximation, Gaussian function can be used (Jewtuszenko et al., 2009):

$$q_t(t) = I\exp[-\gamma(t^\delta - t_r^\delta)]\left(\frac{t}{t_r}\right)^\beta, t > 0. \tag{8}$$

where parameters β, γ and δ are related to the pulse rise time t_r, while value of parameter I can be obtained from the condition of total energy conservation for distributions (6-8).

Fig. 1 presents $q_t(t)$ function diagram with $t_r = 0.2671[s]$ and $t_s = 1[s]$, for three different laser pulse shape approximation functions (6-8).

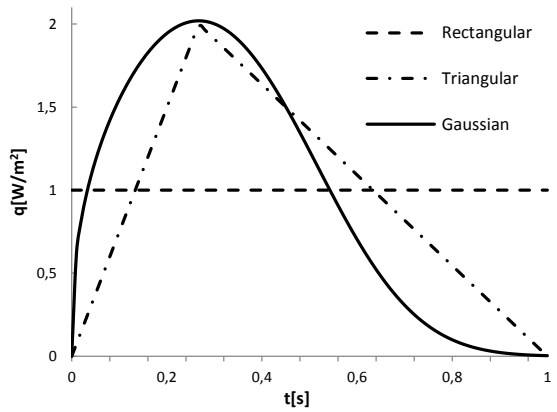

Fig. 1. Diagram of function $q_t(t)$ with $t_r = 0.2671[s]$ and $t_s = 1[s]$, for three different laser pulse shape approximation functions (7-9)

This paper presents heating of a Steel 45 material with Nd:YAG (neodymium-doped yttrium aluminum garnet) laser, for three different laser pulse shape approximation functions (6-8).

4. NUMERICAL ANALYSIS

Few examples have been solved to test efficiency of PIES method for issues simulating laser heating of a material, where all boundary conditions are dependent on time. Results obtained with PIES method have been compared to exact solution and results obtained with FEM. For FEM solution authors have used ANSYS Workbench 14 simulation tool called Transient Thermal. In FEM, square elements with quadratic shape function have been used to model the issue.

Accuracy and stability of results in PIES is dependent on many variables, like time step size Δt, number of collocation points used in the approximating series and their location, and number of weight coefficients in quadrature for integration over boundary and domain. There is a certain relationship between the time step size Δt and the number of weights in the quadrature over the domain in PIES (Zieniuk et al., 2014). The shorter the time step the larger number of weight coefficients has to be taken for integration over the domain. The applied FEM software uses the implicit time integration method, so it is unconditionally stable and does not apply Courant-Friedrich-Levy condition (Lewis et al., 1996). Taking into account the relationship in PIES and unconditionally stable FEM, both methods have been compared for the same time step sizes and a similar number of weight coefficients in quadrature for integration over the domain in PIES and nodes in FEM.

3.1. Rectangular pulse shape

First, a symulation of rectangular pulse shape approximation function (6) has been conducted. Exact solution of this problem is presented in the following form (Jewtuszenko et al., 2009):

$$\mathrm{T(y,t)} = Aq_0 \frac{2\sqrt{kt}}{K} ierfc\left(\frac{y}{2\sqrt{kt}}\right), y \geq 0, t \geq 0, \qquad (9)$$

where $k = K/c$ is the diffusion coefficient and $ierfc(x)$ is the integral of the complementary error function.

In the exact solution a laser heating of the half-space is considered. However, the half-space has to be approximated with a rectangular area for numerical calculations with PIES and FEM, as shown in Fig. 2.

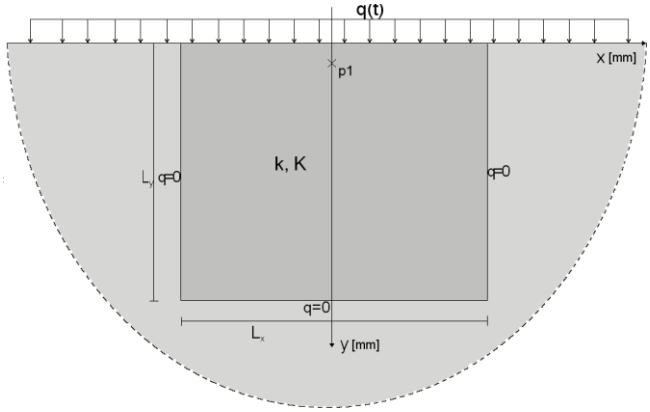

Fig. 2. Laser heating schema

Value of $q(t)$ has been calculated from equation (5). The energy losses by radiation and convection on the surface have been omitted. Material and laser parameters used in calculations are presented in Tab. 1.

Tab. 1. Parameters used for simulation of temperature distribution in material heated by laser beam (Jewtuszenko et al., 2009)

Metal	Laser	$\mathbf{t_s}$ $[ms]$	$\mathbf{t_r}$ $[ms]$	$\mathbf{q_0 \times 10^{-9}}$ $[Wm^{-2}]$	$\mathbf{K}$ $[Wm^{-1}K^{-1}]$	$\mathbf{k \times 10^5}$ $[m^2s^{-1}]$	$\boldsymbol{A}$ [%]
Steel 45	Nd:YAG	1	0.2671	0.58	33.5	1.5	41

The first step was to establish the optimal size of the area, L_x and L_y approximating the half space (Fig. 2). Height of the area L_y has been determined based on the exact solution (9). A minimal height y has been assumed, for which the temperature T and heat flux $q(t)$ are approximately equal to 0, for the given boundary condition (5) and maximum simulation time ($t = 2ms$). Width of the area L_x was established after a series of numerical experiments with use of PIES method. A minimal width L_x was sought, for which a further increase of this width won't have any impact on the results obtained at point $p1(0,0.04)$. It has turned out that the optimal size of approximating area is $L_x = L_y = 3$. It has been also established, that in order to get stable and accurate results there has to be a minimum of 9 collocation points evenly distributed on each of the boundary segments. Also a minimum number of 20 weight coefficients in quadrature for integration over each boundary segment has to considered.

In the next step, the example has been solved multiple times using both methods, PIES and FEM. Results have been obtained for different time step sizes, and different number weight coefficients in quadrature for integration over the domain in PIES and number of nodes in FEM. Results have been compared with the exact solution. Temperature has been measured at point $p1(0,0.04)$. Tab. 2 presents parameters of different PIES solutions. Results are shown in Fig. 3.

As it can be seen in Fig. 3, PIES method gives more accurate results when decreasing the time step size and increasing the number of weight coefficients in quadrature for integration over the domain. The best results (PIES-3) have been obtained for the smallest time step size and the largest number of weights.

DOI 10.1515/ama-2015-0028

Next, results obtained with FEM, have been compared with the exact solution. Input data for FEM are shown in Tab. 3. Results are presented in Fig. 4.

Tab. 2. Input data for PIES

	PIES-1	PIES-2	PIES-3
weights in the domain integral	10080	19680	40080
Δt **[ms]**	0.1	0.05	0.02

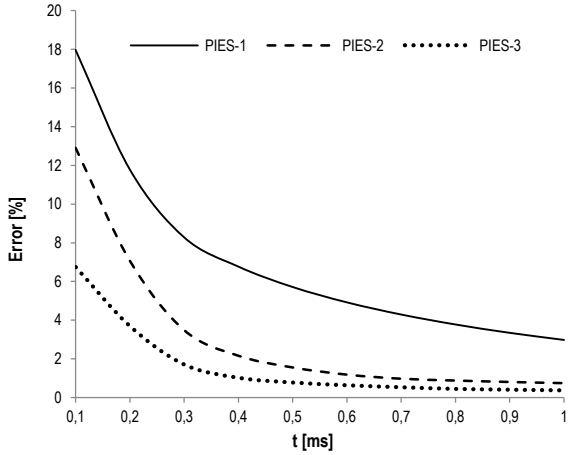

Fig. 3. Relative error [%] history at point $p1$, obtained by different PIES solutions, compared to the exact solution

Tab. 3. Input data for FEM

	FEM-1	FEM-2	FEM-3
elements	3249	6415	13293
nodes	9976	19564	40336
Δt **[ms]**	0.1	0.05	0.02

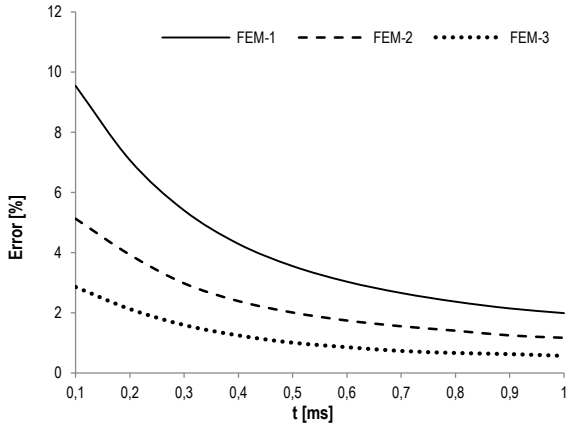

Fig. 4. Relative error [%] history at point $p1$ obtained by different FEM solutions, compared to the exact solution

FEM (Fig. 4) also gives more accurate results for smaller time step size and larger number of nodes (elements).

Tab. 4 presents temperature value at the point $p1$ and time t_s. Temperature has been obtained for the exact solution, best PIES solution and best FEM solution.

Tab. 4. Temperature at point $p1$ and time t_s

t[ms]	Exact	PIES-3	FEM-3
1	723.10	725.81	718.97

Taking into account the data presented in Fig. 3-4 it can be noticed that FEM gives more accurate results than PIES, which is especially visible in the beginning of simulation. Tab. 4 shows that for $t = t_s = 1[ms]$, best FEM and PIES solutions give results with similar accuracy.

In the next step, the best PIES solution and the best FEM solution have been compared. A longer time period has been considered, including the time after which the laser has been turned off. Fig. 5 presents temperature history at point $p1$, obtained with both methods during the laser heating process and after the laser has been turned off.

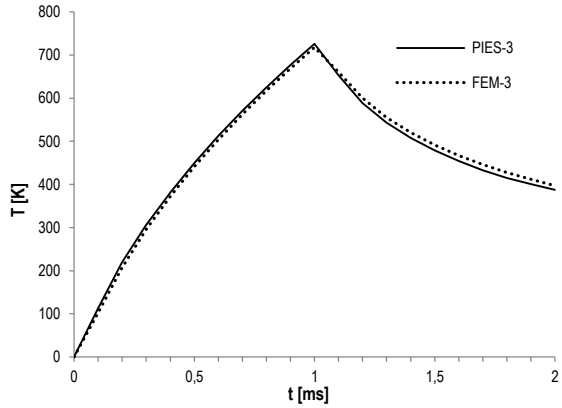

Fig. 5. Temperature history at point $p1$ obtained with best PIES and FEM solutions for rectangular beam shape

As can be noticed, both methods give close results during the whole simulation time.

3.2. Triangular pulse shape

Next, a simulation for the triangular pulse has been carried out (7). The exact solution for this particular problem does not exist, so the problem has been first solved with FEM and then with PIES. Results obtained with PIES have been compared to the best FEM results. In FEM a different number of elements, nodes and different time step size have been considered, as presented in Tab. 3. Results are presented on Fig. 6. Result is the temperature history at point $p1$.

As it can be seen on Fig. 6, improve of the accuracy of FEM solutions by reduction of the time step size and increase of the number of elements (nodes) leads to stabilization of results. FEM-3 has been chosen as the best solution.

Sequentially, the example has been solved with the use of PIES method and results have been compared to the best FEM solution (FEM-3). Parameters of specific PIES solutions can be found in Tab. 2. Temperature history at point $p1$ obtained with PIES can be found on Fig. 7.

Fig. 7 shows that increase of accuracy of PIES method brings the obtained results closer to results obtained with best FEM solution. Closest to the FEM-3 results were the best PIES results (PIES-3).

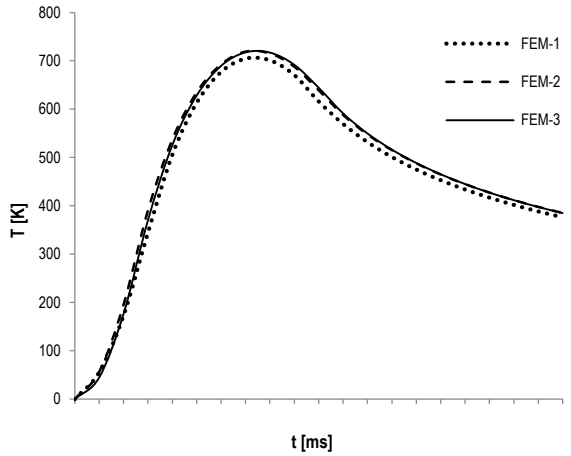

Fig. 6. Temperature history at point $p1$ obtained with FEM for triangular pulse shape

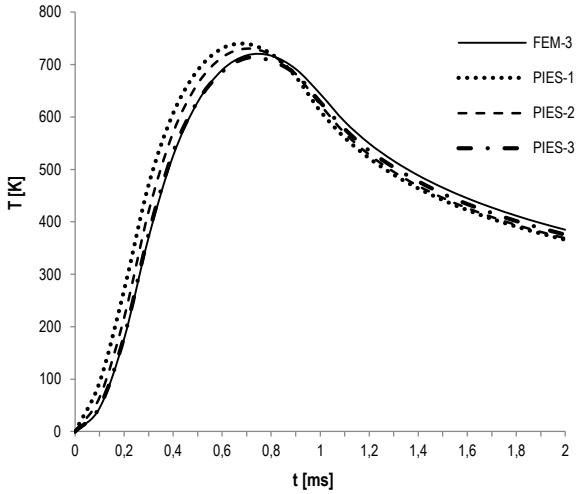

Fig. 7. Temperature history at point $p1$ obtained with PIES and compared to best FEM solution, for triangular pulse shape

3.3. Gaussian pulse shape

In the next step, the Gaussian approximation function (8) has been used in the simulation. The same procedure has been used here, as in previous example. Due to the lack of exact solution, examples has been solved first with FEM and best FEM solution was used as a reference points for results obtained with PIES method.

Different variants of FEM (Tab. 3) have been considered. Results are presented on Fig. 8. Result is the temperature history at point $p1$.

As it can be seen on Fig. 8, also in this case, increase of the accuracy of FEM solutions results in stabilization of obtained results.

Next, the example has been solved with PIES method. Obtained results are compared with FEM-3 results.

As can be noticed (Fig. 9), increase of accuracy in PIES makes the results obtained with this method closer to the best FEM results.

Fig. 10 presents the temperature history at point $p1$, obtained with best PIES-3 solution, for three different laser pulse shape approximation functions (6-8).

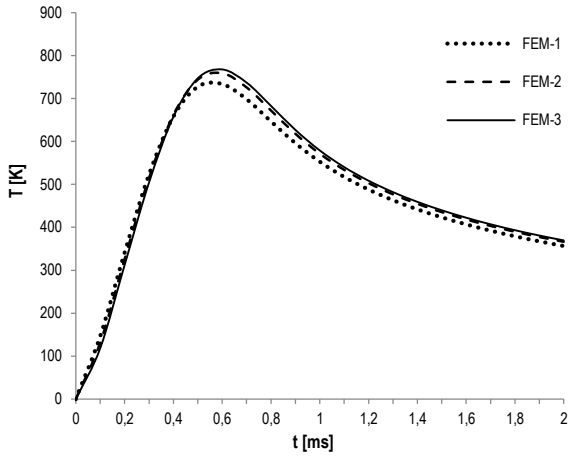

Fig. 8. Temperature history at point $p1$ obtained with FEM for Gaussian pulse shape

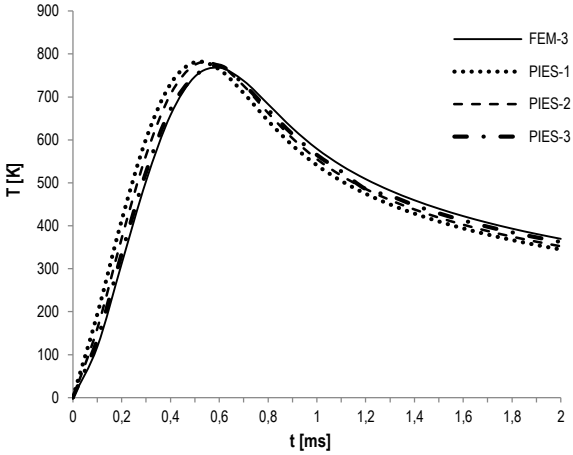

Fig. 9. Temperature history at point $p1$ obtained with PIES and compared to best FEM solution, for Gaussian pulse shape

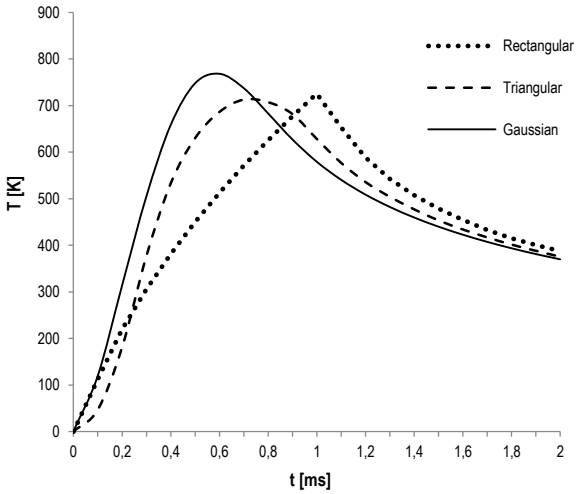

Fig. 10. Temperature history at point $p1$ obtained with best PIES solution, for three different pulse shapes

As can be seen on Fig. 10, the temperature history obtained for different pulse shape approximation functions varies, which is mostly visible at the beginning of simulation. After some time the temperature stabilizes and all graphs converge to a single point.

5. CONCLUSIONS

This paper presents the parametric intergral equations system for temperature equation, with the use of time stepping scheme. In the time stepping scheme each step is treated as a seperate problem, which allows in an easy way to solve issues with all boundary condition dependent on time. The exaples presented in this paper, laser heating of homogeneous materials belong to this category of issues. Three different functions approximating the real laser pulse shape have been considered. Comparison of the results with the exact solution and FEM found that PIES method gives accurate results, comparable with FEM. Therefore, PIES method can be an alternative for the commonly used FEM. In the future, further tests are planned to prove the effectiveness of PIES method in solving transient heat transfer problems.

REFERENCES

1. **Al-Nimr M. A., Alkam M., Arpaci V.** (2002), Heat transfer mechanisms during short-pulse laser heating of two-layer composite thin films, *Heat and Mass Transfer*, 38(7-8), 609-614.
2. **Brebbia C. A., Telles J. C., Wrobel, L. C.** (1984*), Boundary element techniques, theory and applications in engineering*, Springer, New York.
3. **Brugger K.** (1972), Exact solution for the temperature rise in a laser-heated slab, *J. Appl. Phys.*, 43, 557–583.
4. **Gladush G. G., Smurov I.** (2011), Physics of Laser Materials Processing: theory and experiment, *Springer series in materials science*, 146.
5. **Jewtuszenko A., Matysiak S. J., Różniakowska M.** (2009), The temperature and thermal stresses caused by the laser impact on construction materials (in Polish), OWPB, Białystok.
6. **Jirousek J., Qin Q. H.** (1996), Application of hybrid-Trefftz element approach to transient heat conduction analysis, *Computers & Structures*, 58, 195–201.
7. **Johanssona B. T., Lesnicb D.** (2008), A method of fundamental solutions for transient heat conduction, *Engineering Analysis with Boundary Elements*, 32, 697–703.
8. **Lewis R. W., Morgan K., Thomas H. R., Seetharamu K.** (1996), *The Finite Element Method in Heat Transfer Analysis*, Wiley.
9. **Majchrzak E.** (2001), Boundary element method in heat transfer (in Polish), Wydawnictwo Politechniki Częstochowskiej, Częstochowa.
10. **Nowak A. J., Brebbia C. A.** (1989), The multiple-reciprocity method. A new approach for transforming BEM domain integrals to the boundary, *Engineering Analysis with Boundary Elements*, 6, 164-167.
11. **Partridge P. W., Brebbia C. A., Wrobel L. C.** (1992), *The dual reciprocity boundary element method*, Computational Mechanics Publications, Southampton.
12. **Tanaka M., Matsumoto T., Yang Q. F.** (1994), Time-stepping boundary element method applied to 2-D transient heat conduction problems, *Applied Mathematical Modelling*, 18, 569–576.
13. **Warren R. E., Spark M.** (1979), Laser heating of a slab having temperature-dependent surface absorption, *J. Appl. Phys.*, 50, 7952-7958.
14. **Xiaokun Z., Rui D., Hua W.** (2011), A VBCM-RBF based meshless method for large deflection of thin plates, *International Conference on Multimedia Technology (ICMT)*, Hangzhou, 2380-2384.
15. **Yanez A., Alvarez J. C., Lopez A. J., Nicolas G., Perez J. A., Ramil A., Saavedra E.** (2002), Modelling of temperature evolution on metals during laser hardening process, *J. Appl. Surf. Sci.*, 186, 611-616.
16. **Zieniuk E.** (2013), *Computational method PIES for solving boundary value problems* (in Polish), Polish Scientific Publishers PWN, Warsaw.
17. **Zieniuk E., Sawicki D., Bołtuć A.** (2014), Parametric integral equations systems in 2D transient heat conduction analysis, *International Journal of Heat and Mass Transfer*, 78, 571–587.

DELAMINATION RESISTANCE OF LAMINATE MADE WITH VBO MTM46/HTS PREPREG

Piotr CZARNOCKI*, Kamila CZAJKOWSKA**

*Institute of Aeronautics and Applied Mechanics, Warsaw University of Technology, Nowowiejska 24, 00-665 Warsaw, Poland
**Institute of Aviation, Aleja Krakowska 110/114, 02-256 Warsaw, Poland

pecz@meil.pw.edu.pl, kamila.czajkowska @ilot.edu.pl

received 4 May 2015, revised 28 October 2015, accepted 29 October 2015

Abstract: A laminate made with the Vacuum Bag Only (VBO) prepregs can be cured out of autoclave. Because of low curing pressure such a process can result in deterioration of laminate mechanical properties. They can be significantly lower than those displayed by the autoclave cured ones. The resistance against delamination can be among the most affected. Since this property is a week point of all the laminates it was of particular interest. Delamination resistance of unidirectional laminate made from VBO MTM46/HTS(12K) prepreg was in the scope of the presented research and the critical values of the Strain Energy Release Rates and the Paris-type equations corresponding to Mode I, Mode II and Mixed-Mode I/II static and cyclic loadings, respectively, were determined.

Key words: Delamination, VBO Prepregs

1. INTRODUCTION

Vacuum Bag Only (VBO) prepregs are relatively new semi-finished raw products for manufacturing laminate primary airframe parts. Such prepregs can be cured out of autoclave with the use of ovens only, Due to this the related investment and production costs can be lowered since autoclaves and autoclave curing can be eliminated form manufacturing process. However processing conditions of such prepregs are not well established yet, especially in the case of MTM46/HTS(12K) one. For this prepreg the manufacturer suggested curing process should be carried at 130°C and under 90kPa vacuum pressure. Such a relatively low curing pressure, comparing to 800 kPa for prepregs cured in autoclaves, results in more difficult control of void formation and can generate problems with obtaining porosity in the range accepted by an aircraft industry, i.e. below 1%. The essential difference in the porosity control can be explained with the temperature-pressure-time diagrams overlapped with void size diagrams shown in Fig.1.

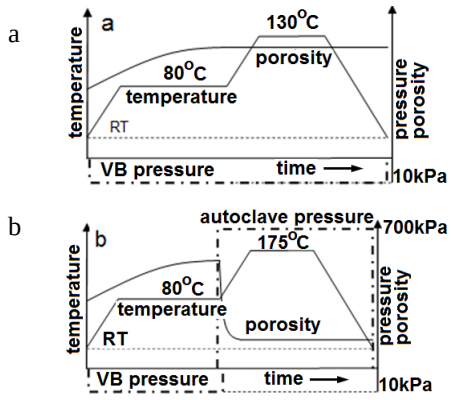

Fig. 1. Temperature-pressure-time diagrams overlapped with void size diagrams for: a) VBO prepregs, b) autoclave cured prepregs

An autoclave pressure of 8 bars, Fig.1a can suppress void formation and reduce size of already formed ones while vacuum pressure created in vacuum bag does not produce such an effect and reduction of porosity can only be achieved by evacuation of the air entrapped inside a laminate with the help of air evacuation ducts, Fig.2, that were produced in the course of specific impregnation process (Bai, 2013).

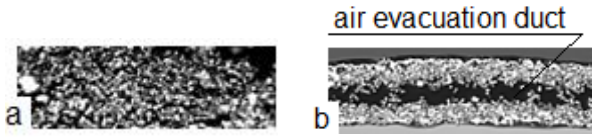

Fig. 2. Structure of uncured prepregs; a) autoclave cured a) VBO- air evacuation ducts are indicated

Resistance of laminates against delamination is their well-known weak point, in general, and porosity can make it even worst. In the case of laminates made with MTM46/HTS(12K) prepreg pores can be easily formed because of low curing pressure. The MTM46/HTS(12K) prepreg has often been considered as a potential candidate for manufacturing structural components of composite airframes. However, material data available in the literature and these provided by the manufacturer do not offer sufficient amount of information concerning the mentioned property. Therefore investigations of delamination resistance under static and cyclic loadings of a laminate made with MTM46/HTS(12K) prepreg were undertaken and the obtained results are presented in this paper. The critical values of the Strain Energy Release Rate (SERR) G_{Ic}, G_{IIc} and $G_{I/IIc}$, and the Paris-type equations were determined for Mode I, Mode II and Mixed-Mode I/II static and cyclic loadings for a unidirectional laminate. For this purpose the beam type laminate specimens were used. While Mode I, Mode II, Mixed-Mode I/II (ASTM D5528-12, ASTN D6671-13) static tests and fatigue Mode I (ASTM D6615-97) test have been standard-

DOI 10.1515/ama-2015-0029

ised, there is no standard procedure for Mode II and Mixed-Mode I/II fatigue tests, yet. Therefore, when necessary more detailed information on the test procedures and data reduction methods were provided.

2. EXPERIMENTAL

2.1. Specimens

The specimens were cut out from 300mm x 200mm x 3.2mm laminate plates consisted of 22 prepreg plies. To assure an appropriate ply compaction a debulking procedure was carried out for each four consecutive ply placements. The applied curing temperature-time and pressure-time profiles are shown in Fig. 3.

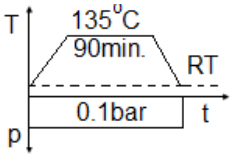

Fig. 3. Temperature-pressure-time curing profile

To facilitate delamination onset and propagation 0.013mm Teflon tape delamination starters were embedded in the middle plane of specimens. The specimen geometry and loading configurations are shown in Fig. 4. Both the static and cyclic Mixed-Mode tests were run for constant ratio of the SERR components G_{II}/G_I = 0.724.

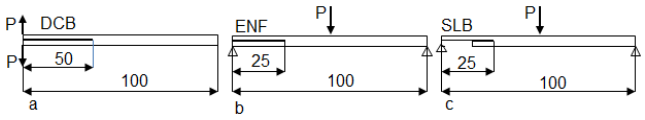

Fig. 4. Specimen geometry and loading configurations for: a) Mode I, b) Mode II and c) Mixed-Mode I/II tests

2.2. Testing

All the tests were run with the help of INSTRON Electro Puls E3000 testing machine equipped with 1000N load cell.

Static tests were run under displacement control with cross head speed 0.5mm/s and 0.75mm/s for Mode I, Mode II and Mixed-Mode I/II tests, respectively.

Fatigue tests were run with the use of the same equipment and under displacement control with the cyclic frequency 5Hz, the cycle parameter R=0.1 and initial values of $G_{I,\,II,\,I/II\,max}$ =0.5$G_{I,\,II,\,I/II\,c}$.

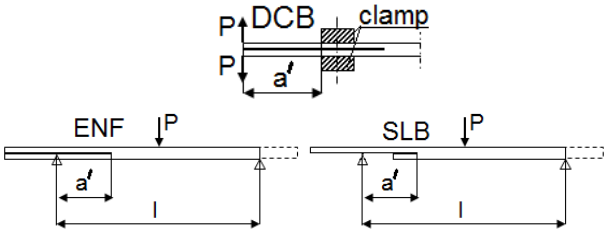

Fig. 5. Specimens configurations for experimental determination of C(a') relationships for DCB, ENF and SLB specimens

In the case of both the static and fatigue tests a current delamination length, a, was calculated based on specimen compliance changes C(a'). These relationships were determined experimentally for each specimen separately and then used for this particular specimen to calculate delamination length based on the compliance value.

Determination of C(a') relationship. To determine C(a') relationship specimens with oversize delamination starters were manufactured, Fig.5 and delamination growth, a', was simulated. End Notch Flexure (ENF) and Single Leg Bending (SLB) specimens were gradually shifted in jigs to the right, Fig.5, to change a' values. For each specimen and for each a' value a specimen compliance was calculated and C(a') relationship was constructed. In the case of Double Cantilever Beam (DCB) specimens changes in a' values could be obtained with the help of clamps which would be tighten in appropriate positions to obtain desired a' values. The range of a' changes was adjusted in such a way that the obtained C(a') relationships covered ranges of expected delamination growths in the real tests, i.e. 25≤a'≤50 for ENF and SLB specimens, and 50≤a'≤80 for DCB ones.

2.3. Data reduction

Static tests:

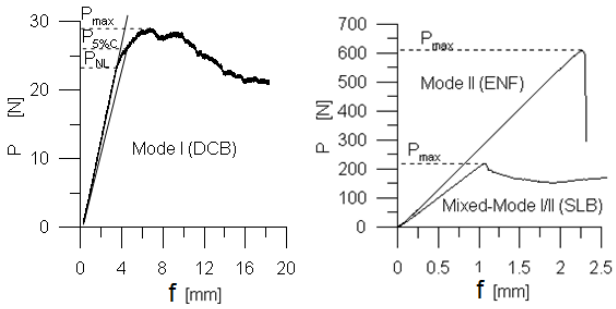

Fig. 6. Typical plots of P(f) relationships obtained from Mode I, Mode II and Mixed-Mode I/II static tests

Mode I test. ASTM D5528 recommends three data reduction methods: Modified Beam Theory (MBT), Compliance Calibration, (CC) and Modified Compliance Calibration (MCC). The critical values of the SERR according to these methods were calculated with the help of (1-3), respectively.

$$G_{Ic} = \frac{3Pf}{2B(a+\Delta)}, \tag{1}$$

$$G_{Ic} = \frac{nPf}{2Ba}, \tag{2}$$

$$G_{Ic} = \frac{3P^2C^{2/3}}{2A_1Bh}, \tag{3}$$

where: B – specimen width, P – load, f – relative displacement of loading points, h – half of specimen thickness, Δ – value determined experimentally by generating a least square plot of the cube root of compliance $\sqrt[3]{C}$, as a function of delamination length, C – compliance of the cracked beam (ratio of the loading point displacement over the applied load), n – slope of the straight line drawn through the data generated from a least square plot of log (f_i/P_i) versus log (a_i), A_1 – slope of the straight line drawn through the data generated from least squares plot of delamina-

tion length normalized by specimen thickness, a/h, as a function of the cube root of compliance, $\sqrt[3]{C}$.

In addition, three different values of force, P, and corresponding values of f could be considered, i.e. P_{NL}, corresponding to the onset of nonlinearity of $P(f)$ plot, $P_{5\%C}$, corresponding to the intersection of $P(f)$ plot with the straight line representing 1.05 of initial compliance and P_{max}, being maximum force value recorded during the test under consideration, see Fig. 6.

Mode II test. The tests were run according to ASTM D D6671 standard recommendations. The critical values of the SERR could be calculated with formula (4) or (5). For the presented research formula (4) was used

$$G_{IIc} = \frac{9a_0^2 P_{max} f_{max}}{2B(2L^3+3a_0{}^3)}, \tag{4}$$

or alternatively

$$G_{IIc} = \frac{3mP_{max}^2 a^2}{2B}, \tag{5}$$

where m is the slope of experimentally determined C(a) relationship of the form $C(a) = A + ma^3$

Mixed-Mode test. For this test SLB loading configuration was used. Although this configuration is not recommended by the ASTM D6671 standard, nevertheless it was chosen because an application of the same loading configuration for the cyclic tests was intended due to convenient jig design. For this loading configuration the critical value of the SERR is given by (6) (Szekrenyes, 2010).

$$G_{I/IIc} = \frac{21a^2 Pf}{2B(7a^3+2L^3)}. \tag{6}$$

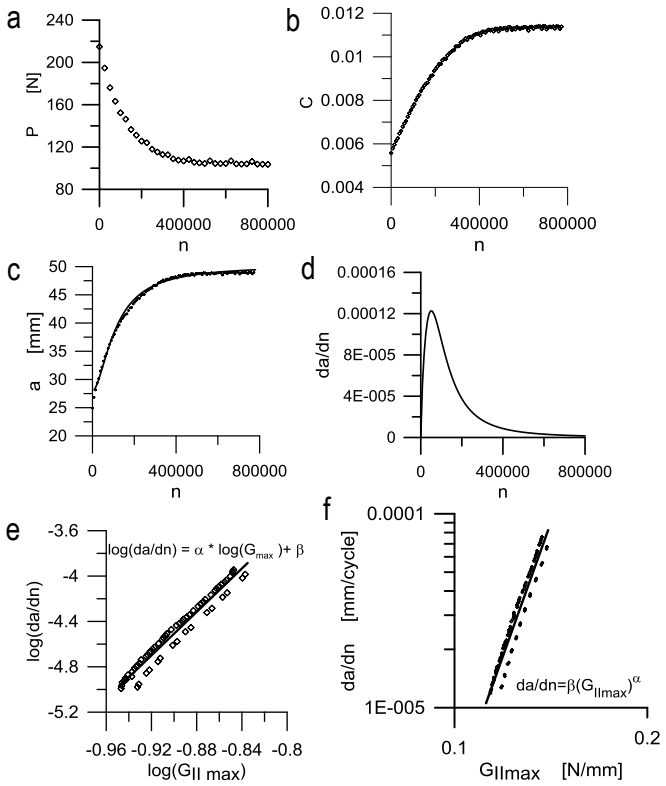

Fig. 7. Data reduction procedure: (a) raw data, (b) compliance vs. cycle elapsed, (c) a(n) obtained with the help of (7), (d) $da/dn(n)$ obtained based on (7) and (c), (e) auxiliary graph for determining coefficients of the Paris relationship, (f) sought Paris relationship

Fatigue tests. They aimed determination of Paris like relationships of the form $da/dn = f(G_{max})$. The tests have not been standardized yet except Mode I fatigue test for which recommendations are given in ASTM D6115 standard. Where possible, this standard was considered for Mode II and Mixed-Mode I/II data reduction procedures. The major departures from the standard recommendation was done regarding determination of $da/dn = f(n)$ relationships. The details of the applied procedure can be found in Czajkowska et al., (2014). The standard procedure recommends the 7-point polynomial piecewise approximation of $da/dn = f(n)$ relationship. For the purpose of the presented research this relationship was not obtained by the pricewise approximation but the entire set of a_i and corresponding n_i values was considered and correlated with the help of sigmoidal function of the form (7):

$$a = \frac{\alpha\beta+\gamma n^{\delta}}{\beta+n^{\delta}}, \tag{7}$$

where: $\alpha, \beta, \gamma, \delta$ are parameters needed to fit the curve

Delamination length, a, for each recorded n-th cycle was calculated with the help of previously determined C(a') relationship and corresponding pairs of P_i and f_i values. Since all the test were carried out under displacement control all the nominal deflection values, f, remained constant during each test.

2.4. Results

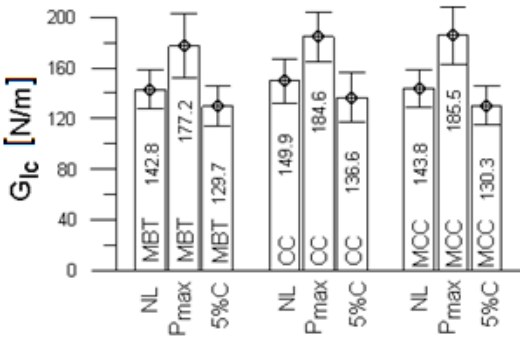

Fig.8. Values of GIc calculated according to MBT, CC and MCC data reduction procedures assuming P_c equal to P_{NL}, P_{max} and $P_{5\%C}$ for each of the method used.(For explanation of symbols and subscripts see eqs.1-3 and Fig. 6, respectively).
For each G_{Ic} value 95% confidence interval has been marked

Bar diagram in Fig. 8 presents initiation values of G_{Ic} calculated according to the three data reduction methods defined by eqs.1-3. For each data reduction method three different values of force, P_c, initiating delamination propagation were assumed. They were, (see Fig. 6):

- force corresponding to the onset of nonlinearity of $P(f)$ relationship, P_{NL};
- force corresponding to the intersection point of $P(f)$ plot and the straight line representing 5% increase in the compliance $C = f/P$, $P_{5\%C}$;
- force corresponding to the maximum of $P(f)$ plot, P_{max}.

Analysing the results used to construct bar diagram in Fig. 8 one could noticed that the most narrow 95% confidence interval as well as standard deviation were obtained for $P_c = P_{5\%C}$.

Plot in Fig.9 presents variation of the critical values of the SERR, G_{ci}, corresponding to the initiation of delamination propa-

DOI 10.1515/ama-2015-0029

gation as a function of the mode mixity defined with the phase angle Ψ (8), (Ψ=40.4° corresponds to G_{II}/G_I =0.724). G_{Ici} was calculated for $P_c = P_{5\%C}$ while G_{IIci} and $G_{I/IIci}$ for $P_c = P_{\max}$.

$$\Psi = atan\sqrt{\frac{G_{II}}{G_I}}. \quad (8)$$

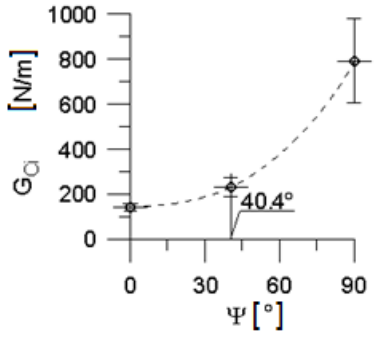

Fig. 9. Resistance against delamination under Mode I, Mode II and Mixed-Mode I/II static loadings. The plot represents the initiation values of G_{ci} versus phase angle Ψ (8) with 95%% CI marked

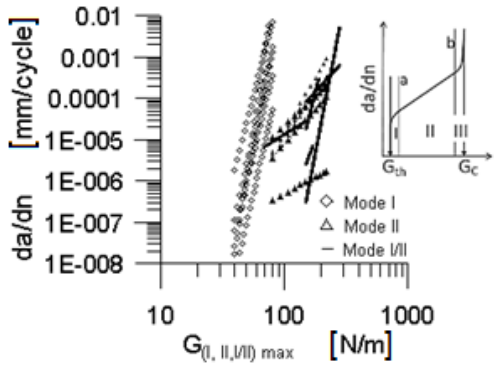

Fig.10. Paris relationships $da/dn = \beta(G_{max})^{\alpha}$ (region II, on the pictogram) for Mode I, Mode II and Mixed-Mode I/II loadings for MTM46/HTS(12K) laminate. Scatter of the results for each loading mode reflects the scatter of the laminate delamination resistance for the loading mode under consideration

Experimental results of fatigue tests are shown in Figs.10 and 11. for region II and I (see pictograms in Figs 10 and 11) of $da/dn(G_{max})$ relationship respectively. From plots in Fig.10 one could conclude that the most dangerous was Mode I loading. This founding corresponds with the results of the static tests showing the lowest resistance against delamination under static Mode I loading. Also, one could notice that for Mode I loading the rate of delamination propagation was more sensitive to the changes in G than for the two other loading Modes. The lowest sensitivity to such changes was noticed for Mode II. Unexpected relation between the delamination propagation rates was noticed for Mode II and Mixed-Mode I/II. In the aspect of GIIc and GI/IIc values, (Fig. 9), one would expect that the rate of delamination propagation under Mode II cyclic loading should be lower than that under Mixed-Mode loading, which was not the case.

Typical $da/dn(G_{max})$ relationships for low values of G_{max} (region I) are shown in Fig.11. It could be noticed that for Mode II and Mixed-Mode I/II loadings possibly threshold values of G_{max}, (for which delamination did not grow), could be indicated. This was not the case for Mode I loading for which a delamination growth rate da/dn < 10-7 cycle/mm was observed even for G_{max}<50N/m. (It was decided to terminate the tests at this delamination growth rate).

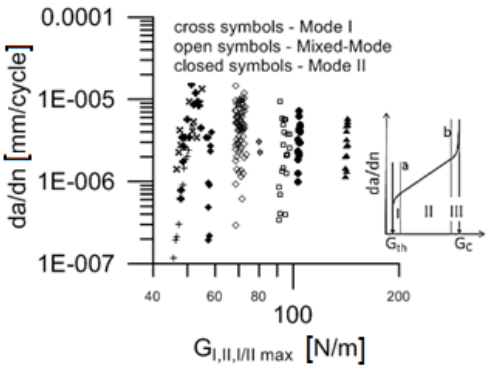

Fig. 11. Examples of $da/dn(G_{max})$ data for Mode I, Mode II and Mixed-Mode I/II fatigue loadings for low G_{max} values, (region I on the pictogram). Possible threshold values of G_{IImax} and $G_{I/IImax}$ could be noticed

2.5. Delamination resistance of MTM46/HTS laminates in perspective

For comparison purpose the critical values of the SERR for Mode I, Mode II and Mixed-Mode I/II loadings for common autoclave-cured laminates of aircraft grade are given in Tab. 1 together with the corresponding properties of MTM46/HTS.

Tab. 1. Interlaminar toughness of laminates

laminate	GIc N/m	GIIc N/m	GI/IIc N/m
MTM46/HTS	142	793	230
3501-6/AS4	200 [5]	525 [5]	-
8552/IM7	230 [6]	1334 [13]	280 [10]
977-3/IM7	154 [12]	670 [9]	-
914C/T300	112 [11]	220 [11]	220[11] G_{II}/G_I=1

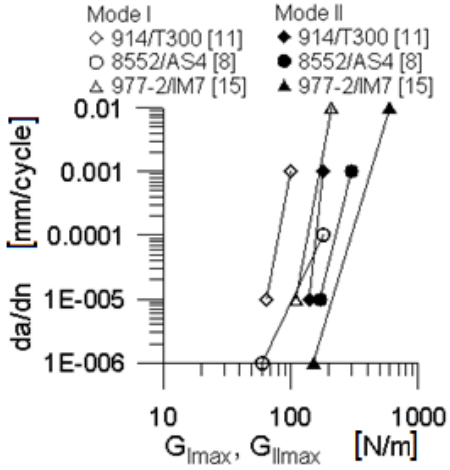

Fig. 12. Resistance against delamination of 914/T300, 8552/AS4 and 977-2/IM7 laminates under cyclic Mode I and Mode II loadings. Data reproduced from (Meziere and Michel, 2000; Hiley, 2000; Stelzer at al., 2013)

Comparison of fatigue data is difficult because there is scant reference to this data in generally accessible literature. Furthermore, the published data are in the form of plots only, and coefficients of Paris equations corresponding to these plots are not provided at all or are not complete. For this reason the plots shown in Fig. 12 are not very accurate representation of the cited literature data and should be regarded as same approximations of the original plots, only.

3. CONCLUSIONS

Comparing delamination resistance of MTM46/HTS laminate subjected to static and cyclic loadings against delamination resistance of aircraft grade laminates made with autoclave cured prepregs one could conclude that:

- VBO MTM46/HTS laminate displayed higher delamination resistance under static and cyclic loadings than laminate made with 914C/T300 prepreg containing non- toughened resin.
- in the case of autoclave cured laminates containing toughened resins their delamination resistance was significantly higher than that of the laminate tested.
- using out-of-autoclave curing process one could obtain laminates displaying similar delamination resistance as those for which autoclave curing process was used assuming that the laminates under consideration were impregnated with the resin systems of similar toughness.

REFERENCES

1. ASTM D5528-12 Standard Test Method for Mode I Interlaminar Fracture Toughness of Unidirectional Fiber-Reinforced Polymer Matrix Composites
2. ASTM D6115-97 Standard Test Method for Mode I Fatigue Delamination Growth Onset of Unidirectional Fiber-Reinforced Polymer Matrix Composites
3. ASTM D6671-13 Standard Test Method for Mixed Mode I-Mode II Interlaminar Fracture Toughness of Unidirectional Fiber Reinforced Polymer Matrix Composites
4. **Bai J. (ed.)** (2013)**,** *Advanced fibre–reinforced polymer (FRP) compositesfor structural application*, Woodhead Pu. Ltd.
5. **Becht G. J., Gillespie J. W.** (1989), Numerical and Experimantal Evaluation of the Mode III Interlaminar Fracture Toughness of Composite Materials, *Polymer Composites*, 10, 293-303.
6. **Czabaj M. W., Ratcliffe J.** (2012), *Comparison of Intralaminar and Interlaminar Mode-I Fracture Toughness of Unidirectional IM7/8552 Graphite/Epoxy Composite*, NACA raport NF 16762-15094.
7. **Czajkowska K., Czarnocki P, Lorenc Z**. (2014), Interlaminar Mode II Toughness of Unidirectional CF-Epoxy Laminates Made of out of Autoclave Prepregs, *Key Engineering Materials*, 598, 45-50.
8. **Hiley M**. (2000), Delamination between multi-directional ply interfaces in carbon-epoxy composite under static and fatigue loadings, *Fracture of Polymers, Composites and Adhesives, ESIS Publication 27*, 41-72.
9. **Kim R. Y**. (2001), *Polymer matrix composite (PMC) damage tolerance and repair technology*, Report No. UDR-TR-2001-00041.
10. **Lander J. K., Kawashita L. F, Allegri G, Hallett S. R, Wisnom M. R.**, (2010), A cut ply specimen for the determination of mixedmode interlaminar fracture toughness, *14th European Conference on Composite Materials*, 1-11.
11. **Meziere Y., Michel L.** (2000), Mixed-Mode delamination Failure criteria in Carbon Fibre/Composite under Quasi-Static and Cyclic Loadings, *Fracture of Polymers, Composites and Adhesives, ESIS Publication 27*, 97-110.
12. **Murri B**., (2011), Effect of Data Reduction and Fiber-Bridging on Mode I Delamination Characterization of Unidirectional Composites, *Proceedings of the American Society for Composites 26th Annual Technical Conference/2nd Joint US-Canada Conference on Composites.*
13. **Paris I., Minguet P. J., O'Brien T. K.** (2003), Comparison of Delamination Characterisation for IM7/8552 Composite Woven and Tape Laminates, *ASTM STP 1436*, 372-390.
14. **Stelzer S., Jones R., Brunner A. J**. (2013), Interlaminar Fatigue Crack Growth In Carbon Fiber Reinforced Composites, *The19th International Conference On Composite Materials*, 1-9.
15. **Szekrenyes A**. (2010), Crack Stability of Fractuer Specimens Used to Test Unidirectional Fiber Reinforced Material, *Experimental chanics*, 50, 473-482.

The work has been accomplished under the research project TEBUK financed by the National Centre for Research and Development and the European Regional Development Fund.

DOI 10.1515/ama-2015-0030

ANTIPLANE DEFORMATION OF A BIMATERIAL CONTAINING AN INTERFACIAL CRACK WITH THE ACCOUNT OF FRICTION 2. REPEATING AND CYCLIC LOADING

Heorhiy SULYM[*], Lyubov PISKOZUB[**], Yosyf PISKOZUB[**], Iaroslav PASTERNAK[***]

[*]Faculty of Mechanical Engineering, Bialystok University of Technology, ul. Wiejska 45C,, 15-351 Bialystok, Poland
[**]Ukrainian Academy of Printing, Pidgolosko Str. 19, 79020 L'viv, Ukraine
[***]Lutsk National Technical University, Lvivska Str. 75, 43018 Lutsk, Ukraine

h.sulym@pb.edu.pl, piskozub@uad.lviv.ua, piskozub@pancha.lviv.ua, pasternak@ukrpost.ua

received 3 March 2015, revised 26 October 2015, accepted 28 October 2015

Abstract: The paper presents the exact solution of the antiplane problem for an inhomogeneous bimaterial with the interface crack exposed to the normal load and cyclic loading by a concentrated force in the longitudinal direction. Using discontinuity function method the problem is reduced to the solution of singular integral equations for the displacement and stress discontinuities at the domains with sliding friction. The paper provides the analysis of the effect of friction and loading parameters on the size of these zones. Hysteretic behaviour of the stress and displacement discontinuities in these domains is observed.

Keywords: Friction, Tribofatigue, Cyclic Loading, Interfacial Crack, Energy Dissipation, Stress Intensity Factor, Antiplane Deformation, Bimaterial, Discontinuity Function, Hysteresis

1. INTRODUCTION

The account of friction in studying of the contact phenomena is one of the most urgent problems of mechanical engineering and materials science in the analysis of the phenomena and processes occurring in moving elements of cars, during various technological operations (Goryacheva, 2001; Comninou, 1977; Panasiuk et al., 1976; Sulym and Piskozub, 2004; Johnson, 1985; Hills et al.,1993; Ulitko and Ostryk, 2006; Datsyshyn et al., 2006). Thus, friction can be accompanied with electric, thermal, vibrating and chemical processes, which damp the internal dynamic processes essentially influencing the intensity materials wear, and consequently the reliability and durability of the structural elements made of them (Sosnovskiy, 2005; Bogdanovich and Tkachuk, 2009; Evtushenko and Kutsei, 2010; Pasternak et al., 2010; Pyrievet al., 2012). Friction influence can be both negative and positive.

From the point of view of structural integrity mechanics, friction of crack faces at their relative displacement is useful in most cases, since it causes internal strain energy dissipation, and consequently reduces the stress concentration, which reduces or even eliminates alternating plastic deformations at alternating loading. It is also known that development of the residual stress field thus assists in the adaptation of a material to operational loadings. The compression of composite materials arising doe to friction forces improves shear stress redistribution even in the case of macroscopic fracture of a fiber-matrix interface.

Negative consequences of a friction are mainly the wear of contacting surfaces, and also thermal emission. At excessive intensity the latter can sometimes cause unpredictable change in mechanical, physical and chemical properties of a material, distribution of physical fields, and consequently influence the diffusive processes, in particular hydrogen diffusion, and development of the fracture phenomena warned by tribofatigue (Sosnovskiy, 2005; Evtushenko and Kutsei, 2010, Pyriev et al., 2012).

This paper continues previous authors' publication (Sulym et al., 2015) and develops the technique for studying the influence of friction in the antiplane problem for a solid with a closed crack under the applied quasi-static (inertia-free) repeatedly changing loading, including cyclic one. The most general case is considered, when at each step the loading can either increase (additional loading) or change sign (unloading) reaching sufficient magnitude, which causes development of slippage zones.

2. PROBLEM STATEMENT

Problem statement coincides with those resulted earlier in Sulym and Piskozub (2004) except the way of loading. Here it is supposed, that a medium is subject to repeatedly changing loading, which cause the quasi-static antiplane deformation of a solid and corresponding stress strain state (in-plane loading is assumed to be constant). As the special case the cyclically changing loading can be considered, which is performed within the pattern loading-unloading-loading-...

As well as in the previous work (Sulym et al., 2015), consider an infinite isotropic medium consisting of two half-spaces with elastic constants $E_k,\ \nu_k,\ G_k \quad (k = 1,2)$, which are pressed to each other along their interface L with normal stress $\sigma_{yyk} = -P \ \ (k = 1,2;\ \ x \in L)$. Here the system of co-ordinates $Oxyz$ is used, with its origin at a plane xOz of contact of half-spaces, where NOz-coaxial strip cracks are localized at $L' = \bigcup_{n=1}^{N} L'_n = \bigcup_{n=1}^{N} [a_n^-;\ a_n^+]$ (Fig. 1).

Thus, the problem is reduced to study of stress strain state (SSS) of a cross-section xOy perpendicular to a direction z of its longitudinal (out-of-plane) displacement. The half-spaces perpendicular to this axis form to half-planes $S_k \ \ (k = 1, 2)$, and their interface correspond to the abscissa $L{\sim}x$.

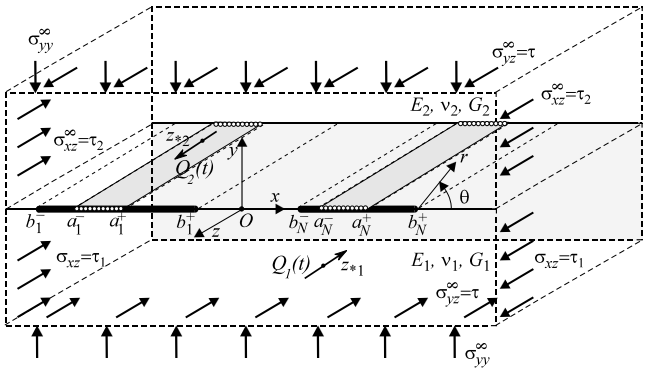

Fig. 1. The loading and geometric scheme of the problem

Thus, the problem is reduced to study of stress strain state (SSS) of a cross-section xOy perpendicular to a direction z of its longitudinal (out-of-plane) displacement. The half-spaces perpendicular to this axis form to half-planes S_k $(k = 1,2)$, and their interface correspond to the abscissa $L{\sim}x$.

The application of similar traditional notation for an axis z and a complex variable $z = x + iy$ should not cause misunderstanding in the solution of the problem.

Contact between the bimaterial medium components along a line $L'' = L\backslash L'$ is supposed to be mechanically perfect, and the contact along defects' (cracks') faces L' is assumed to be performed according to the laws of tangential mechanic contact, at which bodies contact mechanically perfect until the moment, when relative sliding of crack faces may start in some areas $\gamma_n^{(p)} \subset L'_n$ at the material interface (Johnson, 1985; Sulym et al., 2015).

Presence of such slippage zones (cracks with contacting faces) at each p-th step of loading (cycle) is modeled with stress and displacement discontinuity vectors at $\gamma_n^{(p)} \subset L'_n$ (Bozhydarnyk and Sulym, 1999; Sulym, 2007; Piskozub and Sulim, 2008):

$$[\Xi]_{L'} \equiv \Xi^- - \Xi^+ = \mathbf{f}_{(p)}(x,t), \tag{1}$$

for $x \in \gamma_n^{(p)} \subset L'_n$ $(n = \overline{1,N})$,

$$\mathbf{f}_{(p)}(x,t) = 0, \text{ if } x \notin \gamma_n^{(p)} \subset L'_n, \tag{2}$$

where $\Xi(z,t) = \{\sigma_{yz},\ \partial w/\partial x\}(z,t)$ is a state vector; $\mathbf{f}_{(p)}(x,t) = \{f_{3(p)}, f_{6(p)}\}(x,t)$ is a discontinuity vector; p in brackets denote the number of loading step (cycle); t is time as a formal monotonously increasing parameter related with the convertible loading. The following notation are used hereinafter: $[\phi] = \phi(x,-0) - \phi(x,+0)$, $\langle\phi\rangle = \phi(x,-0) + \phi(x,+0)$; indices "+" and "–" correspond to the limit values of a function at the top and bottom edges of a line L.

The friction contact conditions at the closed crack provide that at the achievement by tangent traction σ_{yz} at the lines $\gamma_n^{(p)}$ of a certain critical value $\tau_{yz}^{\max}$ the slippage occurs, and the tangent traction cannot exceed this threshold. Thus, within the classical Amontons' law of friction (Johnson, 1985), consider a variant of a contact problem according to which the tangent traction (friction traction) is constant along the lines $\gamma_n^{(p)}$:

$$\begin{aligned} &\sigma_{yz}^{\pm} = -sgn([w]_{(p)})\tau_{yz}^{max}, \\ &\tau_{yz}^{max} = -\alpha\sigma_{yy}(|w^- - w^+| \neq 0)' \end{aligned} \tag{3}$$

where α is a coefficient of dry friction. Outside the lines $\gamma_n^{(p)}$, which belong to L'_n, the tangent traction at the crack points without slippage does not exceed the possible admissible level

$$|\sigma_{yz}| \le \tau_{yz}^{\max}(w^- - w^+ = 0), \tag{4}$$

and the mutual crack face displacement (displacement discontinuity) is absent. The sign (an action direction) of tangent traction is chosen depending on a sign of the difference of displacements $[w]_{(p)}$ at a considered point of $\gamma_n^{(p)}$.

3. THE PROBLEM SOLUTION

Assume that the magnitude and direction of action of the external mechanical loading factors, which perform the longitudinal shear of a medium, change quasi-statically (so slowly that there is no necessity to consider inertial terms) under the certain law which can be arbitrary. Let the external loading of the problem be defined by monotonously changing in time intervals $[t_{(p-1)};\ t_{(p)}]$ step-by-step sequences of the following factors: stress $\sigma_{yz}^{\infty} = \sum_p \tau_{(p)}(t)$, $\sigma_{xz}^{\infty} = \sum_p \tau_{k(p)}(t)$ uniformly distributed at the infinity; the concentrated forces with magnitude $Q_k(t) = \sum_p Q_{k(p)}(t)$, and screw dislocations with Burgers vectors $b_k(t) = \sum_p b_{k(p)}(t)$ applied at the points $z_{*k} \in S_k (k = 1,2)$. It should be noticed that the positive direction of force and Burgers vectors is selected along z-axis (such that it along with x and y axes forms the right rectangular coordinate system), unlike Panasyuk et al. (1976), where the opposite directions is implicitly accepted as a positive one. According to (20.5) Sulym (2007), at each moment of time stress at the infinity should satisfy the condition:

$$\tau_{2(p)}(t)G_1 = \tau_{1(p)}(t)G_2, \tag{5}$$

which provides straightness of the material interface at the infinity.

The first (initial) step of loading and the SSS produced by it are considered in details in Ref [17], where the resulting system of singular integral equations (SSIE) is obtained

$$\begin{cases} f_{3(1)}(x,t) = 0, & (x \in L'), \\ g_{6(1)}(x,t) = \frac{1}{2C}\left(\langle\sigma_{yz(1)}^0(x,t)\rangle + 2\mathrm{sgn}[w]_{(1)}\tau_{yz}^{\max}\right), \end{cases} \tag{6}$$

which has the following closed-form solution:

$$\begin{aligned} &f_{6(1)}(x,t) = \frac{X_0^{*+}(x)}{\pi i}\int_{L'}\frac{F_{6(1)}(s,t)ds}{X_0^{*+}(s)(s-x)} + \\ &X_0^{*+}(x)Q_{n-1}(x), (x \in L'), \\ &X_0^*(z) = \prod_{n=1}^N\left[\left(z - a_{n(1)}^-\right)\left(z - a_{n(1)}^+\right)\right]^{-1/2}, \end{aligned} \tag{7}$$

where the factors at polynomials $Q_{n-1}(x)$ are determined from additional displacement continuity conditions at each crack:

$$\int_{a_{n(1)}^-}^{a_{n(1)}^+} f_{6(1)}(s,t)ds = 0 \quad \left(n = \overline{1,N}\right). \tag{8}$$

Here and further for each step the following notation is used (Sulym et al., 2015):

$$\begin{aligned} &\sigma_{yz(p)}^0(z,t) + i\sigma_{xz(p)}^0(z,t) = \tau_{(p)}(t) + i\{\tau_{k(p)}(t) \\ &+D_{k(p)}(z,t) + \left(p_k - p_j\right)\overline{D}_{k(p)}(z,t) + 2p_kD_{j(p)}(z,t)\}, \\ &D_{k(p)}(z,t) = -\frac{Q_{k(p)}(t) + iG_kb_{k(p)}(t)}{2\pi(z - z_{*k})}, (z \in S_k, \\ &k = 1,2), \\ &g_{r(p)}(z,t) = \frac{1}{\pi}\int_{L'}\frac{f_{r(p)}(x,t)dx}{x - z}, \\ &C = \frac{G_1G_2}{G_1 + G_2}, \qquad p_k = \frac{C}{C_j}. \end{aligned} \tag{9}$$

and SSS components are defined by relations

$$\begin{aligned}&\sigma_{yz(1)}(z,t)+i\sigma_{xz(1)}(z,t)=\sigma^0_{yz(1)}(z,t)\\&+i\sigma^0_{xz(1)}(z,t)+ip_kg_{3(1)}(z,t)-Cg_{6(1)}(z,t)\\&(z\in S_k;\ \ r=3,6;\ \ k=1,2;\ \ j=3-k);\\&\sigma^{\pm}_{yz(1)}(x,t)=\mp p_kf_{3(1)}(x,t)\\&-Cg_{6(1)}(x,t)+\sigma^{0\pm}_{yz(1)}(x,t),\\&\sigma^{\pm}_{xz(1)}(x,t)=\mp Cf_{6(1)}(x,t)+p_kg_{3(1)}(x,t)\\&+\sigma^{0\pm}_{xz(1)}(x,t),\qquad (x\in L').\end{aligned}\tag{10}$$

Consider the next step of loading. Assume that the components of SSS of the medium obtained at the end time $t_{(1)}$ of the previous (first) step can be considered as residual ones.

Then one can assume that the problem statement at this step differs from the formulation of the problem of the previous step in already existing displacement and stress discontinuities caused by the previous step of loading. Hence, at this step additional change in loading is accompanied with additional discontinuities and the representation of a total stress field, which account for the residual SSS from the previous ($p=1$) step, is as follows:

$$\begin{aligned}&\sigma_{yz}(z,t)+i\sigma_{xz}(z,t)=\sigma_{yz(1)}\big(z,t_{(1)}\big)\\&+i\sigma_{xz(1)}\big(z,t_{(1)}\big)+\sigma^0_{yz(2)}(z,t)+i\sigma^0_{xz(2)}(z,t)\\&+ip_kg_{3(2)}(z,t)-Cg_{6(2)}(z,t),\\&(z\in S_k;\ \ k=1,2;\ \ j=3-k).\end{aligned}\tag{11}$$

The total stress should satisfy the boundary conditions (3) at $\gamma_n^{(2)}$ with the account of a loading direction. Then one can formulate the following local problem for the second step:

$$\begin{aligned}&\sigma_{yz(2)}(z,t)+i\sigma_{xz(2)}(z,t)=\big\{\sigma_{yz}(z,t)+i\sigma_{xz}(z,t)\big\}\\&-\big\{\sigma_{yz(1)}\big(z,t_{(1)}\big)+i\sigma_{xz(1)}\big(z,t_{(1)}\big)\big\}\\&(z\in S_k;\ \ k=1,2;\ \ j=3-k)\end{aligned}\tag{12}$$

with boundary conditions

$$\begin{aligned}&\sigma^{\pm}_{yz(2)}(x,t)=-\mathrm{sgn}([w]_{(2)})\tau^{\max}_{yz}-\sigma^{\pm}_{yz(1)}\big(x,t_{(1)}\big),\\&x\in\gamma_n^{(2)}\subset L'_n\ (n=\overline{1,N}).\end{aligned}\tag{13}$$

Conditions (13) can be specified depending on a relation between $\gamma_n^{(2)}$ and $\gamma_n^{(1)}$:

$$\sigma^{\pm}_{yz(2)}(x,t)=\begin{cases}-\mathrm{sgn}([w]_{(2)})\tau^{\max}_{yz}+\mathrm{sgn}([w]_{(1)})\tau^{\max}_{yz}, & x\in\gamma_n^{(2)}\subset\gamma_n^{(1)}\\-\mathrm{sgn}([w]_{(2)})\tau^{\max}_{yz}-\sigma^{\pm}_{yz(1)}\big(x,t_{(1)}\big), & x\in\gamma_n^{(2)}\backslash\gamma_n^{(1)}.\end{cases}\tag{14}$$

According to Eq (14), the abovementioned assumption does not demand the proof in a case, when at a following step the sign of applied (local at this step) loading changes. As soon as at the moment $t_{(1)}$ of the first step end the local loadings reach their extreme values (at their increase those are maxima), a slippage zone is fixed in size, and contact surfaces stick together and the reached SSS is further considered as residual one. After that, with the beginning of a following step the magnitudes of total loadings start to decrease and quite similar to the process of unloading of the plastic material, new slippage does not arise, while at certain time $t^{st}_{(2)}\big(t_{(1)}<t^{st}_{(2)}\le t_{(2)}\big)$ the slippage conditions (3) are to be satisfied. Thus, the starting size of a slippage zone at the second step is always less than its size in the end of the previous step: $\gamma_n^{(2)}(t^{st}_{(2)})\subset\gamma_n^{(1)}(t_{(1)})$. Therefore, using for this case of loading the reasoning similar to that of the previous step one can obtain the following resulting SSIE

$$\begin{cases}f_{3(2)}(x,t)=0,\\g_{6(2)}(x,t)=\dfrac{1}{2C}\big\{\big\langle\sigma^0_{yz(2)}(x,t)\big\rangle+2\tau^{\max}_{yz}\big(\mathrm{sgn}[w]_{(2)}-\mathrm{sgn}[w]_{(1)}\big)\big\};\end{cases}$$

for determination of local (additional regarding the SSS reached at time $t_{(1)}$) stress and displacement discontinuities from local (for this step) loadings. The obtained solution differs from Eqs (7)–(10) only in the influence of additional term $-2\tau^{\max}_{yz}\mathrm{sgn}[w]_{(1)}$ at the right hand side of SSIE (15), and of course, the superscript in brackets defines the second step.

Providing similar reasoning for the following steps of alternating monotonously changing loading one can obtain the local problem for the p-th step:

$$\begin{aligned}&\sigma_{yz(p)}(z,t)+i\sigma_{xz(p)}(z,t)=\big\{\sigma_{yz}(z,t)+i\sigma_{xz}(z,t)\big\}\\&-\sum_{i=1}^{p-1}\big\{\sigma_{yz(i)}\big(z,t_{(i)}\big)+i\sigma_{xz(i)}\big(z,t_{(i)}\big)\big\}\\&\big(z\in S_k;\ \ k=1,2;\ \ j=3-k;\ t>t_{(p-1)}\big)\end{aligned}\tag{16}$$

with boundary conditions:

$$\begin{aligned}&\sigma^{\pm}_{yz(p)}(x,t)=-\mathrm{sgn}([w]_{(p)})\tau^{\max}_{yz}-\sigma^{\pm}_{yz(p-1)}\big(x,t_{(m)}\big)\\&=-\tau^{\max}_{yz}\big(\mathrm{sgn}[w]_{(p)}-\mathrm{sgn}[w]_{(p-1)}\big),\\&x\in\gamma_n^{(p)}\subset L'n\ (n=\overline{1,N}),\end{aligned}\tag{17}$$

which results in the following SSIE

$$\begin{cases}f_{3(p)}(x,t)=0,\\g_{6(p)}(x,t)=\dfrac{1}{2C}\big\{\big\langle\sigma^0_{yz(p)}(x,t)\big\rangle+2\tau^{\max}_{yz}\big(\mathrm{sgn}[w]_{(p)}-\mathrm{sgn}[w]_{(p-1)}\big)\big\};\end{cases}\tag{18}$$

and its solution has the same structure as in Eqs (7)–(10).

In general the local displacement discontinuity and energy dissipation at the p-th step are defined as:

$$\begin{aligned}&[w]_{(p)}(x,t)=\int_{a_{n(p)}}^{x}f_{6(p)}(s,t)ds,\\&x\in\gamma_n^{(p)}\subset L'\mathrm{n},(n=\overline{1,N}),\end{aligned}\tag{19}$$

$$W^d_{(p)}(t)=-\int_{L'}\tau^{\max}_{yz}\big|[w]_{(p)}(x,t)\big|\,dx.\tag{20}$$

As a consequence, total values of stress, strain, displacement and its discontinuity, the dissipated energy etc. after the p-th step can be presented as a superposition, for instance

$$\begin{aligned}&[w](x,t)=\textstyle\sum_{m=1}^{p-1}[w]_{(m)}(x,t_{(m)})+[w]_{(p)}(x,t)\\&\big(x\in L';\ \ t>t_{(p-1)}\big)\end{aligned},\tag{21}$$

$$W^d(t)=\textstyle\sum_{m=1}^{p-1}W^d_{(m)}\big(t_{(m)}\big)+W^d_{(p)}(t),\ \big(t>t_{(p-1)}\big).\tag{22}$$

As well as in Sulym et al. (2015), for detailed illustration of the developed approach for solution of the problem consider a special case of alternating loading symmetric concerning a vertical axis ($z_{*k}=\pm id$) of a medium containing a single ($N=1$) crack $L'_1=[-b;\ b]$. Then in the bounds of L'_1 at each loading step only a symmetric slippage zone $\gamma_1^{(p)}=\big[-a_{(p)};\ a_{(p)}\big]\big(a_{(p)}\le b\big)$ can occur and

$$\begin{aligned}&\big\langle\sigma^0_{yz(p)}(x,t)\big\rangle=2\tau_{(p)}(t)-4p_1\mathrm{Im}D_{2(p)}(x,t)-\\&4p_2\mathrm{Im}D_{1(p)}(x,t),\qquad Q_0(x)\equiv c_0=0.\end{aligned}$$

In this case the solution of the integral equation (18) after calculation of corresponding integrals is as follows:

$$f_{6(p)}(x,t)=\frac{1}{\pi C\sqrt{a_{(p)}^2-x^2}}\left\{\pi\left(\tau_{(p)}(t)+\tau_{yz}^{\max}\left(\operatorname{sgn}[w]_{(p)}-\operatorname{sgn}[w]_{(p-1)}\right)\right)x+\right.$$
$$\left.+\sum_{k=1}^{2}p_{2-k}\left(Q_{k(p)}(t)\operatorname{Im}\frac{\sqrt{{z_{*k}}^2-a_{(p)}^2}}{x-z_{*k}}+G_k b_{k(p)}(t)\operatorname{Re}\left(\frac{\sqrt{{z_{*k}}^2-a_{(p)}^2}}{x-z_{*k}}+1\right)\right)\right\},\qquad \left(x\in[-a_{(p)};\ a_{(p)}]\right). \tag{23}$$

The function $X(z)=\sqrt{z^2-a^2}$ is understand as a branch, satisfying the condition $\sqrt{z^2-a^2}/z\to 1$ as $z\to\infty$. Similar reasoning is used for a choice of branches of functions $\sqrt{z_{*k}^2-a^2}$and $\sqrt{\bar{z}_{*k}^2-a^2}$, $k=1,\ 2$.

Based on Eq (23) one can obtain the following formula for $g_{6(p)}(z,t)$:

$$g_{6(p)}(z,t)=\frac{1}{C}\left[\tau_{(p)}(t)+\tau_{yz}^{\max}\left(\operatorname{sgn}[w]_{(p)}-\left(\operatorname{sgn}[w]_{(p-1)}\right)\right]\left(1-\frac{z}{\sqrt{z^2-a_{(p)}^2}}\right)-\frac{p_1G_2b_{2(p)}(t)+p_2G_1b_{1(p)}(t)}{\pi C\sqrt{z^2-a_{(p)}^2}}\right.$$
$$\left.-\frac{1}{2\pi C}\sum_{k=1}^{2}p_{2-k}\left(iQ_{k(p)}(t)R_k^-\left(a_{(p)},z,z_{*k}\right)-\left(G_kb_{k(p)}(t)R_k^+\left(a_{(p)},z,z_{*k}\right)\right)\right),\quad \left(z\notin[-a_{(p)};\ a_{(p)}]\right), \tag{24}$$

where:

$$R_k^{\pm}(a,z,z_{*k})=\frac{1}{\pi}\int_{-a}^{a}\left(\frac{\sqrt{z_{*k}^2-a^2}}{x-z_{*k}}\pm\frac{\sqrt{\bar{z}_{*k}^2-a^2}}{x-\bar{z}_{*k}}\right)\frac{dx}{\sqrt{a^2-x^2}(x-z)}=\frac{1}{\sqrt{z^2-a^2}}\left(\frac{\sqrt{z_{*k}^2-a^2}}{z_{*k}-z}\pm\frac{\sqrt{\bar{z}_{*k}^2-a^2}}{\bar{z}_{*k}-z}\right)-\left(\frac{1}{z_{*k}-z}\pm\frac{1}{\bar{z}_{*k}-z}\right).$$

Expression for displacement discontinuity $[w]_{(p)}$ can be obtained from Eqs (19), (23) as

$$[w]_{(p)}(x,t)=\int_{-a_{(p)}}^{x}f_{6(p)}(s,t)ds=-\frac{1}{C}\left(\tau_{(p)}(t)+\tau_{yz}^{\max}\left(\operatorname{sgn}[w]_{(p)}-\operatorname{sgn}[w]_{(p-1)}\right)\right)\sqrt{a^2{}_{(p)}-x^2}+$$
$$+\frac{1}{\pi C}\left\{\sum_{k=1}^{2}p_{2-k}\left(Q_{k(p)}(t)\operatorname{Im}I(x,z_{*k})+G_kb_{k(p)}(t)\left(\pi+2\arcsin\frac{x}{a_{(p)}}+\operatorname{Re}I(x,a_{(p)},z_{*k})\right),\quad \left(|x|\le a_{(p)}\right),\right.\right. \tag{25}$$

where: $I(x,a,z)\equiv\sqrt{z^2-a^2}\int_{-a}^{x}\frac{dx}{\sqrt{a^2-t^2}(x-z)}=i\ln\frac{a(z-x)}{a^2-xz-i\sqrt{a^2-x^2}\sqrt{z^2-a^2}}$.

From Eqs (20), (25) it follows the expression for energy dissipation $W_{(p)}^{d}(t)$:

$$W_{(p)}^{d}(t)=-\int_{-a_{(p)}}^{a_{(p)}}\tau_{yz}^{\max}\left|[w]_{(p)}(x,t)\right|dx=-\frac{\tau_{yz}^{\max}}{C}\left|\frac{\pi a_{(p)}^2}{2}\left(\tau_{(p)}(t)+\tau_{yz}^{\max}\left(\operatorname{sgn}[w]_{(p)}-\right.\right.\right.$$
$$\left.\left.\left.-\operatorname{sgn}[w]_{(p-1)}\right)\right)+\sum_{k=1}^{2}p_{2-k}\left(Q_{k(p)}(t)\right)\operatorname{Im}\left(\sqrt{z_{*k}^2-a_{(p)}^2}-z_{*k}\right)+G_kb_{k(p)}(t)\operatorname{Re}\left(\sqrt{z_{*k}^2-a_{(p)}^2}-z_{*k}\right)\right|. \tag{26}$$

Consider in details the determination of the size $a_{(p)}$ of the slippage zone at each step of loading. Here SIF is the defining parameter, which is determined within Eq (22) of Sulym and Piskozub (2004) as:

$$K_{3(p)}(t)=\frac{1}{\sqrt{\pi a_{(p)}}}\int_{-a_{(p)}}^{a_{(p)}}\sqrt{\frac{a_{(p)}\pm x}{a_{(p)}\mp x}}\sigma_{yz}(x,t)\,dx=\frac{1}{\sqrt{\pi a_{(p)}}}\int_{-a_{(p)}}^{a_{(p)}}\sqrt{\frac{a_{(p)}\pm x}{a_{(p)}\mp x}}\left\{\sum_{m=1}^{p-1}\sigma_{yz(m)}\left(x,t_{(m)}\right)+\sigma_{yz(p)}^{0}(x,t)+\operatorname{sgn}[w]_{(p)}\tau_{yz}^{\max}\right\}dx$$
$$=\sqrt{\pi a_{(p)}}\left(\sum_{m=1}^{p-1}\tau_{(m)}(t_{(m)})+\tau_{(p)}(t)+\operatorname{sgn}[w]_{(p)}\tau_{yz}^{\max}\right)-\frac{1}{\sqrt{\pi a_{(p)}}}\sum_{k=1}^{2}p_{2-k}\left\{\left(\sum_{m=1}^{p-1}Q_{k(m)}(t_{(m)})+Q_{k(p)}(t)\right)\operatorname{Im}\frac{a_{(p)}\pm z_{*k}}{\sqrt{z_{*k}^2-a_{(p)}^2}}+\right.$$
$$\left.+\left(\sum_{m=1}^{p-1}b_{k(m)}(t_{(m)})+b_{k(p)}(t)\right)G_k\operatorname{Re}\left(\frac{a_{(p)}\pm z_{*k}}{\sqrt{z_{*k}^2-a_{(p)}^2}}\mp 1\right)\right\}. \tag{27}$$

The equality of SIF to zero provides the condition for slippage start at the p-th step, the magnitude of the first critical loading $Q_{k(p)}^{*}$, and the size $a_{(p)}$ of the slippage.

For definiteness it is assumed (other cases are studied similarly) that at the point $z_{*2}=id$ of the top half-space only one alternating monotonously changing concentrated force with magnitude $Q_2(t)=\sum_m Q_{2(m)}(t)$ is applied, which increase at odd and decrease at even m. SIF magnitude, the size of a slippage zone, displacement discontinuity and energy dissipation at the first step of such loading are studied in Ref [17]. Consider the second step (unloading), when $Q_{2(2)}(t)<0\ \left(t>t_{(1)}\right)$. Accounting for the fact that $\operatorname{sgn}[w]_{(2)}=1$ at this step, from expression (27) one can obtain the size of new slippage zone

$$a_{(2)}(t)=\sqrt{\frac{p_1^2Q_{2(2)}(t)^2}{4\pi^2{\tau_{yz}^{\max}}^2}-d^2}, \tag{28}$$

and a condition at unloading, when the slippage starts over again

$$\left|Q_{2(2)}(t)\right|\ge\frac{2\pi d\tau_{yz}^{\max}}{p_1}=Q_{2(2)}^{*}=2Q_{2(1)}^{*}. \tag{29}$$

Here the first critical value of the applied force at the p-th step is denoted as $Q_{2(p)}^{*}$. Local displacement discontinuity and the energy dissipation at the second step for such loading (while the condition (29) holds) is as follows

$$[w]_{(2)}(x,t)=\int_{-a_{(2)}}^{x} f_{6(2)}(x,t)dx=\frac{p_1Q_{2(2)}(t)}{2\pi C}\ln\frac{\sqrt{a_{(2)}^2+d^2}-\sqrt{a_{(2)}^2-x^2}}{\sqrt{a_{(2)}^2+d^2}+\sqrt{a_{(2)}^2-x^2}}-\frac{2}{C}\tau_{yz}^{\max}\sqrt{a_{(2)}^2-x^2}\left(|x|\le a_{(2)}\right); \tag{30}$$

$$W_{(2)}^{d}(t)=-\int_{-a_{(2)}}^{a_{(2)}}\tau_{yz}^{\max}\left|[w]_{(2)}(x,t)\right|dx=\frac{\pi a_{(2)}^2{\tau_{yz}^{\max}}^2}{2C}-\frac{\tau_{yz}^{\max}}{C}p_1Q_{2(2)}(t)\left(\sqrt{a_{(2)}^2+d^2}-d\right). \tag{31}$$

Assuming that $a=b$ in (29) one can obtain the second critical force, at which nonzero SIF (singular stress) arise at the vicinity of crack tips

$$Q_{2(2)}^{**}=\frac{2\pi\tau_{yz}^{\max}}{p_1}\sqrt{d^2+b^2}=2Q_{2(2)}^{*}\frac{\sqrt{d^2+b^2}}{d}.$$

Continuing similar reasoning for the following steps of loadings one can find that both critical loadings of the second and following steps is higher twice than corresponding critical loadings of the initial step.

For smooth contact between crack faces (zero friction coefficient) one should assume $\tau_{yz}^{\max}=0$ in the abovementioned equations. This special case coincides with the solution of the antiplane problem for an interfacial crack under the identical static loading in Panasyuk et al. (1976) and in Sulym (2007).

Let's prove that the proposed additive approach of the account of repeating loading is suitable and for the case when at the following step the applied loading does not change its sign. As at time $t_{(1)}$ the first step loading reaches maximum, and then continues to increase already at the second step, the slippage zon after the first step continues to grow without a delay to a maximum $\gamma_n^{(2)}(t)\supset\gamma_n^{(1)}(t_{(1)})$ $\left(t_{(2)}^{st}=t_{(1)}\right)$ of the second. Hence, if the total solution after the second step obtained by means of Eqs (23)–(28) coincides with the solution of this problem in a single step, but the medium is then subjected to the total loading of two steps. Thus, the proposed technique can be used for the arbitrary quasi-static multistage loading. Let's show this on the abovementioned example for the two first steps of action of symmetric loading with the regard to the vertical axis ($z_{*k}=\pm id$) of a medium with a single ($N=1$) crack. For simplification of calculations we will assume that only one concentrated force $Q_{2(p)}(t)$ acts in the medium. Since $a_{(2)}(t)\ge a_{(1)}(t_{(1)})$ for $t\ge t_{(1)}$, in this case one should account for the second part of the boundary conditions (14), which contains the following terms:

$$\sigma_{yz(1)}^{\pm}\left(x,t_{(1)}\right)=\sigma_{yz(1)}^{0\pm}\left(x,t_{(1)}\right)-Cg_{6(1)}\left(x,t_{(1)}\right)=\sigma_{yz(1)}^{0\pm}\left(x,t_{(1)}\right)-\frac{C}{\pi}\int_{-a_{(1)}}^{a_{(1)}}\frac{f_{6(1)}(\xi,t_{(1)})d\xi}{\xi-x},$$
$$x\subset\left[-a_{(2)};a_{(2)}\right]\backslash\left[-a_{(1)};a_{(1)}\right]. \tag{32}$$

Calculating $K_{3(2)}(t)$ at the second step one obtains

$$K_{3(2)}(t)=\frac{1}{\sqrt{\pi a_{(2)}}}\int_{-a_{(2)}}^{a_{(2)}}\sqrt{\frac{a_{(2)}\pm x}{a_{(2)}\mp x}}\left\{\sigma_{yz(1)}\left(x,t_{(1)}\right)+\sigma_{yz(2)}^{0}(x,t)+\operatorname{sgn}[w]_{(2)}\tau_{yz}^{\max}\right\}dx=$$
$$=\frac{1}{\sqrt{\pi a_{(2)}}}\int_{-a_{(2)}}^{a_{(2)}}\sqrt{\frac{a_{(2)}\pm x}{a_{(2)}\mp x}}\left(\sigma_{yz(2)}^{0}(x,t)+\operatorname{sgn}[w]_{(2)}\tau_{yz}^{\max}+\begin{cases}-\operatorname{sgn}[w]_{(1)}\tau_{yz}^{\max}, & x\in\gamma_1^{(2)}\subset\gamma_1^{(1)}\\ \sigma_{yz(1)}^{0}(x,t)-Cg_{6(1)}\left(x,t_{(1)}\right), & x\in\gamma_1^{(2)}\backslash\gamma_1^{(1)}\end{cases}\right)dx=$$
$$=\frac{1}{\sqrt{\pi a_{(2)}}}\int_{-a_{(2)}}^{a_{(2)}}\sqrt{\frac{a_{(2)}\pm x}{a_{(2)}\mp x}}\left(\sigma_{yz(2)}^{0}(x,t)+\operatorname{sgn}[w]_{(2)}\tau_{yz}^{\max}\right)dx-\frac{\operatorname{sgn}[w]_{(1)}\tau_{yz}^{\max}}{\sqrt{\pi a_{(2)}}}\int_{-a_{(1)}}^{a_{(1)}}\sqrt{\frac{a_{(2)}\pm x}{a_{(2)}\mp x}}dx+$$
$$+\frac{1}{\sqrt{\pi a_{(2)}}}\int_{-a_{(2)}}^{-a_{(1)}}\sqrt{\frac{a_{(2)}\pm x}{a_{(2)}\mp x}}\left(\sigma_{yz(1)}^{0}(x,t)-Cg_{6(1)}\left(x,t_{(1)}\right)\right)dx+$$
$$+\frac{1}{\sqrt{\pi a_{(2)}}}\int_{a_{(1)}}^{a_{(2)}}\sqrt{\frac{a_{(2)}\pm x}{a_{(2)}\mp x}}\left(\sigma_{yz(1)}^{0}(x,t)-Cg_{6(1)}\left(x,t_{(1)}\right)\right)dx. \tag{33}$$

Accounting for $\operatorname{sgn}[w]_{(2)}=\operatorname{sgn}[w]_{(1)}=-1$ in the considered case, and utilizing the values of integrals

$$\frac{1}{\pi}\int_{-a}^{a}\frac{\xi d\xi}{\sqrt{a^2-\xi^2}(\xi-x)}=1-\frac{|x|}{\sqrt{x^2-a^2}},$$
$$\frac{1}{\pi}\int_{-a}^{a}\frac{d\xi}{\sqrt{a^2-\xi^2}(\xi-x)(\xi-z)}=\frac{1}{z-x}\left(-\frac{1}{\sqrt{z^2-a^2}}+\frac{\operatorname{sgn}(x)}{\sqrt{x^2-a^2}}\right)x\notin[-a;a],$$
$$\int_{-b}^{-a}\sqrt{\frac{b\pm\xi}{b\mp\xi}}d\xi+\int_{a}^{b}\sqrt{\frac{b\pm\xi}{b\mp\xi}}d\xi=2b\left(\frac{\pi}{2}-\arcsin\frac{a}{b}\right),\qquad\int_{-b}^{-a}\sqrt{\frac{b\pm\xi}{b\mp\xi}}\frac{|\xi|d\xi}{\sqrt{\xi^2-a^2}}+\int_{a}^{b}\sqrt{\frac{b\pm\xi}{b\mp\xi}}\frac{|\xi|d\xi}{\sqrt{\xi^2-a^2}}=b\pi,$$
$$\int_{-b}^{-a}\sqrt{\frac{b\pm\xi}{b\mp\xi}}\frac{\operatorname{sgn}(\xi)d\xi}{(\xi-id)\sqrt{\xi^2-a^2}}+\int_{a}^{b}\sqrt{\frac{b\pm\xi}{b\mp\xi}}\frac{\operatorname{sgn}(\xi)d\xi}{(\xi-id)\sqrt{\xi^2-a^2}}=\frac{\pi(b\pm id)}{\sqrt{a^2+d^2}\sqrt{b^2+d^2}}, \tag{34}$$

one obtains SIF as:

$$K_{3(2)}(t)=\sqrt{\pi a_{(2)}}\left(\tau_{(1)}(t_{(1)})+\tau_{(2)}(t)-\tau_{yz}^{\max}\right)-\sqrt{\frac{a_{(2)}}{\pi}}\frac{p_1\left(Q_{2(1)}(t_{(1)})+Q_{2(2)}(t)\right)}{\sqrt{a_{(2)}^2+d^2}}, \tag{35}$$

which coincides with the sum of expressions (25) and (26) of Sulym et al. (2015) for the case of a single-step loading equal to $\tau_{(1)}(t_{(1)}) + \tau_{(2)}(t)$ and $Q_{2(1)}(t_{(1)}) + Q_{2(2)}(t)$.

Thus, the proposed additive approach to the sequence of residual SSS is suitable for the account of multistage loading-unloading. However, for simplification of the solution procedure it is expediently to unite the consecutive steps of additional loading or unloading in one single step. In this case, the solution of the problem formulated in section 1 can be easily obtained by means of the above-stated technique for alternating loading.

4. THE NUMERICAL ANALYSIS

Consider the following dimensionless values, which significantly reduce the amount of calculations without loss in generality: $a_{(p)}/b$, x/b, d/b are the slippage zone, co-ordinate x and distance to the concentrated force application point, respectively, normalized to the semi-length of a crack at the p-th step; $\beta_{(p)} = Q_{(p)}(t)/Q^*_{(1)}$ is a normalized magnitude of the applied force at the p-th step; $\pi dC[w]_{(p)}(x,t)/bp_1Q^*_{(1)}$, $CW_{(p)}(x,t)/\pi\alpha^2b^2P^2$ are normalized displacement discontinuity and the energy dissipation at the p-th step.

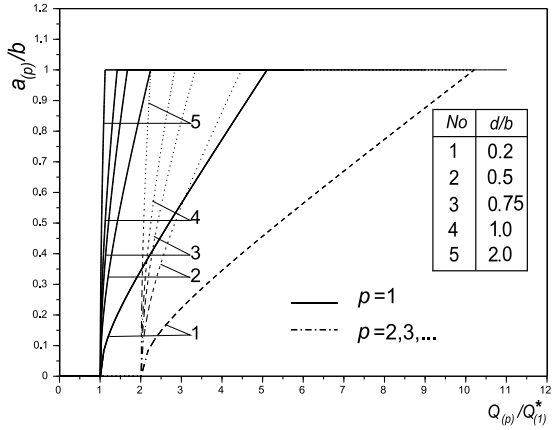

Fig. 2. Dependence of the size of a slippage zone on the loading parameters at the p-th step

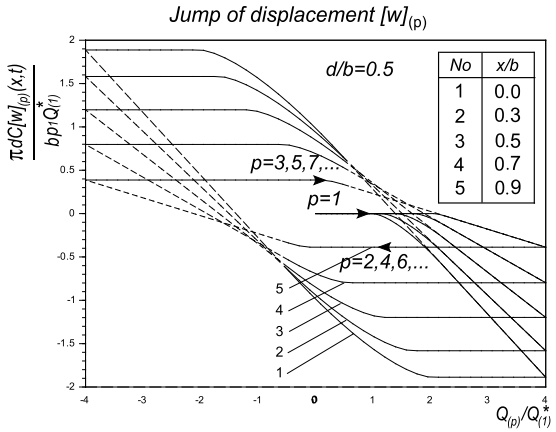

Fig. 3. Hysteretic behavior of displacement discontinuity in a full cycle of loading

Fig. 2 plots the dependence of the size $a_{(p)}/b$ of a slippage zone at the p-th step on the dimensionless magnitude $\beta_{(p)} = Q_{(p)}(t)/Q^*_{(1)}$ of the applied force.

It should be notices that for $\beta_{(p)} \leq 1$ the slippage is always absent, and for $1 \leq \beta_{(p)} \leq 2$ it occurs only at the first (initial) step of a cycle. The slippage zone at a step grows monotonously with increase in the magnitude of loading, not exceeding the size of a crack.

Fig. 3 illustrates the hysteretic behaviour of the total displacement discontinuity $\pi dC[w]_{(p)}(x,t)/bp_1Q^*_{(1)}$ at various points x/b of the slippage zone depending on the magnitude of loading in the alternating cycle $4Q^*_{(1)} \to -4Q^*_{(1)} \to 4Q^*_{(1)} \to -4Q^*_{(1)} \to \ldots$. Here it is well observed that such character of change is inherent to displacement discontinuities not only at the centre of slippage zone, but also to all of its points. Continuous lines correspond to a range of change of loading between the first and the second critical values, when the slippage zone has not reached crack tips yet. The dot line denote displacement discontinuities for loading exceeding the second critical force, when at the vicinity of crack tips stress singularity arise.

Change in the form of both local and total displacement discontinuities $\pi dC[w]_{(p)}(x,t)/bp_1Q^*_{(1)}$ in the zero-base cycle $10Q^*_{(1)} \to 0 \to 10Q^*_{(1)} \to 0 \to \ldots$ in its dependence on x/b is plotted in Fig. 4. It is well-noted that after a full cycle of change of loading crack edges do not come back into their initial positions, thus keeping some residual displacement discontinuity, which increase together with a friction coefficient. For $Q_{(p)}(t)/Q^*_{(1)} \leq 2$ the slippage at the second and subsequent steps does not occur.

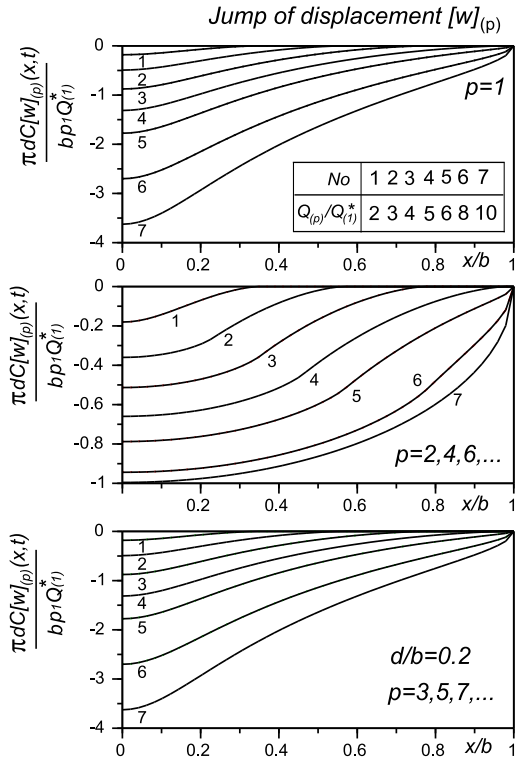

Fig. 4. Dependence of the form of displacement discontinuity on the magnitude of loading at the p-th step

Fig. 5 illustrates the dependence of the form of displacement discontinuity on the relative remoteness d/b of the force application point in the zero-base cycle $4Q^*_{(1)} \to 0 \to 4Q^*_{(1)} \to 0 \to \ldots$. The increase in d/b decreases the range of $Q^{**}_{(p)}/Q^*_{(p)} = \sqrt{d^2 + b^2}/d$ and accordingly, the sensitivity of $[w]_{(p)}(x,t)$ to this parameter.

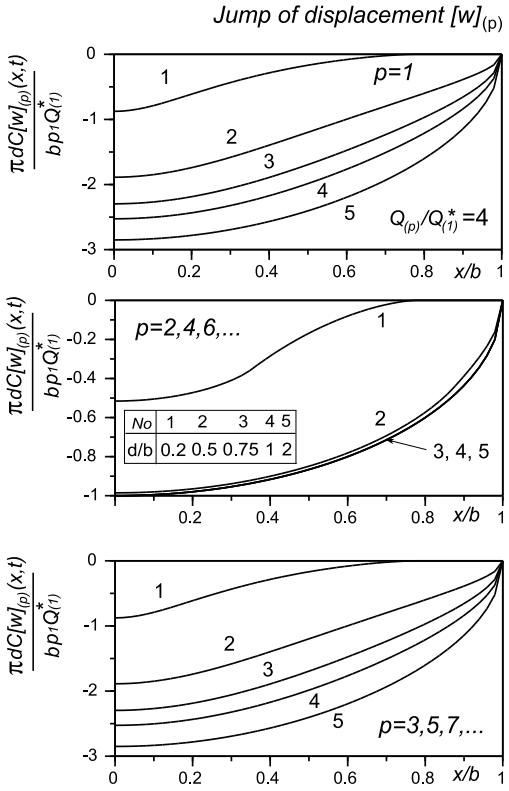

Fig. 5. Dependence of the form of displacement discontinuity on the relative remoteness of the force application point at the p-th step

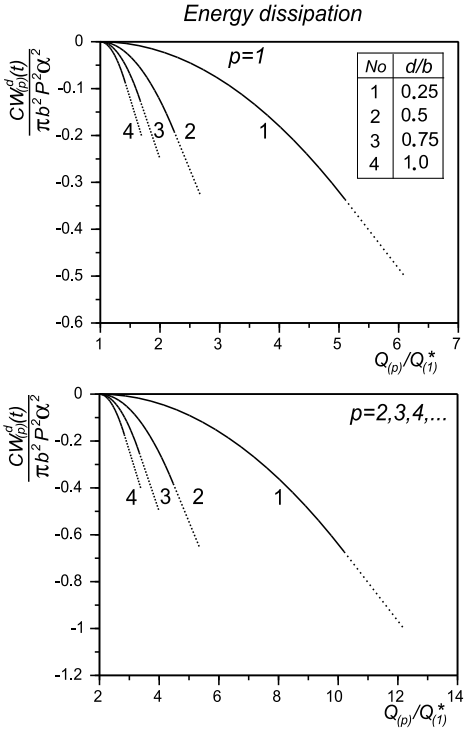

Fig. 6. Dependence of energy dissipation on relative remoteness of the force application point at the p-th step

Energy dispersion $CW^d_{(p)}(t)/\pi\alpha^2 b^2 P^2$ at the p-th step of the alternating cycle $4Q^*_{(1)} \to -4Q^*_{(1)} \to 4Q^*_{(1)} \to -4Q^*_{(1)} \to \ldots$ depending on the relative remoteness d/b of the force application point is plotted in Fig. 6. Continuous lines correspond to a range of change of loading between the first and the second critical values, when the slippage zone has not reached crack tips yet. The dot line denote displacement discontinuities for loading exceeding the second critical force, when at the vicinity of crack tips stress singularity arise. Total energy dissipation at time t can be obtained using Eq (22).

Thus one can conclude that the parameter G_1/G_2 characterizing the difference of mechanical properties of half-spaces' materials is negligible in the resulted calculations due to a choice of dimensionless quantities of the problem.

REFERENCES

1. **Bogdanovich P. N., Tkachuk D. V.** (2009), Thermal and thermomechanical effects in sliding contact (in russian), *Treniye i iznos*, 30, No 3, 214-229.
2. **Bozhydarnyk V. V, Sulym H.** (1999), *Elements of the theory of plasticity and strength* (in ukrainian), L'viv, Svit.
3. **Cherepanov G.P.** (1966), On the development of cracks in compressed bodies (in russian), *Prikladnaya matematika i mehanika*, 30, No 1, 82–93.
4. **Comninou M.** (1977), The interface crack, *J. Appl. Mech.,* 44, 631–636.
5. **Datsyshyn O. P., Kadyra V. M. (**2006), A fracture mechanics approach to prediction of pitting under fretting fatigue conditions, *Int. J. of Fatigue,* 28, No 4, 375–385
6. **Evtushenko A. A., Kutsei M.** (2010), Effect of pressure evolution during braking on temperature of a pad-disk tribosystem, *J.Friction and Wear,* 31(5), 317–325.
7. **Goryacheva I.G.** (2001), *Mechanics of frictional interaction* (in russian), Moskva, Nauka.
8. **Goryacheva I. G., Rajeev P. T., Farris T. N.** (2001), Wear in partial slip contact, *J. Tribology,* 123**,** 848–856.
9. **Hills D. A, Nowell D., Sackfield A.** (1993), *Mechanics of elastic contact,* Butterworth-Heinemann, Oxford.
10. **Johnson K. L.** (1985), *Contact mechanics*, Cambridge University press.
11. **Ostryk V. I., Ulitko A. F.** (2006), *Wiener-Hopf method to contact problems of theory of elasticity* (in russian), Kiev, Naukova dumka.
12. **Panasyuk V. V. et al.** (1976), *Distribution tense neighborhood of cracks in the plates and shells* (in russian), Kiev, Naukova dumka.
13. **Pasternak Ya. M., Sulym H. T., Piskozub L. G.** (2010), Models of thin inclusion with the account of imperfect contact with the medium (in russian), *Proc. of VI International symposium on Tribo-Fatigue MSTF 2010 in 2 parts, part 2.*, Minsk, BGU, 399–404.
14. **Piskozub J. Z., Sulim G. T.** (2008), Thermoelastic equilibrium of piecewise homogeneous solids with thin inclusions, *Journal of Engineering Mathematics*, *Special Issue Thermomechanics*, 61**,** 315–337.
15. **Pyriev S. Yu.** et al. (2012), Thermomechanical wear during quasi-stationary frictional heating (in russian), *Treniye i iznos,* 33, No 5, 435–443.
16. **Sosnovskiy L. A.** (2005), Tribo-Fatigue. *Wear-fatigue damage and its prediction (Foundations of engineering mechanics)*, Series: Foundations of Engineering Mechanics, Springer.
17. **Sulym H. T., Piskozub L. G., Piskozub Y. Z., Pasternak Ya. M.** (2015), Antiplane deformation of a bimaterial containing an interfacial crack with the account of friction. I. Single loading, *Acta Mechanica et Automatica*, vol.9, No 2, 115-121.
18. **Sulym H. T.** (2007), *Fundamentals of the mathematical theory of thermoelastic equilibrium of deformable bodies with thin inclusions* (in ukrainian), Lviv, Doslidno-vydavnychyy tsentr NTSh.
19. **Sulym H. T., Piskozub Y.Z.** (2004), Conditions of contact interaction (review) (in ukrainian), *Mat. metody i fiz.-meh. polya*, 47, No 3, 110–125.